Low-energy excitations in some complex oxides by resonant inelastic X-ray scattering: RMnO3 (R = Tb, Dy) and Lu2V2O7

Jiatai Feng

Université Pierre et Marie Curie

École doctorale :
Chimie physique et chimie analytique de Paris Centre

Laboratoire de Chimie Physique–Matière et Rayonnement (UMR 7614)

Low-energy excitations in some complex oxides by resonant inelastic X-ray scattering: $RMnO_3$ (R = Tb, Dy) and $Lu_2V_2O_7$

---

par Jiatai FENG

Thèse de doctorat

dirigée par Gheorghe Sorin CHIUZBĂIAN

présentée et soutenue publiquement le 28 Septembre 2017

devant le jury composé de :

M^{me}	Christel GERVAIS-STARY	Université Pierre et Marie Curie	Présidente
M^{me}	Christine RICHTER	Université de Cergy-Pontoise	Rapportrice
M.	Antonio TEJEDA GALA	Université Paris Sud	Rapporteur
M.	Andrei POSTNIKOV	Université de Lorraine	Examinateur
M.	Gheorghe Sorin CHIUZBĂIAN	Université Pierre et Marie Curie	Directeur de thèse
M^{me}	Amélie JUHIN	Université Pierre et Marie Curie	Invitée

Cette thèse est dédiée à Maman et Papa.
Sans eux, je n'aurais jamais vu le jour.
Aussi pour ma chérie, qui me soutient au fond.
C'est aussi un cadeau pour ma fille.

Cogito, ergo sum.
– René Descartes

Remerciements

Ce manuscrit de thèse contient l'aboutissement de trois années de travail. Je voudrais fortement remercier les personnes qui m'ont accompagnées durant cette période.

J'ai effectué cette recherche au Laboratoire Chimie Physique–Matière et Rayonnement [Université Pierre et Marie Curie et CNRS (UMR 7614)]. Je remercie son directeur, Alain Dubois, pour son accueil bienveillant, ses conseils et son écoute.

J'adresse mes sincères remerciements à Gheorghe Sorin Chiuzbăian, mon directeur de thèse, et aussi pour m'avoir donné le goût de la recherche à travers un sujet très riche et à l'interface de plusieurs disciplines, entre théorie et expérience. Je remercie vivement les membres de notre équipe : Renaud Delaunay, Romain Jarrier et Jean-Michel Mariot pour avoir participé aux temps de faisceau au synchrotron SOLEIL. Je remercie particulièrement Jean-Michel Mariot pour le temps qu'il m'a consacré.

Mes sincères remerciements vont bien sûr à Amélie Juhin pour son accueil bienveillant à l'Institut de Minéralogie et de Physique des Milieux Condensés de notre Université. Je lui suis redevable de m'avoir guidé pour mener à bien les calculs multiplets en champ cristallin, tant pour l'initiation théorique que pour la conduite des calculs numériques. Je la remercie aussi vivement, ainsi que Christian Brouder et Philippe Sainctavit, pour les discussions sur $Lu_2V_2O_7$.

Je remercie grandement Nicolas Jaouen, le responsable de la ligne SEXTANTS au synchrotron SOLEIL, et Alessandro Nicolaou, le scientifique de cette ligne pour leur soutien.

Sans échantillons de haute qualité, cette thèse n'aurait pas été possible. Que Haidong Zhou trouve ici mes remerciements pour ses monocristaux.

Un grand merci à Stephane Carniato et Patricia Selles pour m'avoir aidé à comprendre la théorie des groupes.

Mon ancien équipe, Francis Penent, Pascal Lablanquie, Lidija Andric, Jérôme Palaudoux et Mehdi Abdelbaki Khalal m'ont encouragé tout au long de ce travail.

Je ne saurais bien sûr oublier de remercier, déjà avec une certaine nostalgie, mes amis thésards, particulièrement Aladine Merhe, Antoine Desrier, Francois Risoud, Hang Liu, Meiyi Wu et Xuan Liu, et les post-doctorants du Laboratoire, qui ont donné une dimension humaine à ces trois années.

Mes remerciements vont aussi à mes proches, famille, belle-famille et amis (Tian Li, Peng Zhou), qui m'ont constamment supporté dans tous les sens du terme.

J'adresse mes profonds remerciements à ma chère épouse, Jipeng Luan, pour partager sa vie avec moi et m'avoir accompagné durant ces trois années difficiles. Je suis conscient que tu as souffert de la solitude à cause de notre relation à distance, et que tu t'occupes toute seule de notre fille. Je n'oublierai jamais toute l'énergie que tu as consacré pour me fournir la meilleure atmosphère de travail. Je n'oublierai jamais la motivation et le soutien que tu m'as apporté quand j'en avais besoin. Sans toi, je n'aurais pas fait tout ça. Je t'aime.

Table des matières

Résumé

Le problème des oxydes complexes d'éléments de transition $3d$

Ce travail de thèse porte sur l'étude expérimentale des excitations de basse énergie dans les oxydes complexes d'éléments de transition (CTMO, pour Complex Transition-Metal Oxides) par spectroscopies utilisant le rayonnement synchrotron. La technique principale que j'ai utilisé est la diffusion Raman résonante des rayons X, une technique connue aussi sous le nom de diffusion inélastique résonante des rayons X (ou RIXS, pour Resonant Inelastic X-ray Scattering).

La motivation de cette étude résulte des propriétés intrigantes des CMTO [1]. Par exemple, certains cuprates peuvent présenter une supraconductivité à "haute" température ; les manganites attirent aussi beaucoup l'attention à cause de leur magnétorésistance colossale ou de leurs propriétés multiferroïques. Dans un même CMTO, cette grande variété des propriétés physiques peut apparaître à la suite d'une modification fine, par exemple de la composition chimique, de la structure cristalline, de la température, de la pression, etc. L'origine de ce comportement provient des fortes corrélations électroniques qui résultent de l'extension spatiale réduite des orbitales de valence $3d$, impliquant une forte répulsion coulombienne entre ces électrons. La théorie quantique est essentiellement basée sur l'approximation à un électron, approximation qui n'est alors plus valable. Un des grands défis actuels de la Physique de la matière condensée est la compréhension de ces systèmes à électrons fortement corrélés, dont les CTMO font partie. Les excitations de basse énergie sont au cœur de la physique de ces systèmes. Leur cartographie est d'une importance cruciale, tant pour mieux connaître les forces motrices des propriétés physiques que pour confronter les modèles théoriques à l'expérience.

L'intérêt pour ces systèmes n'est pas seulement académique mais aussi technologique. Par exemple, grâce au couplage fort de l'aimantation et de la polarisation électrique dans les composés multiferroïques, on peut envisager de contrôler le magnétisme *via* un champ électrique, et *vice versa*, ce qui pourrait révolutionner les technologies de stockage de l'information ou des détecteurs.

La diffusion inélastique résonante des rayons X

La diffusion inélastique résonante des rayons X (RIXS) peut être simplement considérée comme une technique de "photon-entrant – photon-sortant" [2]. Deux processus s'y mêlent de façons différentes [2]. Au seuil $L_{2,3}$ des métaux de transition $3d$, le RIXS *direct* est dominant et permet de mesurer directement les excitations de type $d-d$ par des transitions dipolaires électriques des niveaux $2p$ vers $3d$.

Le RIXS peut être décrit comme la succession de deux étapes discrètes associées à des transitions dipolaires électriques : une absorption et une émission.

- **Première étape : absorption**
  Un photon avec une énergie $h\nu_{in}$ au voisinage de l'énergie de liaison d'un niveau du cœur de l'atome (i.e., à une résonance) est absorbé par le système qui est porté ainsi de son état fondamental $|i\rangle$ à un état excité, appelé l'état intermédiaire $|n\rangle$, avec une durée de vie de l'ordre de la femtoseconde.
- **Seconde étape : émission**
  L'état intermédiaire se désexcite radiativement soit vers l'état fondamental $|i\rangle$, soit vers des états excités $|f\rangle$ juste au-dessus de celui-ci. Si le système retrouve l'état fondamental, l'énergie du photon diffusé $h\nu_{out}$ est égale à celle de photon incident : c'est le processus de diffusion élastique résonante des rayons X. Sinon, le système se retrouve dans un état excité et une différence d'énergie ($\Delta E = h\nu_{in} - h\nu_{out} \neq 0$) apparaît entre le photon sortant et le photon entrant. Cette différence mesure une excitation spécifique du système.

Il est important de noter plusieurs points qui font du RIXS une technique expérimentale particulièrement puissante :

- **Le RIXS est une spectroscopie des états neutres.**
  Le nombre d'électrons est conservé dans le processus de diffusion. Il n'y a donc pas ionisation du système.
- **Le RIXS donne accès à des excitations sans changement de parité.**
  Les deux étapes d'absorption et d'émission intervenant dans le RIXS au seuil $L_{2,3}$ sont dipolaires électriques ($\Delta\ell = \pm 1$). La parité est donc conservée dans le RIXS, ce qui indique que l'on peut accéder à des excitations de type *d-d* ou bien *f-f*, sans restrictions imposées par la règle de sélection orbitalaire, comme par exemple dans l'absorption UV-visible.
  En outre, il faut noter qu'il n'y a pas trou de cœur dans l'état final du RIXS. Ainsi, la résolution de cette spectroscopie ne dépend que de la "monochromaticité" du photon incident et de la résolution instrumentale. En fonction des conditions, il devient en principe possible d'accéder non seulement à des excitations électroniques sur un site ou au transfert de charge ($\sim$ eV), mais aussi à d'autres excitations, comme les excitations de magnons ($\sim$ centaine meV) ou de phonons ($\sim$ dizaine meV).
- **Le RIXS est une sonde de l'état massif.**
  Si la spectroscopie des photoélectrons est une spectroscopie de surface en raison du faible libre parcours moyen des électrons (quelques dizaines d'ansgtröms) dans la matière, le RIXS est une spectroscopie de volume : le photon sortant a une énergie quasi égale à celle du photon entrant qui a lui même, dans le domaine des rayons X mous, qui est celui de ce travail, un libre parcours moyen de plusieurs milliers d'ansgtröms.
- **Le RIXS est chimiquement sélectif.**
  Ceci provient du caractère résonant de l'excitation et de ce que les électrons des atomes ont des énergies de liaison bien spécifiques. Par conséquent, les excitations observées lorsqu'un photon incident possède une énergie accordée à une énergie d'un niveau d'un atome donné seront propres à cet atome.

En dépit de ces atouts, les expériences de RIXS demeurent un tour de force car la section efficace du processus RIXS est extrêmement faible, en particulier dans le domaine des rayons X mous. C'est la raison pour laquelle cette spectroscopie ne s'est développée que récemment grâce à la disponibilité de sources de rayonnement synchrotron de $3^{\text{ème}}$ génération de haute brillance et au développement de spectromètres à haute résolution dédiés, comme le spectromètre AERHA (pour Adjustable Energy Resolution High Accep-

tance) développé et construit par le groupe de recherche dans lequel j'ai préparé ma thèse, et installé de manière permanente sur la ligne de lumière SEXTANTS du synchrotron SOLEIL.

Le synchrotron SOLEIL et la ligne SEXTANTS

Le synchrotron SOLEIL est un anneau de stockage dédié à la production de rayonnement entre 4×10^{-4} eV (μ-ondes) et 10 keV (rayons X durs). Après avoir été produits, les électrons sont accélérés par un "linac" et un "booster", puis injectés avec une énergie de 2.75 GeV dans l'anneau de stockage. La ligne SEXTANTS [3] a été conçue avec l'objectif de focaliser au mieux, et avec un flux optimal, pour un pouvoir résolvant supérieur à 10000, les photons X mous ($h\nu < 1500$ eV)) dans la perspective de mener, entre autres, des expériences de RIXS. C'est ainsi que le faisceau X éclairant l'échantillon a une taille de l'ordre de 2 µm (vert.) × 150 µm (horiz.).

L'instrument AREHA

L'instrument AREHA [4] est actuellement l'un des spectromètres RIXS les plus performants dans le monde dans la gamme des rayons X mous (50 eV – 1000 eV) avec un pouvoir résolvant entre 5000 et 8000 et une transmission pouvant être 10 fois supérieure à celle des autres instruments haute résolution. Il est notamment très bien adapté à l'étude des métaux de transition de la première série et des terres rares.

Cet instrument est composé des éléments suivants :

- **Chambre d'introduction/préparation**
  Une pré-chambre pour l'introduction des échantillons et leur conditionnement est attachée à la chambre d'analyse proprement dite. L'échantillon peut y être clivé ou gratté avec une lime en diamant, sous une pression de $\approx 1 \times 10^{-7}$ mbar.
- **Chambre d'analyse**
  Après préparation, l'échantillon est transféré dans la chambre principale d'analyse, où règne une pression inférieure à 5×10^{-9} mbar, sur un manipulateur (x, y, z, θ). Sur ce manipulateur, l'échantillon peut être refroidi par de l'hélium liquide jusqu'à une température de 15 K environ.
  Les mesures des spectres d'absorption (XAS, pour X-ray Absorption Spectroscopy) sont aussi faites dans cette chambre en mesurant le courant échantillon, c'est-à-dire en mesurant le photocourant total généré par la photoabsorption (dit Total Electron Yield mode ou TEY).
- **Chemin optique**
  De la source au détecteur, le chemin optique comporte deux miroirs concaves et un réseau gravé à nombre de traits variable. Le premier miroir sert à collecter les photons diffusés par l'échantillon et à obtenir une grande acceptance angulaire dans le plan horizontal. Il est suivi d'un miroir elliptique qui crée la source virtuelle du réseau de diffraction dispersant dans le plan vertical (en fait deux réseaux : l'un avec 450 traits/mm couvrant le domaine 50 eV – 500 eV et l'autre avec 1800 traits/mm couvrant le domaine 400 eV – 1000 eV.
- **Détecteur**
  Le détecteur est une caméra CCD à faible bruit et refroidie à l'azote liquide. Le spectre RIXS capté par la caméra CCD est une image dont on doit donner une signification physique en procédant à un étalonnage, c'est-à-dire faire correspondre,

pour une position particulière de la caméra, des numéros de pixel dans la direction de dispersion à des énergies vraies. Cet étalonnage est effectué en enregistrant une série de pics de diffusion élastique obtenus pour des énergies connues grâce au monochromateur de la ligne de lumière.

Matériaux étudiés

$TbMnO_3$ et $DyMnO_3$

Les multiferroïques sont des matériaux où coexistent une polarisation électrique (aussi appelé ferroélectricité) et un ordre magnétique [5]. Les multiferroïques conventionnels (dits de type I) présentent une forte ferroélectricité mais seulement un couplage magnétoélectrique faible. Récemment, une autre classe de multiferroïques, comme $TbMnO_3$ et $DyMnO_3$, a été découverte. Dans ces systèmes, l'apparition de la ferroélectricité est concomitante avec celle d'un ordre magnétique. Contrairement aux systèmes de type I, le couplage magnétoélectrique y est fort –ce qui rend ces composés très attractifs– mais leur ferroélectricité est faible –ces composés sont donc difficiles à employer dans des dispositifs réels. Le point d'intérêt de ces matériaux ne réside pas seulement dans les applications industrielles potentielles, mais aussi dans le défi qu'ils présentent pour expliquer le fait inattendu que la ferroélectricité apparaît conjointement à une transition d'ordre magnétique.

$TbMnO_3$ est l'un des matériaux multiferroïques de type II qui est le plus étudié. Nous le prendrons comme exemple "modèle" ici. Le mécanisme microscopique sous-jacent demeure une discussion ouverte, essentiellement entre deux modèles : l'interaction de Dzyaloshinskii–Moriya (DM) inverse [6] et la rotation du courant de spin (modèle KNB, d'après leurs auteurs Katsura, Nagaosa et Balatsky [7]). Le modèle DM décrit un mécanisme de déplacement atomique qui induit la ferroélectricité en raison de l'inclinaison du spin entre les voisins les plus proches. La modèle KNB explique un mécanisme de génération de la distribution de nuages électroniques polarisés sous un ordre magnétique en spirale. Ces deux modèles sont différents, mais ils impliquent la même conséquence. La polarisation électrique ($\vec{P}$) spontanée est proportionnelle au vecteur de translation du site i au site j, $\vec{r_{ij}}$, et au spin incliné entre les voisins les plus proches :

$$\vec{P} \propto r_{ij} \times (\vec{S_i} \times \vec{S_j}).$$

$TbMnO_3$ est une perovskite de structure orthorhombique (groupe d'espace *Pbmn*) dans laquelle la ferroélectricité apparaît spontanément lors de l'apparition d'un ordre magnétique en spirale. En fait, $TbMnO_3$ subit trois transitions de phase : d'abord, l'état paramagnétique passe à un ordre incommensurable antiferromagnétique (AF) avec une onde de spin sinusoïdale associée au manganèse suivant l'axe b à $T_N^{Mn} = 41\,K$; puis, l'ordre AF varie de sinusoïde incommensurable à spirale commensurable avec apparition de la ferroélectricité à $T_{lock}^{Mn} = 28$ K parallèle à l'axe c ; enfin, les moments magnétiques des ions Tb^{3+} s'ordonnent antiferromagnétiquement le long de l'axe a [8].

La structure cristalline n'est en fait pas celle d'une perovskite cubique parfaite. Le réseau présente une distorsion orthorhombique, dite de type $GbFeO_3$. Cette distorsion transforme l'octaèdre régulier MnO_6 en un octaèdre allongé, la direction d'élongation oscillant d'un octaèdre à l'autre. Le champ cristallin ressenti par le manganèse dépend non seulement de cette distorsion, mais aussi de la distorsion Jahn–Teller, les ions Mn^{3+} ayant la configuration électronique d^4 ($t_{2g}^3 e_g^1$).

Il est donc vraisemblable que l'origine de la ferroélectricité dans $TbMnO_3$ est très complexe. Elle pourrait faire intervenir conjointement des aspects des multiferroïques de type I et de type II. Un facteur crucial pour répondre à cette question est la valeur du champ cristallin au site Mn. En effet cette valeur peut servir comme point de référence pour les calculs de structure électronique car elle contient les corrélations électroniques effectives sur ce site [9, 10]. Par ailleurs, l'anisotropie magnétique d'un ion Mn^{3+} dépend explicitement de la démultiplication des états Mn $3d$ dans le champ cristallin ; elle joue donc un rôle central dans l'interaction d'échange antisymétrique qui gouverne les multiferroïques de type II [11, 12].

Champ cristalllin du manganèse

Les structures électroniques au seuil $L_{2,3}$ de Mn ($2p \rightarrow 3d$) et au seuil K de O ($1s \rightarrow 2p$) sont sondées par XAS et RIXS à la température ambiante et à 25 K. Le XAS est mesuré en mode TEY. La résolution en énergie globale pour le RIXS dans le cas de Mn $L_{2,3}$ (≈ 640 eV) est de 180 meV ; dans ces conditions, le fractionnement des niveaux d'énergie venant du champ cristallin peut être clairement observé dans les spectres RIXS.

Dans les calculs de multiplets avec champ cristallin [13], les paramètres du champ sont liés directement à la symétrie du site en jeu, un site de haute symétrie étant décrit décrit par un seul paramètre ; si la symétrie du site est plus faible, le nombre de paramètres considérés augmente.

En combinant les résultats expérimentaux de RIXS au seuil L_3 du manganèse à des analyses théoriques des spectres XAS et RIXS, nous pouvons paramétrer le champ cristallin ressenti par la manganèse dans $TbMnO_3$. Dans les calculs, la symétrie a été considérée comme approximativement D_{4h} à des fins de simplification numérique, même si le plan perpendiculaire à la direction d'élongation de l'octaèdre MnO_6 comporte deux liaisons Mn–O de longueur différente (1.89 Å et 1.95 Å). La configuration électronique de l'état fondamental de Mn^{3+} considérée est $3d^4$. L'effet du champ cristallin octaédrique entraine une levée de dégénérescence, le terme ^5D de l'ion libre se divise en un état t_{2g} et un état e_g, soit $t_{2g}^3 e_g^1$. Notons que la différence d'énergie t_{2g}–e_g correspond au paramètre $10Dq$ du champ cristallin. La déformation de l'octaèdre résultant de la distorsion abaisse la symétrie de O_h à D_{4h} selon notre approximation, ce qui nécessite l'introduction de deux paramètres de champ cristallin supplémentaires, Dt et Ds.

Les paramètres de champ cristallin trouvés dans ce cadre formel sont indiqués dans le Tableau 1 et permettent d'accéder à une image du potentiel électrique ressenti par l'atome de manganèse. Ceci devrait ouvrir la voie à des études quantitatives des déplacements atomiques contribuant à la polarisation électrique, ce qui peut jouer un rôle utile pour mieux connaître les mécanismes microscopiques en jeu.

Cette démarche a été aussi utilisée par caractériser le champ cristallin autour du manganèse dans $DyMnO_3$ [14] avec l'objectif supplémentaire d'étudier les effets du changement du rayon de l'ion de terre rare sur ce champ.

À partir de ces paramètres de champ cristallin, un diagramme d'énergie des états Mn $3d$ peut être construit, ce qui aide à comprendre les propriétés magnétiques et permet des confrontations avec les valeurs théoriques obtenues par d'autres approches. La différence faible de Ds entre $DyMnO_3$ et $TbMnO_3$ signifie que l'octaèdre MnO_6 possède une distorsion tétragonale plus importante dans $DyMnO_3$, donnant lieu à un diagramme de niveau d'énergie totalement différent pour ces deux composés. Un croisement est observé pour le niveau t_{2g} : dans $DyMnO_3$, l'énergie du niveau d_{xy} est supérieure à celle de d_{z^2}. En revanche, dans $TbMnO_3$, ces deux niveaux possèdent une énergie assez semblable, ce qui signifie la possibilité de la présence d'un échange orbital.

Champ cristalllin de la terre rare

Même si la structure cristalline et la structure magnétique sont similaires dans ces deux composés, la température de transition de phase est légèrement différente, ce qui suggère que la terre rare joue un rôle dans la détermination des propriétés physiques. Les travaux les plus récents sur $DyMnO_3$ laissent à penser que la contrainte d'échange symétrique entre les ions voisins R et Mn peut expliquer l'amélioration de la polarisation ferroélectrique dans $DyMnO_3$ ainsi que la ferroélectricité induite par le champ magnétique dans $GdMnO_3$ [15]. L'interaction de spin Dy–Mn contribue à la polarisation ferroélectrique à travers le mécanisme de couplage spin-réseau.

Afin d'étudier la structure électronique des terres rares, les spectres XAS et RIXS ont été mesurés aux seuils $N_{4,5}$ de Tb et Dy ($\approx 150\,\text{eV}$). La résolution en énergie globale du RIXS dans ce cas peut atteindre 50 meV avec le spectromètre AREHA. Avec cette résolution élevée, il est possible d'observer les effets du couplage spin-orbite sur les termes spectraux et donc d'étudier le champ cristallin de la terre rare.

Quant à l'orbitale $4f$ (la couche externe des ions terre rare), le couplage spin orbite joue un rôle important dans la levée de dégénérescence des niveaux énergétiques. Le champ cristallin est relativement faible par rapport au couplage spin orbite, donc les excitations de type f-f mesurées par RIXS sont données par les termes spectroscopiques atomiques. Ces excitations peuvent être identifiées à l'aide de la base de données des spectres atomiques du NIST. Néanmoins, certains légers décalages d'énergie existent entre la base de données et l'observation expérimentale, ce qui est dû au champ cristallin. Il est nécessaire de connaître les valeurs de ce faible champ cristallin quand nous étudions la structure électronique de la terre rare. La partie suivante a pour objectif de calculer ces valeurs.

Intégrales de Slater–Condon et valeurs de couplage spin-orbite (eV)

	$\|i\rangle$	$\|n\rangle$	$\|f\rangle$
F^2_{dd}	11.4151	12.2101	11.4151
F^4_{dd}	7.1481	7.6491	7.1481
G^2_{pd}	0.0	0.0592	0.0
ζ	0.0462	6.8452	0.0462

Paramètres de champ cristallin D_{4h} (eV)

$TbMnO_3$		$DyMnO_3$	
$10Dq$	1.60	$10Dq$	1.60
Dt	0.06	Dt	0.06
Ds	0.31	Ds	0.36

TABLE 1 – Valeurs des paramètres de structure électronique utilisés dans les calculs de multiplets avec champ cristallin pour simuler les spectres XAS et RIXS $L_{2,3}$ du manganèse (Mn^{3+}) avec la symétrie D_{4h} dans $TbMnO_3$ et $DyMnO_3$.

$Lu_2V_2O_7$

$Lu_2V_2O_7$ a une structure pyrochlore, où l'atome de vanadium se situe au sommet d'un tétraèdre constitué de quatre octaèdres VO_6, et l'atome de lutétium se place au centre de ce tétraèdre. Dans le ferromagnétique $Lu_2V_2O_7$ (température de Curie, $T_C = 70\,K$), les ions V^{4+} trivalents ne possèdent qu'un seul électron sur l'orbitale $3d$. Les trétraèdres dont ces ions occupent le centre ne sont pas distordus ; néanmoins, l'orientation relative de ces tétraèdres produit un champ cristallin trigonal, qui lève la dégénérescence des états t_{2g}.

Un effet Hall thermique anormal a été découvert dans $Lu_2V_2O_7$ et attribué à des excitations de spin (magnons) [16]. Notre objectif était de confirmer l'existence d'excitations de type magnon dont l'énergie prévue théoriquement était de $\approx 260\,meV$, donc accessibles par des mesures RIXS au seuil V $L_{2,3}$ avec AERHA. Nous n'avons pas été en mesure de confimer cette prévision théorique. Toutefois, il faut noter que la prédicition initiale était erronnée d'un ordre de grandeur (26 meV et non 260 meV) [17].

Les mesures RIXS au seil V $L_{2,3}$ nous ont cependant permis de faire la distinction entre les excitations orbitalaires locales et inter-site et d'apporter un regard nouveau sur la structure électronique du vanadium dans ce composé.

Comme on l'a vu, le vanadium V^{4+} a un seul électron sur la couche externe (configuration électronique $3d^1$) et il est dans un environnement octaédrique de six atomes d'oxygène (symétrie O_h). Une déformation systématique des VO_6 octahedra dans le pyrochlore produit un champ cristallin trigonal aux ions vanadium. Des mesures de diffusion des neutrons ont indiqué la présence d'un ordre orbitalaire et une structure ferromagnétique dans ce composé [18]. D'un autre côté, dans le cadre du modèle de Hubbard qui prend en compte les processus de sauts entre voisins les plus proches, les résultats montrent que la séparation du niveau d'énergie $3d$ a la même différence d'énergie que le résultat vennant du calcul du champs cristallin. L'état fondamental $3d^1$ est divisé en un état fondamental $^2A_{1g}$ et un état $^2E'_g$ (plus haut en énergie de 0.4 eV) ainsi qu'en un état ^2E_g (d'énergie encore plus élevée, soit 2 eV) [19].

La résolution énergétique globale des spectres RIXS est de 140 meV. Avec cette résolution, les spectres RIXS expérimentaux devraient révéler des formes spectrales discrètes. Mais, en fait, les spectres montrent une forme spectrale continue où les caractéristiques des excitations Raman ne sont pas nettement marquées, même si des excitations Raman peuvent être distingués à 0.4 eV, 1.8 eV et 2.7 eV. Une excitation Raman exotique au-dessus de 2 eV n'a pas pu être identifiée par le calcul en faisant appel à l'état unique V^{4+}.

Le spectre XAS $L_{2,3}$ de V dans $Lu_2V_2O_7$ ne révèle pas seulement la présence de V^{4+}. Sous le seuil V L_3, un pic semble être dû à V^{3+}, sur la base d'observations expérimentales faites sur d'autres oxydes de vanadium (e.g., V_2O_3, VO_2, V_2O_5) [20].

Pour interpréter les spectres RIXS au seuil $L_{2,3}$, des simulations, dans la théorie des multiplets en champ de ligand, des spectres XAS et RIXS pour chaque valence possible V^{3+}, V^{4+}, V^{5+} avec la symétrie de D_{3d} ont été effectuées. Les meilleures simulations correspondent au cas où il est fait appel à un mélange de valence ($V^{3+} : V^{4+} : V^{5+} = 1 : 2 : 1$), ce qui suggère l'existence d'un électron itinérant. Les intégrales de Slater utilisées sont les valeurs Hartree–Fock non réduites. Dans ce cadre, l'excitation Raman exotique au-dessus de 2 eV résulte de l'état trivalent V^{3+} (configuration électronique $3d^2$).

Conclusions et perspectives

Nous avons réussi à mettre en place le miroir collecteur dans le spectromètre AERHA (installé sur la ligne SEXTANTS du SOLEIL synchrotron) qui est désigné et développé

par notre équipe. Avec ce miroir, nous avons réussi à obtenir un gain d'intensité compatible avec la valeur théorique.

- **$RMnO_3$ (R = Tb, Dy)**
  En utilisant le spectromètre AERHA, nous avons mesuré les spectres XAS et RIXS au seuil $L_{2,3}$ de Mn, K de O, et $N_{4,5}$ de la terre rare (Tb, Dy) pour les deux composés similaires ($TbMnO_3$ et $DyMnO_3$). Les spectres de RIXS pour Mn et O montrent qu'il y a une superposition des pics venant des excitations orbitalaires. Cette observation expérimentale indique l'existence d'une forte hybridation entre Mn et O. Cela correspond aux résultats théoriques produits par le calcul de multiplets. Nous avons réussi à reproduire de manière théorique la forme de spectre XAS et la position des excitations de type *d-d* sur l'axe de perte d'énergie. Donc dans ce cas, nous avons bien paramétré le champ cristallin au site de Mn dans un modèle où Mn a un groupe ponctuel de symétrie D_{4h} et sans tenir compte de l'effet du transfert de charge. Les spectres de XAS et RIXS de la terre rare montrent une forte ressemblance avec le spectre atomique. L'effet du champ cristallin est certes faible, mais nous l'avons observé grâce à notre spectromètre qui a une de meilleures résolutions en énergie au monde (50 meV au seuil de la terre rare $N_{4,5}$).

- **$Lu_2V_2O_7$**
  En utilisant la même méthode, nous avons mesuré les spectres XAS et RIXS au seuil $L_{2,3}$ de V dans l'isolant de Mott-Hubbard $Lu_2V_2O_7$. Au lieu de trouver trois états discrets pour V^{4+}, nous avons trouvé une large bande que nous attribuons à la présence de V^{3+} et V^{5+}. Ceci pourrait être expliqué par la présence d'un électron itinérant dans $Lu_2V_2O_7$.

Chapter 1

Introduction

Over the past decades, strongly correlated electron systems have attracted massif attention of researchers, especially for complex transition metals oxides (CMTO) [1], due to numerous physical properties of interest, such as high temperature superconductivity. A typical characteristic of CMTO is that even a slight modification of the material, such as chemical composition, crystal structure, or a weak change of the external environment, like temperature or pressure, could trigger significant variations of physical properties. More precisely, cuprates and manganites, as major members of the CMTO family, exhibit colossal magnetoresistance. Recently, the search for multiferroic properties in rare earth manganites ($RMnO_3$) has become more intense, and it is the central topic of this thesis. Furthermore, type II multiferroics such as $TbMnO_3$ and $DyMnO_3$ presenting a fascinating behavior, the strong magnetoelectric effect, harbor a large potential in the industrial application such as numerical storage, detector, and spintronics. The microscopic mechanism experimentally behind of this phenomena was studied. Discussions of pertinent results will be presented in the following sections.

In an attempt to reveal the origin of these behaviors, spectroscopic studies of the electronic structure are necessary in order to investigate the role of correlation effects. These effects, which stem from the strong electron-electron interactions, are related to the reduced spatial extension of the $3d$ valence orbitals, implying a strong Coulomb repulsion between these electrons. Actually, the quantum theory is essentially based on the approximation of single electron, but in the case of multi-electrons system, this approximation is not valid anymore. As of today, understanding the strongly correlated electron systems is still a difficult challenge in condensed matter physics.

Thanks to the development of synchrotron radiation sources over the last past half-century, resonant inelastic X-ray scattering (RIXS) spectroscopy (with a fairly low scattering cross section) has become gradually a powerful tool to investigate the electronic structure with high energy resolution. X-ray absorption spectroscopy (XAS) probes unoccupied valence band states; it is regarded as a first step of RIXS measurements which give access to both occupied and unoccupied states. As will be shown in this thesis, the combination of both techniques provides new insights towards the understanding of strongly correlated systems. Measurement of low energy excitations (below a magnitude of 10 eV) by RIXS can reveal the intimate interactions among spin, orbital, lattice and charge orders. This experimental method has already displayed numerous success in fundamental physics, through measurements of the detailed electronic structure of various appealing materials, *e.g.*, like superconductors [21], Mott insulators [22], multiferroics [23] and topological insulators [24].

Nevertheless, experimental observations solely are not enough to elucidate complex quantum systems. Hence, theoretical analysis is a valuable approach to extract information from experimental observations. For instance, by supporting the interpretation of experimental XAS and RIXS spectra by crystal field multiplet simulations, the characteristics of the electronic structure in particular for $3d$ orbitals – the local crystal field as well as electron-electron interactions – can be understood quantitatively. These studies provide important findings to shed light on the enigma of fascinating material properties.

My main studies during the last three years, in the viewpoint of experiment and theory, were focused on the characterization of the electronic structure of $RMnO_3$ (R = Tb, Dy) and $Lu_2V_2O_7$ by XAS and RIXS. The thesis is organized in the following way:

- In Chapter 1, an introduction of type II multiferroics $RMnO_3$ (R = Tb, Dy) and of ferromagnet $Lu_2V_2O_7$ is provided.

- In Chapter 2, the experimental method and theoretical background of RIXS are detailed, where RIXS advantages are also listed.

- In Chapter 3, the principles underlying the theoretical CTM simulations are presented.

- In Chapter 4, the experimental and theoretical results obtained for $TbMnO_3$, $DyMnO_3$ and $Lu_2V_2O_7$ are discussed.

- The conclusions and perspectives are drawn at the end.

1.1 Type II multiferroics $RMnO_3$ (R = Tb, Dy)

Multiferroics are materials that possess, in the same phase, at least two "ferroic" properties: ferromagnetism (with spontaneous magnetic polarization $\vec{M}$), ferroelectricity (with spontaneous electric polarization $\vec{P}$), ferroelasticity (lattice modulation supporting the change of electric polarization) [25]. Fig. 1.1 illustrates their relationship, where piezoelectricity is present in the materials with ferroelasticity and ferroelectricity; magnetostriction is a magnetoelastic effect; magnetoelectricity is a behavior involving magnetic and electric interaction.

Magnetoelectricity was firstly predicted by Pierre Curie in 1894 [28]. Basically, the ferroelectric polarization $\vec{P}$ can be changed by an external magnetic field $\vec{H}$ and the ferromagnetic polarization $\vec{M}$ can be changed by an external electric field $\vec{E}$. This behavior is expected to be exploited for many applications such as magnetic field sensors and data storage, underlying the increasing interest for magnetoelectricity over the last decade. The rare-earth manganite, $RMnO_3$ (*e.g.*, R = Tb, Dy), is an archetype of perovskite with this multiferroic property. It exhibits a sharp increase of the magnetoresistance (colossal magnetoresistance) and weak ferroelectricity at low temperature.

Conventionally, magnetism appears in a material where transition metal ions have a partially filled d orbital (e.g., Fe, Co, Ni); the ferroelectricity is present in many materials of transition metal oxides where cations have an empty d orbital (e.g., $BaTiO_3$). This difference in d-electron number contradicts the coexistence of the mutual ferroelectric and ferromagnetic properties.

However, the d^0-ness rule is not the unique reason for apparent exclusion between fer-

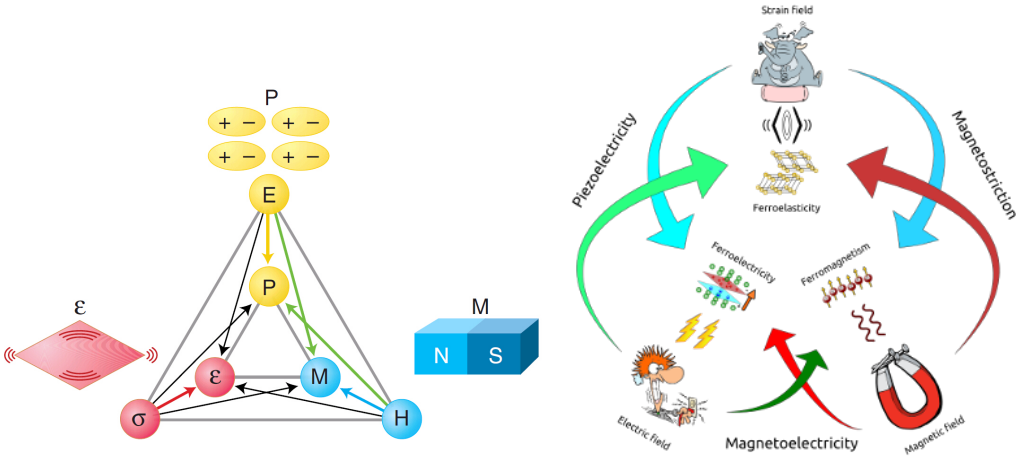

Figure 1.1: Schematic diagram of the relationship between multiferroics [26, 27], where the applied mechanic constraint, electric field and magnetic field are noted by σ, E and H, respectively; the ferroelasticity, ferroelectricity and magnetization are noted by ε, P and M, respectively.

roelectricity and magnetism. The prerequisites for the appearance of ferroelectricity are in fact a broken spatial-inversion symmetry ($\widehat{I} : r \to -r$) and an invariant time-reversal symmetry ($\widehat{T} : t \to -t$). In contrast, the pre-requisites for ferromagnetism are an invariant spatial-inversion symmetry and a broken time-reversal symmetry. Therefore, a simultaneous breaking of time-reversal and spatial inversion symmetries are requested in multiferroics systems in order to have magnetoelectricity (schematically shown in Fig. 1.2).

Magnetoelectric coupling present in a single-phase crystal was well described by Landau free energy F as follows:

$$\begin{aligned} F(\vec{E},\vec{H}) = F_0 &- P_i^S E_i - M_i^S H_i \\ &- \frac{1}{2}\epsilon_0\epsilon_{ij}E_iE_j - \frac{1}{2}\mu_0\mu_{ij}H_iH_j - \alpha_{ij}E_iH_j \\ &- \frac{1}{2}\beta_{ijk}E_iH_jH_k - \frac{1}{2}\gamma_{ijk}H_iE_jE_k - \cdots \end{aligned} \tag{1.1}$$

where, E_i, H_i represent an external electric and magnetic field of i-th component, respectively. The spontaneous electric polarization and magnetization in the material are denoted by P_i^S (with the unity of μC/cm^2) and M_i^S (with the unity of Bohr magneton μ_B), respectively. Based on Landau theory, the ferroelectricity/ferromagnetism is given by taking the derivative of the free energy F with respect to the electric/magnetic field. The electric polarization can then be expressed as:

$$\begin{aligned} P_i(\vec{E},\vec{H}) &= -\frac{\partial F}{\partial E_i} \\ &= P_i^S + \epsilon_0\epsilon_{ij}E_j + \alpha_{ij}H_j \\ &\quad + \frac{1}{2}\beta_{ijk}H_jH_k + \gamma_{ijk}H_iE_j + \cdots \end{aligned} \tag{1.2}$$

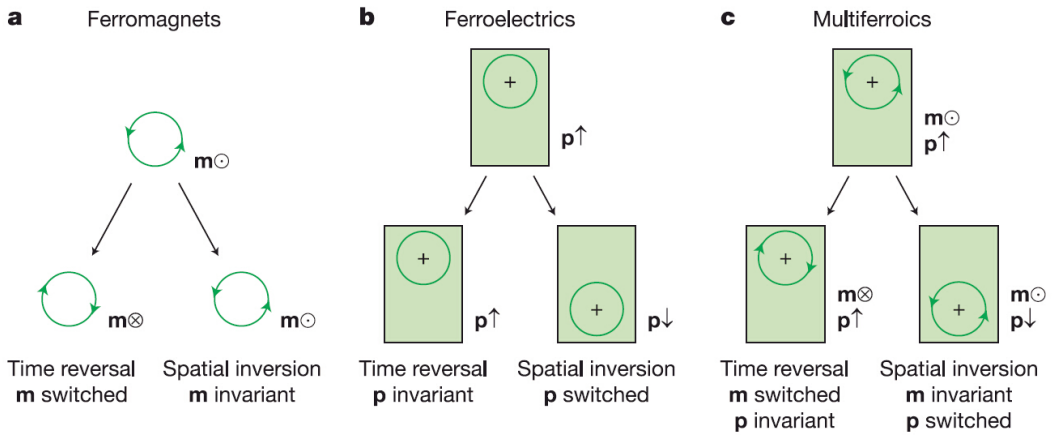

Figure 1.2: Schematic diagram of time-reversal and spatial inversion symmetries in ferroics, where the letter **m** and **p** denote magnetization and electric polarization, respectively [5].

and magnetization by:

$$\begin{aligned} M_i(\vec{E},\vec{H}) &= -\frac{\partial F}{\partial H_i} \\ &= M_i^S + \mu_0\mu_{ij}H_j + \alpha_{ij}E_i \\ &\quad + \beta_{ijk}E_iH_j + \frac{1}{2}\gamma_{ijk}E_jE_k + \cdots \end{aligned} \tag{1.3}$$

where, ϵ_0 and μ_0 represent the permittivity and permeability of free space. The relative permittivity and permeability are denoted by the tensors ϵ_{ij} and μ_{ij}, respectively. The linear magnetoelectric coupling coefficient corresponds to α_{ij}. β_{ijk} and γ_{ijk} can be totally neglected in multiferroics systems since they are magnetoelectric coefficients of quadratic order. Multiferroics with magnetoelectricity have large permittivity as well as permeability, hence they exhibit an important magnetoelectric effect. However, the upper bound on electromagnetic susceptibility can be given as [29]:

$$\alpha^2 \leq \epsilon_0\mu_0\epsilon_{ij}\mu_{ij} \tag{1.4}$$

where, a large ϵ_{ij} is neither a necessary nor a sufficient condition for stating that a material has multiferroic properties. It was reported that the relative permittivity reaches 25 in ferroelectric KNO_3 around the T_C ($\sim$120 C°) [30] and even higher than 5×10^4 in paraelectric $SrTiO_3$ at low temperature [31].

Based on the Landau theory, the linear response between the electric polarization (P) and the applied magnetic field (H) or between the magnetization (M) and the applied electric field (E) are given in the first order in Eq. (1.2) and Eq. (1.3), respectively. These linear responses offer a large amount of application possibilities, since even a weak applied external field is still able to vary an internal magnetic/electric order state, due to strong magnetoelectric coupling.

Actually, the strong magnetoelectric coupling does not exist in all multiferroic materials. Multiferroics are generally classified into two families, type I and type II, depending on the origin of ferroelectricity. A famous prototype of type II multiferroics is $TbMnO_3$, its ferroelectricity (8×10^{-4} C/m^2 at $\sim$ 10 K) arises when the magnetic structure has the cycloid magnetic order. Type I multiferroics have a large ferroelectricity at high temperature.

For instance $BaTiO_3$ reaches 2.6×10^{-2} C/m^2 at 296 K. In $BaTiO_3$, the electric polarization originates from the ionic displacement of Ti^{4+} in the TiO_6 cluster, and it appears along with ferromagnetic order. Therefore, in general, the ferroelectric polarization and the associated ordering temperature are significantly lower in type II multiferroics when compared to type I multiferroic materials. However, the magnetoelectric coupling present in type II multiferroics is stronger than in type I multiferroics. Because of a strong magnetoelectric (ME) coupling presented in the multiferroics $TbMnO_3$ and $DyMnO_3$, these compounds have a large application potential.

Fig. 1.3 illustrates the phase transitions of orbital and magnetic ordering of Mn in $RMnO_3$ (space group Pbnm). At low temperature, orbital order is present, but the spin order is frustrated, forming a complicated magnetic structure. The electronic configuration of Mn^{3+} ions with high spin is $|t_{2g}^3 e_g^1\rangle$, where the e_g states form a staggering orbital ordering of $d_{3x^2-r^2}$ and $d_{3y^2-r^2}$ [33]. Actually, the orbital ordering of the half-filled triplet orbital t_{2g} is quenched and therefore, the single e_g electron located on a degenerate state gives rise to an anisotropic electronic distribution [34], due to Jahn-Teller effect. This anisotropic $3d$ electronic distribution (called orbital ordering) is always present in the rare-earth manganite series [35, 36], where the degree of freedom of orbital ordering depends on the atomic radius of rare-earth (or the Mn-O-Mn bond angle ϕ). In the case of $RMnO_3$ with R = Tb, Dy, there are two magnetic phase transitions at Mn site. The first phase transition occurs at T_N, from a paramagnetic state to an incommensurate antifer-

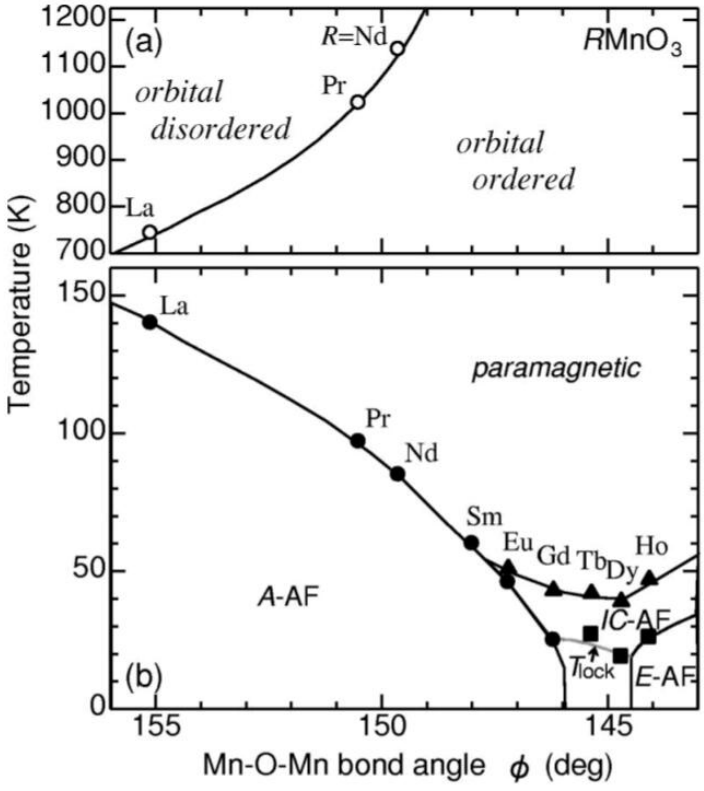

Figure 1.3: Diagram of orbital (a) and spin (b) ordering versus sample temperature, T, for rare-earth manganite series as a function of the temperature and Mn-O-Mn tilt angle along the zig-zag chain [32].

romagnetic (IC-AF) state with a longitudinal modulated pattern (see. Fig. 1.4 a). The second transition appears at T_{lock} and leads to a phase transition featuring an elliptical spinal magnetic pattern (see. Fig. 1.4 b), and a spontaneous electrical polarization ($\vec{P}//c$) .

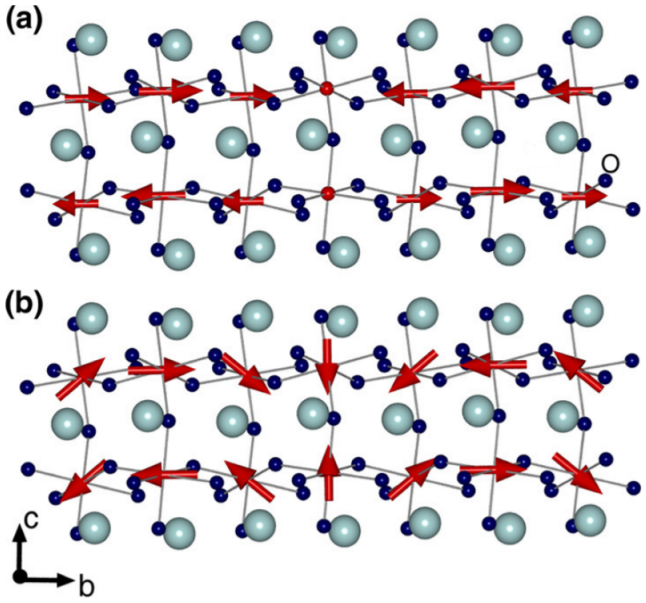

Figure 1.4: Magnetic structure pattern cut through the bc plan of the orthorhombic crystal structure of $RMnO_3$ (R = Tb, Dy) showing (a) the magnetic ordering of Mn below $T_N = 42$ K, and (b) the cycloid ordering below $T_{lock} = 28$ K. Red arrows indicate the orientation of the magnetic moment at the Mn site [37].

Recently, the colossal magnetoresistance (CMR) has been discovered in mixed valence manganites $R_{1-x}A_xMnO_3$ (R = rare earth, A = Ba, Ca, Sr, Pb). In such compounds, with Mn ions having mixed valence, charge ordering is present. This intriguing physical property triggered a significant discussion about the fundamental microscopic mechanism in pure $RMnO_3$. The microscopic mechanisms for the magnetic structure were proposed in various multiferroic materials, [38, 15, 39], however, the interest for this class of multiferroics remains unaltered. *Ab initio* density functional theory (DFT) was used to investigate the ferroelectricity induced by ionic displacements. Using the model of femtoscale magnetically induced lattice, Walker [40] concluded that a theoretical value of $P = 176\ \mu Cm^{-2}$ is close to a third of the obtained experimental value of $P \approx 600\ \mu Cm^{-2}$. Clarifying the microscopic mechanism of cycloidal magnetic order induced ferroelectricity in $TbMnO_3$ and $DyMnO_3$ is still a challenge for theory.

1.1.1 $TbMnO_3$

Background

The magnetic structure of Mn in the $TbMnO_3$ varies with the temperature. At $T_N \approx$ 41 K, Mn exhibits a phase transition from a paramagnetic state (at room temperature) to an antiferromagnetic state. At long range, the magnetic structure of Mn is characterized by a AF sine-wave ordering along b-axis as shown in Fig. 1.5. Of particular interest for this multiferroic material is the difference from magnetic structure of either the A-type AF (*e.g.*, $LaMnO_3$ [41]) or E-type AF (*e.g.*, $HoMnO_3$ [42]). The magnetic structure of Mn were investigated using neutron diffraction measurements [43] on powder and single crystal samples (group space Pbnm), where the wave vector of the Mn magnetic structure is denoted as $(0, k_s, 0)$. The wavenumber k_s is equal 0.295 at T_N and decreases during the cooling process. k_s component is almost locked at the constant value 0.28 below T_{lock}=27 K. Therefore, an incommensurate to "commensurate" (lock-in) phase transition arises in the magnetic structure of Mn, and the magnetic moments of Mn present a cycloid spin ordering at long range.

In addition, since the relative atomic displacement is related to electronic polarization in a unit cell (*e.g.*, MnO_6 cluster), the crystal structure of the different magnetic phases is relevant. X-ray diffraction measurements on a single crystal show additional superlattice peaks at $(0, k_l, l)$ below T_N, where l is an integer. The $TbMnO_3$ wave vector k_l of 0.57 at T_N and of quasi-constant 0.55 below T_{lock} were measured along $(0, k_l, 3)$ by X-ray diffraction. These phenomena imply the presence of atomic displacement with presence of magnetic ordering, where this displacement is magnetoelastically induced by the sinusoidal AF order of Mn. This distortion in the crystal can be explained by exchange striction [44].

According to Kimura [8], the appearing of the superstructure peaks in the measurement

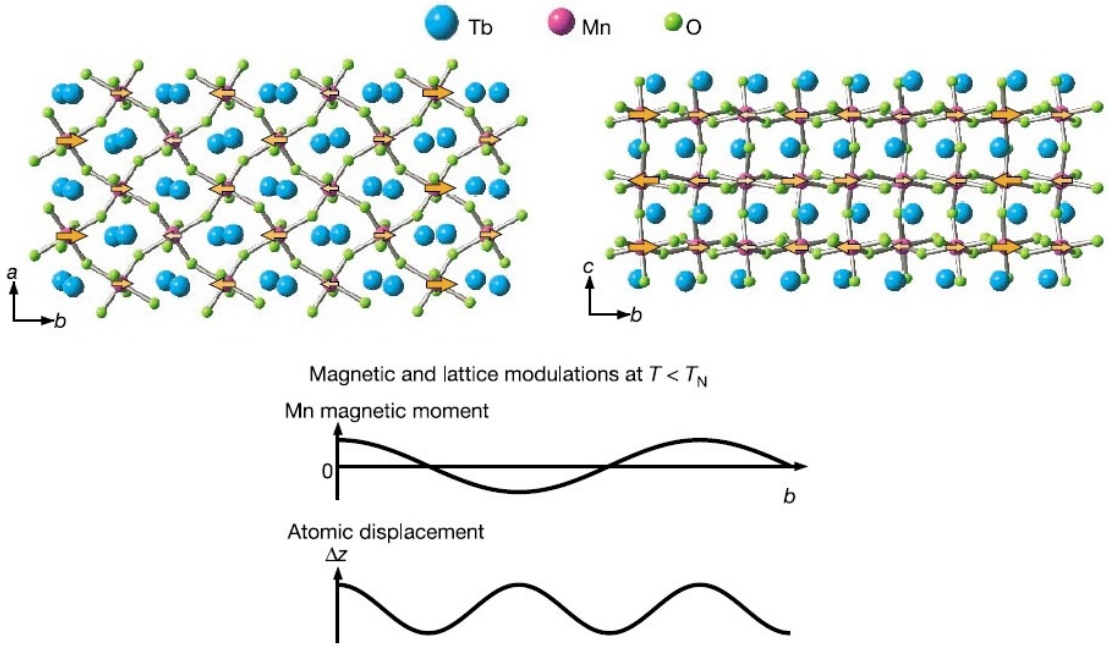

Figure 1.5: Magnetic structure in ab and bc plan, where antiferromagnetic sine-wave order is along b axis in the space group Pbmn at temperature below T_N, of Mn in multiferroics $TbMnO_3$ and atomic displacement due to magnetic striction [8].

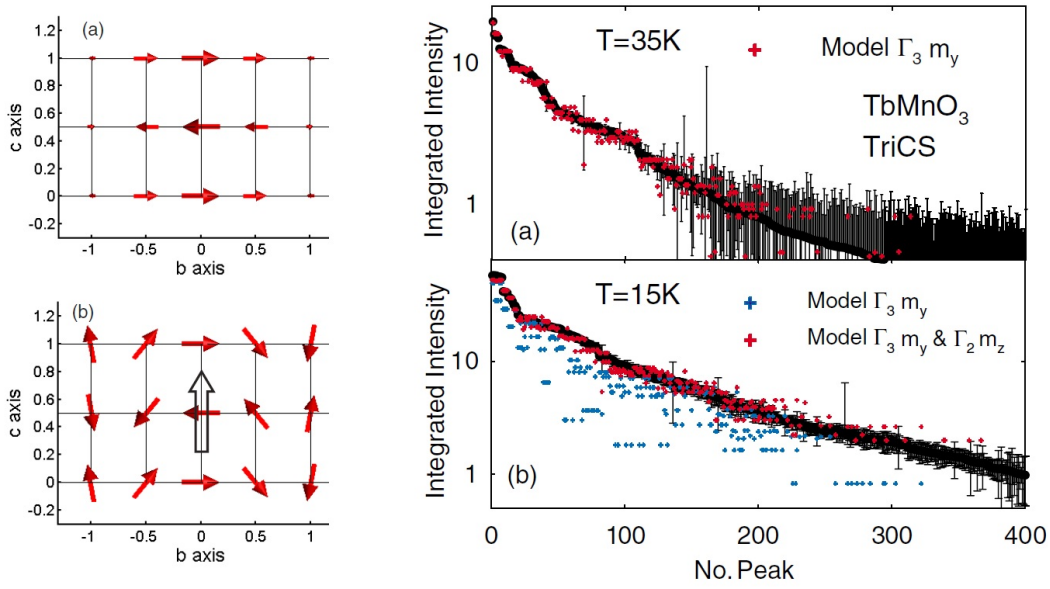

Figure 1.6: Magnetic structure in the bc plan and integrated intensity measured by neutron diffraction shown in (a) and (b) are taken at 35 K ($T_{lock} < T < T_N$) and 15 K($T < T_{lock}$), respectively. Simulation results (noted by +) are compared with experimental observation in the right panel, where the Γ_i is according to the irreducible representation [38].

of magnetic structure by using neutron diffraction [43] on one hand, and crystallographic distortion at magnetic ordering [32] on the other hand, attests that ferroelectricity might be due to the incommensurate to commensurate (less ordered state to more ordered state) phase transition [44], which leads to a displacement of atoms. We expected to observe the variation of electronic structure that appears upon crystal distortion. This study is helpful to reveal the origin of the ferroelectricity induced by magnetoelectronic coupling.

However, by combining experimental observations (neutron diffraction) and theoretical analysis (Laudau free energy), Kenzelmann [38] demonstrated that: (1) incommensurate to commensurate phase transition does not unambiguously happen at T_{lock}; (2) the emergence of ferroelectricity is completely irrelevant to the commensurate or incommensurate phase; (3) ferroelectricity appears owing to the magnetic structure of particular variation (see. Fig. 1.6). Further, the sinusoidal spin ordering at T_N cannot break the spatial inversion symmetry, hence ferroelectricity cannot be present in the system. In contrast, the elliptic spiral Mn moments ordering breaks inversion symmetry. The magnetic structure of Mn is identified by fitting under the irreducible group [38].

Despite the fact that several scenarios for individual materials have been proposed over the past decades [45, 46, 47], a common microscopic quantum theory of magnetoelectric effect is still missing. Currently, there are three models to describe electromagnetic coupling in the multiferroics system: the antisymmetric Dzyaloshinskii–Moriya (DM) model [6], the spin current model (called also KNB model) [7], and the electric current cancellation model [48].

The antisymmetric Dzyaloshinskii–Moriya model, takes into account some key ingredients (double-exchange, superexchange, DM interaction [49, 50] as well as the Jahn-

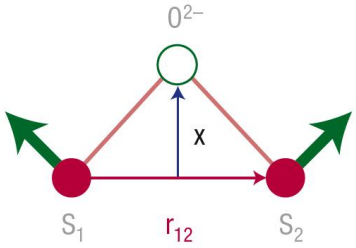

Figure 1.7: Scheme of the Dzyaloshinskii–Moriya interaction, where the green arrow indicates the direction of magnetic moment at the Mn site, x is the atomic displacement of the O ligand, the distance between nearest neighbors of Mn noted as r_{12} [51].

Teller effect) and describes the microscopic mechanism for the incommensurate antiferromagnetic (IC-AF) order induced ferroelectricity. In the Hamiltonian of orthorhombic multiferroic manganite system [6], the DM interaction term is written as:

$$H_{DM} = \vec{D}_{ij} \cdot (\vec{S}_i \times \vec{S}_j), \tag{1.5}$$

where $\vec{D}_{ij}$ is a Dzyaloshinskii vector, $\vec{S}_i$ is the moment at ith site. Assuming that the Mn site is fixed and only O moves, the Dzyaloshinskii vector is proportional to the vector product between the relative atomic displacement of O^{2-} ($\vec{x}$) and the rotation axis of the local spin, $\vec{D}_{12} = \vec{x} \times (\vec{u}_{S_1} \times \vec{u}_{S_2})$ as shown in Fig. 1.7. DM interaction plays a major role in stabilizing the helical magnetic structure and can be considered as a correction effect related to the superexchange in the asymmetric system. It gives an important contribution in ferroelectricity through the electroelastical displacement upon exchange striction effect.

The spin current model was proposed by the Katasura, Nagaosa and Balatsky, hence it is also called KNB model. In this model, a gauge interpretation is introduced within the Heisenberg spin Hamiltonian for the superexchange, therefore the DM interaction effect is hidden in the imaginary part of a supercurrent and plays the role of vector potential or gauge field in the spin current [7]. Briefly, the electric polarization written as $\vec{P} \propto \vec{e}_{ij} \times (\vec{S}_i \times \vec{S}_j)$, is proportional to the product vector between the unit vector directed from the site i to j, $\vec{e}_{ij}$, and the product vector of rotation axis of spins, $\vec{S}_i \times \vec{S}_j$.

The electric current cancellation model is the least referred model among the three. Upon the non-relativistic dynamic Maxwell equations, an electric current can induce directly a magnetization. The magnetoelectric coupling is induced by the electric current cancellation. The multiferroics are requested to be an unconventional insulator, namely Mott insulator where the strong electron-electron coupling results in a band splitting. Moreover, the external shell should not be completely filled.

Until now, the microscopic mechanism of ferroelectricity is still under discussion mainly between two recognized mainstream models, namely spin current (KNB model) [7] and antisymmetric Dzyaloshinskii–Moriya [6]. Ferroelectricity appears among the c axis while the magnetic ordering becomes cycloid at long range. In fact, the cycloid magnetic order breaks the spatial inversion symmetry and therefore it induces this spontaneous electric polarization. The intimate link between the magnetic structure and ferroelectricity is

commonly established as:

$$\vec{P} \propto \sum_{i,j} \vec{e}_{i,j} \times \left(\vec{S}_i \times \vec{S}_j\right).$$

However, ion displacement plays a crucial role in the breaking of spatial inversion symmetry, to date there is not yet a convincing evidence to end this discussion. Actually, the KNB model is generally accepted in the world for studying the microscopic mechanism of magnetoelectric effect induced ferroelectricity [7, 51].

With the aim to contribute to the discussion about the microscopic mechanism of ferroelectricity in $RMnO_3$, we expect to estimate the energy of atomic displacement and electron cloud movement in a crystal field. Identifying this crystal field is necessary to realize this final goal and it is the main work performed during this thesis.

In order to figure out the crystal field, it is important to start from the description of the crystal structure. In the case of the MnO_6 cluster in $TbMnO_3$, the six surrounding O ligands impose the crystal field at the Mn site. Table 1.1 lists the crystal structure parameters and the position of O^{2-} ligands. The ligand positions in Cartesian coordinate system display a strong crystal distortion that is expected lead to XAS spectra with polarization dependence in a non-magnetic material. To simulate these XAS spectra, we take into account both MnO_6 clusters (notated as α-MnO_6 and β-MnO_6) with different orientations. Through translation of these two MnO_6 clusters, one can construct the main crystal structure of $TbMnO_3$. Structurally, these two clusters have identical Jahn-Teller distortion with elongation mode. The adjacent angle of O-Mn-O remains 90° even in a strong Jahn-Teller effect at Mn site. In each cluster, the point group symmetry at the Mn site is actually D_{2h}. However, the distances between O-Mn-O contained in the perpendicular plane to the main rotation axis are very close. Therefore, the point group symmetry is approximated as D_{4h} in all my theoretical calculations. This approximation is to simplify the difficulty of describing a low symmetry coordination, which requests further crystal field parameters. Moreover, the calculations in the doped system $La_{0.5}Sr_{1.5}MnO_4$ demonstrate that the results with D_{4h} crystal field with are very similar to D_{2h} [34].

Experimentally, we investigated the electronic structure of Mn $L_{2,3}$ edge of orthorhombic $TbMnO_3$ single crystal [with surface orientation (001) in the space group of Pbnm] by using both XAS and RIXS. For XAS, the polarization dependence in XAS Mn $L_{2,3}$ edge is already observed in the orthorhombic $TbMnO_3$ single crystal [52] and in the hexagonal $TbMnO_3$ thin film [53]. We expected to observe this polarization dependence in XAS Mn $L_{2,3}$ edge of orthorhombic $TbMnO_3$ single crystal by rotating the sample. For RIXS, our electronic structure investigation at Mn L_3 edge of $TbMnO_3$ is the first study ever performed. The RIXS spectra at Mn K threshold measured by Chen [23] show merely three prominent RIXS features at the energy loss of 2.9, 7, and 11 eV, respectively. The broad and intense elastic peak might cover the others d-d excitations below 2.9 eV.

It was expected to figure out the crystal field at Mn site by a reliable approach, namely crystal field multiplet calculations (see Chapter 3). Over the past decades, the orbital ordering is still argued along either $d_{3z^2-r^2}$ or $d_{x^2-y^2}$ in $LaMnO_3$. Indeed, the orbital ordering is dependent on the occupied orbital of splitted e_g. From the viewpoint of first principles calculations [54], the ground state is orbitally ordered with a staggered order of $x^2 - r^2$ and $y^2 - r^2$. However from the viewpoint of crystal field multiplet calculations [55], the $d_{3z^2-r^2}$ possesses a lower energy level than $d_{x^2-y^2}$, hence the orbital ordering should be found among $3z^2 - r^2$ orbitals. However, crystal field multiplet calculations

Lattice parameters			
	a	b	c
	5.30300 Å	5.83000 Å	7.41400 Å
Atomic coordinates			
Element	x	y	z
Tb1	0.98360	0.08000	0.25000
Mn1	0.50000	0.00000	0.00000
O1	0.10400	0.46380	0.25000
O2	0.70240	0.32930	0.05210
α-MnO_6 cluster			
O2	1.29760	0.67070	0.94790
O2	0.70240	0.32930	1.05210
O1	1.10400	0.46380	1.25000
O1	0.89600	0.53620	0.75000
O2	0.79760	0.82930	1.05210
O2	1.20240	0.17070	0.94790
β-MnO_6 cluster			
O2	0.20240	1.17070	0.94790
O2	0.79760	0.82930	1.05210
O1	0.60400	1.03620	0.75000
O1	0.39600	0.96380	1.25000
O2	0.29760	0.67070	0.94790
O2	0.70240	1.32930	1.05210

Table 1.1: Structure parameter and ligand position from VESTA [56], where the ligand position of α-MnO_6 and β-MnO_6 clusters are randomly chosen, but these two types of clusters have a specific orientation of C_4 axis.

cannot be compared in a straightforward way to first principles calculations.

This work is focused on the determining the crystal field parameters (the reduction factor of Slater integrals and spin-orbital coupling, $10Dq$, Dt and Ds). From these three crystal field parameters, $10Dq$, Dt and Ds, one should be able to establish a diagram of energy level to describe the orbital ordering.

1.1.2 $DyMnO_3$

Background

In the previous section, a few physical properties in the view of crystal structure and magnetic structure for $TbMnO_3$ are listed. The mentioned theoretical models apply also to $DyMnO_3$. Indeed, $DyMnO_3$ ($Z_{Dy} = 66$ with electronic configuration $[Xe]4f^{10}6s^2$) is an analogical compound to multiferroic $TbMnO_3$ ($Z_{Tb} = 65$ with an electronic configuration $[Xe]4f^96s^2$). Both compounds harbor quasi-identical chemical and physical properties. Dysprosium has a trivalent state, as terbium in $TbMnO_3$. This means that the electronic configuration of the ground state of Mn^{3+} is $|3d^4\rangle$. A strategy similar to the one used for $TbMnO_3$ can be proposed for the investigation of $DyMnO_3$.

The energy level splitting of Mn is due to the existence of the crystal field (an electric potential field), which is generated by the surrounding O ligands. Within the O_h symmetry, the electronic states are described by a triplet t_{2g} (d_{xy}, d_{xz} and d_{yz}), and a doublet e_g ($d_{x^2-y^2}$, $d_{3r^2-z^2}$). The crystal field is quantitatively defined by the value of parameter $10Dq$. Generally, $10Dq$ is between 1-2 eV for oxide compounds. The $10Dq$ represents the energy difference between both single-particle states ($10Dq = \Delta_0 = \varepsilon_{e_g} - \varepsilon_{t_{2g}}$), also called splitting energy. Taking into account the Jahn-Teller distortion, a further energy level splitting appears and it depends on two new parameters Ds and Dt, which quantify the distortion effect in terms of the electric potential. The presence of a strong Jahn-Teller effect in the MnO_6 octahedra lifts the degeneracy of e_g and reduces the symmetry from O_h to a distorted cluster with low symmetry, *e.g.*, D_{4h}. In the same time, the orbital ordering appears. The tetragonal distortion splits the doublet e_g into $d_{3z^2-r^2}$ and $d_{x^2-y^2}$, while triplet t_{2g} splits into d_{xy} and doublet $d_{xz,yz}$. Considering that the half-filled t_{2g}^3 state has no orbital degeneracy, the orbital degree of freedom is only related to e_g^1 electron. This phenomenon of orbital ordering is ascribed to a cooperative Jahn-Teller effect, which was

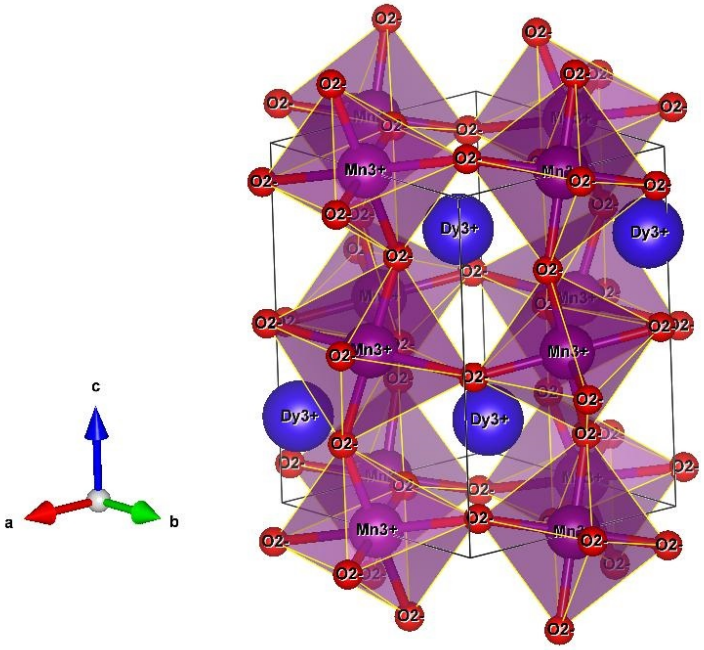

Figure 1.8: Orthorhombic crystal structure of $DyMnO_3$ in the space group Pbnm No. 62.

Element	x	y	z
Dy^{3+}	0.98260	0.08248	0.25000
Mn^{3+}	0.50000	0.00000	0.00000
O^{2-}	0.11400	0.46300	0.25000
O^{2-}	0.20100	0.17300	0.55340

Table 1.2: Structure parameters of orthorhombic $DyMnO_3$ in the space group Pbnm, No. 62.

discussed by Kanamori in Ref. [57].

In the Pbnm (No. 62) orthorhombic space group, the lattice parameters of $DyMnO_3$ [58] are $a = 5.280\,\text{Å}$, $b = 5.842\,\text{Å}$, $c = 7.378\,\text{Å}$. The positions of each atom are listed in the Tab. 1.2. The crystal structure of $DyMnO_3$ shown in Fig. 1.8, illustrates that the MnO_6 cluster has a quasi identical mode as in $TbMnO_3$. There are one long ($l_1 = 4.441\,\text{Å}$) and two short ($l_2 = 3.904\,\text{Å}$ and $l_3 = 3.830\,\text{Å}$) distances among the three O-Mn-O chains. The O-Mn-O chain in the cluster MnO_6 with symmetry D_{2h} remains 90°, and both short lines have a similar distance, allowing to approximate the symmetry at Mn site as D_{4h} in the crystal field multiplet calculations. The C_4 axis in cluster MnO_6 has two different orientations, which are taken into account in the calculations of XAS spectra with polarization dependence. Jahn-Teller effect at the Mn site leads to the elongated distortion (as shown in Fig. 1.9), modulating the crystal field.

The magnetic structure of $DyMnO_3$ is difficult to be measured by the neutron scattering technique, because the Dy element has an important cross section [32]. Hence, its magnetic structure is mainly inferred from X-ray magnetic resonant scattering and diffraction [14]. It undergoes three phase transitions: below $T_N = 39$ K, the moment of Mn at long range forms an incommensurate sinusoidal AF ordering with a wave vector $(0, 0.36, 0)$;

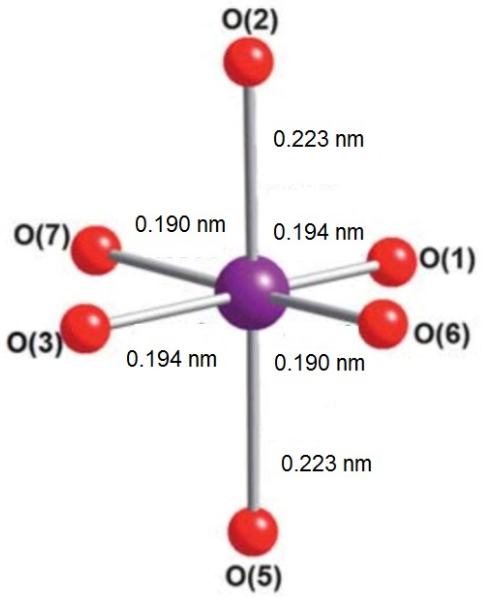

Figure 1.9: Structure of MnO_6 cluster in $DyMnO_3$ [59].

secondly, the magnetic order transfers into a commensurate cycloid AF ordering with a wave vector $(0, 0.39, 0)$ with decreasing T below $T_{lock} = 18$ K; thirdly, the moment of Dy gives rise to the magnetic order with a propagation vector $(0, 0.5, 0)$ when the temperature is decreased reaching $T_N^{Dy} = 5$ K. For a bulk mono-crystal of $DyMnO_3$, the emergence of superstructure should be due to magnetoelastical strain under the magnetic phase transition below T_{lock} [60]. The magnetic structure of $DyMnO_3$ is highly similar to the one of $TbMnO_3$.

1.1.3 Comparison of $DyMnO_3$ and $TbMnO_3$ - role of the rare earth

$DyMnO_3$ and $TbMnO_3$ display similar physical behaviors. However, there is a difference between them below T_{lock} in the applied external magnetic field. In $TbMnO_3$, the polarization flop ($P \parallel c \rightarrow P \parallel a$) shows a transient variation. Nevertheless, in $DyMnO_3$, the polarization flop gradually and continuously varies during transition [61]. The Coulomb interaction, as well as the stereo-repulsion, are likely to play an important role in the $RMnO_3$ series.

By using Raman spectroscopy, the phonon modes have been identified in Ref. [62]. For $TbMnO_3$, the stretching $A_g(1)$ and bending $A_g(3)$ modes (as shown in Fig. 1.10) are strongly mixed. For $DyMnO_3$, Raman spectroscopy shows that the bending mode has a higher frequency than the stretching mode, indicating crystal distortion. The vibration modes presented in $RMnO_3$ series may have a direct link to the ferroelectricity or CMR [62].

In recent papers, the spontaneous magnetic ordering of Tb [38] and Dy [15] was observed when the temperature is above the Néel temperature of rare-earth, $T_{Néel}^R$. In this condition, an interaction (attraction or repulsion) between neighboring rare-earth and Mn could bring out symmetric exchange striction [64].

Recent studies of dichroism at the Tb $M_{4,5}$ threshold illustrate that the contribution

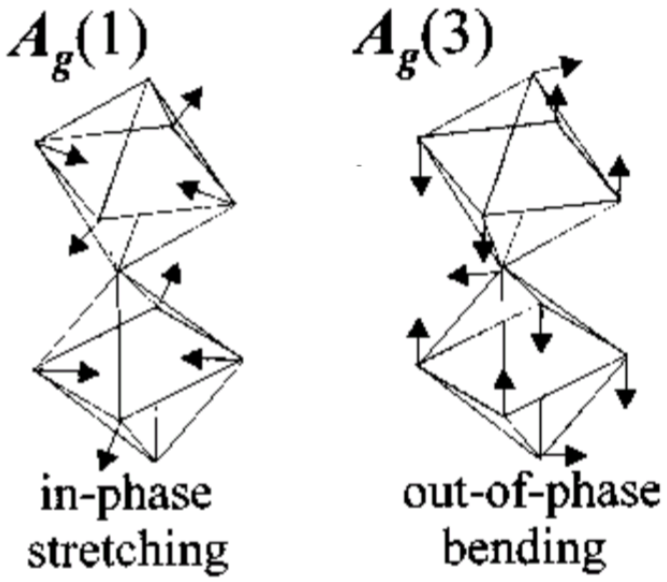

Figure 1.10: Raman allowed phonon modes for perovskite $RMnO_3$ compounds [63].

from the Tb magnetic order to the electric polarization in $TbMnO_3$ cannot be ignored [65]. This observation, in orthorhombic multiferroics $RMnO_3$, points out that moments of the rare earth may play an important role in the ferroelectricity. It may also open up a simple route to enhance the ferroelectricity in multiferroics. Therefore the investigation of local electronic f-f excitations on rare-earths site is important in the above mentioned compounds.

To date, the role of rare earth in the multiferroics $RMnO_3$ is not well understood. The $4f$ electronic energy levels are usually studied using optical spectroscopy, where the energy of light source ranges from the infrared to the ultraviolet. These techniques generally have a high energy resolution. For instance, one can probe the hyperfine electronic structure [66] in the solid state. However, because of the lack of element selectivity in optical spectroscopy, the transitions are difficult to identify.

The analysis of spectroscopic results for the rare earth $4f$ orbital is best resumed as follows:

> *"What appears to be unique in solid-state rare earth spectroscopy is that the electronic energy level structure is established primarily using the quantum theory of atomic spectroscopy, and all collective solid-state effects can be treated as a perturbation known as the crystal-field interaction."*
> – cited from *the Spectroscopic Properties of Rare Earths in Optical Materials.* [67]

In fact, because the electrons in $4f$ orbitals are localized, Hund's rule plays a crucial role in the energy level splitting of $4f$ levels (as shown in Fig. 1.11). This is totally antithetic to the (more) delocalized $3d$ orbitals, where the crystal field effect is dominant, *e.g.*, previously mentioned in Mn ions. It means that the spin-orbital coupling gives rise to the total angular momentum and lifts the degenerate states for $4f$ orbitals. The crystal field effect therein plays just a role as a perturbation in the description of the electron system. Hence, the transition states in the rare earth are noted by atomic term symbols.

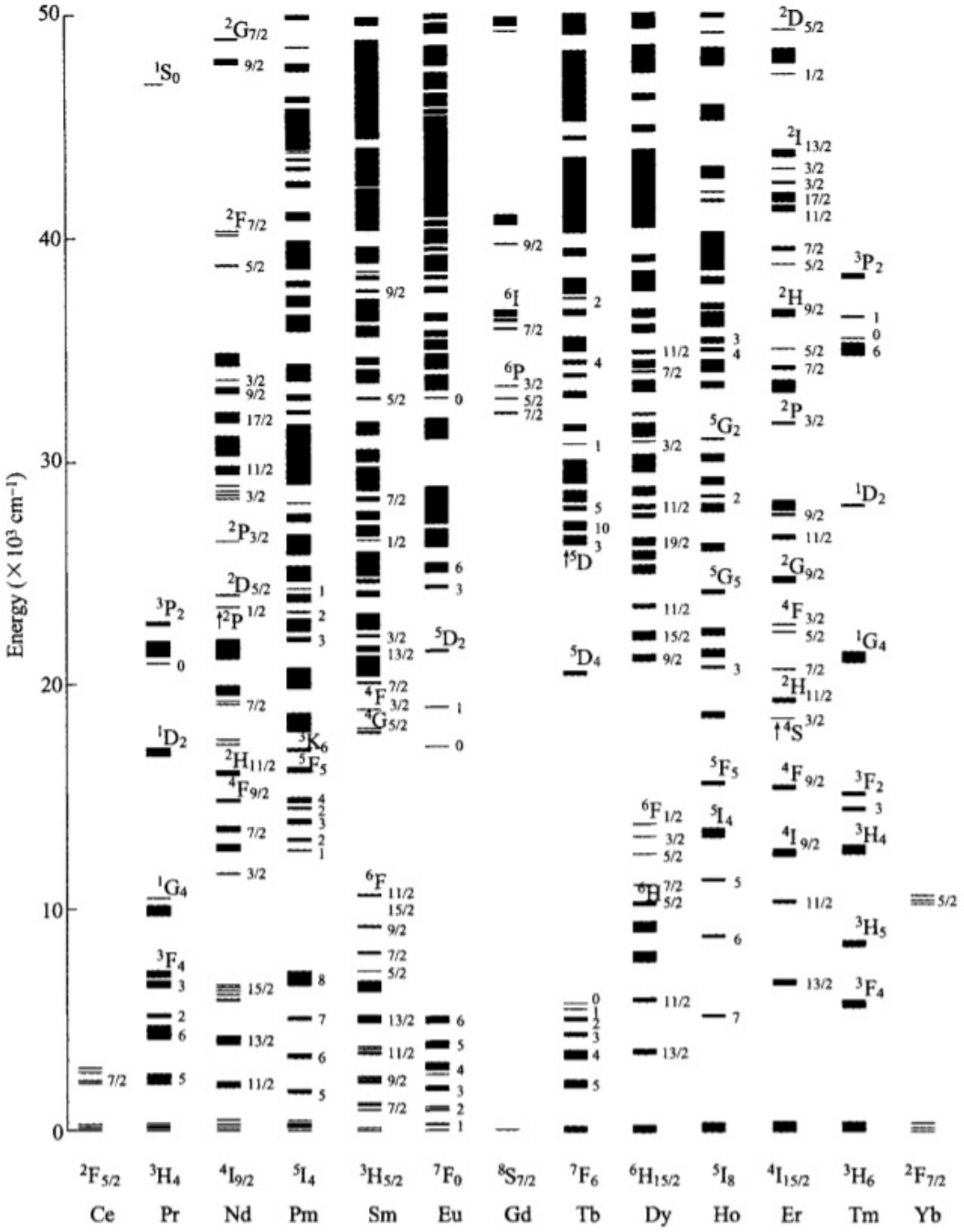

Figure 1.11: Energy level structure of rare earth ions R^{3+} [68].

1.2 Pyrochlore $Lu_2V_2O_7$

Background

The interest for $Lu_2V_2O_7$ arises from the fact that the composition is a ferromagnetic insulator candidate for future spintronic devices. In conducting materials, electrons are the carriers during the spin propagation; the dissipation by Joule heating is unavoidable. However, in a magnetic insulator like in $Lu_2V_2O_7$, spin moments are carried by magnons (quanta of magnetic excitations). Consequently, a fundamental question is arisen for the magnon spin current that is, whether it will exhibit the thermal Hall effect or not.

Recently, a magnon Hall effect has been experimentally observed by Onose [16] in $Lu_2V_2O_7$. Indeed, this phenomenon is an anomalous thermal Hall effect which depends on the magnetization; it appears spontaneously with decreasing temperature. This kind of Hall effect is favored by magnons, where the Dzyaloshinskii-Moriya interaction plays an indispensable role, hence it is called also magnon Hall effect. The observation of magnon excitations is of particular interest. RIXS is a powerful tool to achieve the diagram of magnon dispersion (versus the transferred moments) to confirm the existence of magnons. Unfortunately, the magnon excitations have generally very low energy (on the order of 100 meV), thus the energy of magnon excitations should be at least higher than the overall energy resolution of RIXS (see Chapter 2).

From the theoretical point of view, the anomalous Hall effect can be described in the frame of Berry phases (see Ref. [69]): detailed information can be found in Ref. [70]. The energy of magnon excitations was predicted by Periro [71] at 261 meV, while taking into account the Heisenberg and Dzyaloshinskii-Moriya interactions on the topological phase [which corresponds to the surface orientation (111)].

Pyrochlore $A_2B_2O_7$ is a material with a complex crystal structure. Structurally, the magnetic A ion and sixfold ligands – oxygens – form an octahedron, and the nearest neighbors (NN) establish corner-sharing tetrahedra, where no magnetic B atom is located at the center of the tetrahedra. It involves the kagome and triangle lattice on the crystal orientation (111). From the projected view on this (111) surface, A atoms draw a translated *Star of David* (✡), where the barycenter is occupied by a B atom. In addition to this specific topological phase, pyrochlore compounds have some exotic properties which can be related to the magnetic interaction. Magnetic frustration is a classic question about the orientation of antiferromagnetic moment in 2-dimensional (2D) triangle. If the two magnetic moments of NN are opposite, the moment orientation of the third one becomes unknown, as shown in Fig. 1.12. These three spins are impossible to be all antiparallel. This issue reflects the classical geometric frustration in 2-dimensions (2D). The interest in the behavior of frustration is that the entropy of the system is not equal to zero, even when the decreased temperature reaches the absolute zero. This means that the ground state has lots of degenerate states. Generally, this frustration leads to spin fluctuations in the antiferromagnetic material. The fluctuation of spin could be either classic (large spin, much larger than the minimum S of 1/2) or quantum (quantum of angular momentum is quantized in half-integer unit of $\hbar$) [72].

This geometric frustration can be also present in ferromagnetic materials with orbital ordering, for instance, $Dy_2Ti_2O_7$, $Ho_2Ti_2O_7$ and $Ho_2Sn_2O_7$ [73, 74, 75]. These ferromagnetic compounds have a large spin from $4f$ electrons pointing to the local (111) axis. The spin of $4f$ electrons behaves as Ising doublets, which depend on the crystal field. For these compounds, the orbital ordering of rare earth on the vertex of tetrahedron is directed to the barycenter occupied by the non-magnetic cation. Under the nearest neighbors (NN)

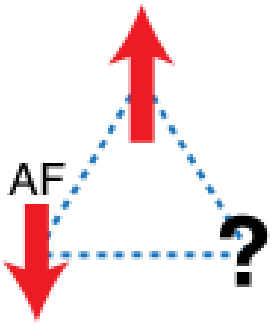

Figure 1.12: Schematic of geometric frustration problem on 2D lattice.

ferromagnetic interaction, the ground state has sixfold degeneracy, if two spins point inward and two spin point outward the tetrahedron (2-in 2-out) center. By analogy, the configuration of spin ice seems like the position of H^+ in the tetrahedrally coordinated O^{2-} framework of H_2O ice. It is the famous *spin-ice rule*. Additionally, in a recent survey of spin structures by polarized neutron scattering, the results obtained on two spin-ice compounds $Dy_2Ti_2O_7$ [73] and $Ho_2Ti_2O_7$ [74] support the presence of magnetic monopoles predicted by Dirac string.

In contrast to the conventional pyrochlore, $Lu_2V_2O_7$ has a different lattice construction, where V atoms are located at the corner-sharing tetrahedra, whereas a Lu atom occupies the center of this tetrahedron. On the surface with (111) crystal orientation, a non-trivial topological phase originates from a kagome texture as shown in Fig. 1.13. It is formed by the triangle and hexagon lattice of the V where the Lu atom, without any magnetic and electric contribution, takes the barycenter of hexagon lattice.

In ferromagnetic $Lu_2V_2O_7$ (with Curie temperature, $T_C = 70$ K), the tetravalent V^{4+} ions possess only one electron on the $3d$ orbital. Despite having simultaneously

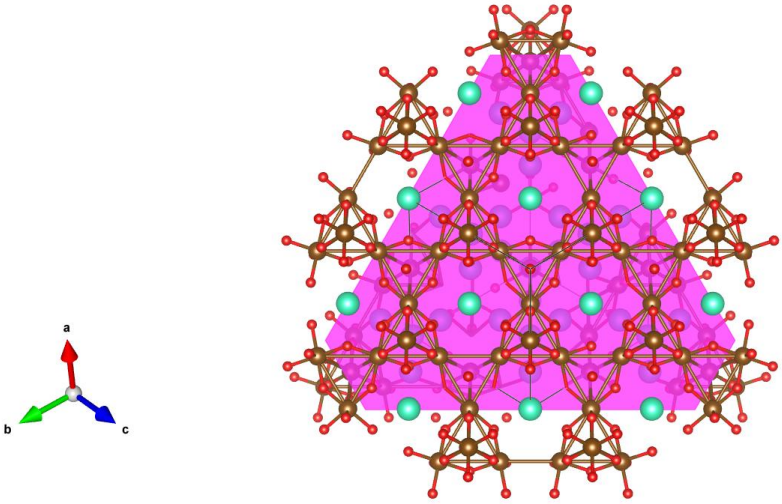

Figure 1.13: $Lu_2V_2O_7$ crystal structure projected in $\langle 111 \rangle$ (shown as the pink plane), where the element of Lu, V, O are represented by the color bull of aqua, coffee and red, respectively.

ferromagnetic and orbital ordering, $Lu_2V_2O_7$ may not be classified as a spin-ice system as previously mentioned for $Dy_2Ti_2O_7$. This is because of its half-integer quantum of the spin angular momentum of V^{4+}.

As mentioned before, a magnon Hall effect has been observed in this material [16]. Magnon Hall effect is actually an anomalous thermal Hall effect enhanced by magnons. Generally, Hall effect is a behavior that creates a voltage difference transverse to an electronic current in the conductor when one applies an external magnetic field perpendicular to the current. Thermal Hall effect is a thermal analog of Hall effect. A temperature gradient arises when applying magnetic field. Here, anomalous signifies that the observation of this effect exists only in the ferromagnetic state. Therefore, anomalous thermal Hall effect (also called magnon Hall effect in $Lu_2V_2O_7$) is an exotic behavior that is directly correlated to the magnetization of the ferromagnetic material. The anomalous Hall effect can be either extrinsic (related to disorder) or intrinsic (linked with the Berry phase in $\vec{k}$-space) [70].

The kagome lattice results in a topological phase. Berry phase [69] which is used to describe the topological character, is a term introduced during the process of finding eigenvalues, where its eigenstate evolves with the time. With the goal to identify the Berry phase, it is useful to understand the various observable physical and chemical properties of topological materials.

For Ising-like rare earth ions in a pyrochlore compound, if the magnetic moments are coupled ferromagnetically, and if each Ising doublet is oriented toward the local (111) axis, the tetrahedron emerges the "2-in 2-out" geometrical frustration based on *ice rules*, *e.g.* $Dy_2Ti_2O_7$ [76]. However, the quantum spin frustrations in $Tb_2Ti_2O_7$ results in a spin-liquid system [77, 78].

Experimental observations demonstrate that the Dzyaloshinskii-Moriya (DM) interaction favors magnon excitations to enhance thermal Hall effect in $Lu_2V_2O_7$ with orbital ordering [18]. This DM interaction, which breaks the inversion symmetry [79], can be described as in Eq. 1.5, where the spin current is proportional to $\left(\vec{S}_i \times \vec{S}_j\right)$. It was shown that the spin dynamic of quantum (Ising doublet S = 1/2) ferromagnet in the pyrochlore $Lu_2V_2O_7$ is not compatible with a classical spin ice system [80].

The initial research goal of this compound was to confirm the existence of magnons by the observation of magnon dispersion. To perform this 2-dimensional (2D) image of intensity versus transferred energy and moment, we expect to obtain the dispersion of magnon by changing the RIXS scattering angle.

Chapter 2

Experimental methods

The main experimental technique used in this thesis is the resonant inelastic X-ray scattering (RIXS) spectroscopy. This element specific "photon-in photon-out" technique allows to simultaneously investigate on-site and inter-site electronic excitations and spin dynamics. In some aspects, RIXS may be considered as similar to Raman scattering, but there are also significant differences. Briefly, the incident photon energy, $h\nu_{in}$, belongs to the X-ray range for RIXS, while light with low frequency (*e.g.*, visible light, infrared, or ultraviolet) is used in Raman scattering. In my thesis, X-ray photons with energy below 1 keV (called soft X-rays) have been used. The overall energy resolution of a scattering technique is related to the frequency of the incident photon. For example, Raman spectroscopy can easily reach a resolution of a few meV for investigating phonon vibration modes in the material, but it does not have element specificity. Although the penetration depth of soft X-rays is weaker than hard X-rays, it can still penetrate a few hundred nanometers into samples in order to carry the bulk information out. The total electron number is conserved during the scattering process, hence RIXS measures neutral excitations. The electronic excitations and decay in the inelastic scattering process produce various excited final states, which means that RIXS is able to record the information originating from both occupied and unoccupied orbitals. During the last decades, RIXS has been developed and has now become a familiar tool to probe the detailed electronic structure in numerous intriguing materials, such as topological materials (*e.g.* frustrated magnets, superconducting materials), multiferroics, and many others.[2]

2.1 Overview of RIXS spectroscopy

RIXS is a fast-developing technique, in which an X-ray photon is scattered inelastically by matter. Before discussing the detailed information of the AERHA (adjustable energy resolution high acceptance) setup, the basic theory of RIXS is introduced in this subsection.

Understanding the process of RIXS is an important step to understand the origin of spectral features present in a RIXS spectrum. RIXS offers the opportunity to observe directly *d*-*d* or *f*-*f* excitations (which are forbidden by direct electric dipole transitions), because the scattering process can be considered, as two steps involving electric dipole transitions: absorption and emission. The cross section of inelastic scattering, through integrating the second order differential cross section, is able to be calculated via the Kramers-Heisenberg formula, but it is generally difficult to calculate it exactly [2, 81].

The Kramers–Heisenberg formula describes the resonant scattering process:

$$\frac{d^2\sigma}{d\Omega_{k'}d\hbar\omega_{k'}} = \frac{\omega'_k}{\omega_k}\sum_{|f\rangle}\left|\sum_{|n\rangle}\frac{\langle f|\,T'^{\dagger}\,|n\rangle\,\langle n|\,T\,|i\rangle}{E_i - E_n - \hbar\omega_k + \mathrm{i}\Gamma_n/2}\right|^2 \cdot\delta\left(E_i - E_f + \hbar\omega_k - \hbar\omega_{k'}\right) \tag{2.1}$$

where E_i, E_n and E_f are the energies of initial $|i\rangle$, intermediate $|n\rangle$ and final $|f\rangle$ states, respectively. σ is the cross-section.

In the absorption process, an atom absorbs a photon with energy $\hbar\omega_k$, which allows the transition from the initial state $|i\rangle$ into an intermediate state $|n\rangle$. This process is driven by an absorption operator T. In the emission process, the transition is driven by an emission operator $T'^{\dagger}$. This operator leads to a decay process from the intermediate state $|n\rangle$ to the final state $|f\rangle$. Therefore, a photon undergoes scattering process and has an energy of $\hbar\omega_{k'}$. During the scattering process, the intermediate state is a virtual state $|n\rangle$. A mixed second derivative of cross section is derived with respect to solid angle $\Omega_{k'}$, and the scattered photon energy $\hbar\omega_{k'}$. The energy conservation is assured during the whole process as defined through the Dirac function $\delta(E_i - E_f + \hbar\omega_k - \hbar\omega'_k)$, where $\hbar\omega_k$ signifies the incident photon energy. The strength of cross section is related to the intrinsic bandwidth from the core-hole lifetime of the intermediate state Γ_n in which the inner-shell core hole usually has a very short lifetime (on the order of fs). Generally, there are two kinds of scattering process (Fig. 2.1): direct RIXS, and indirect RIXS.

In a direct RIXS process, as shown in Fig. 2.1a, the incident photon transfers an electron from an inner-shell into an empty state in the valence band; an electron from a different state in the valence band subsequently fills the created inner-shell core-hole, liberating a photon. In an indirect RIXS process, as shown in Fig. 2.1b, the incident photon also promotes an electron from an inner-shell but into a higher energy state (several eV above the Fermi level); subsequently, this electron decays to the inner-shell core hole. During this process, the inelastic scattering may not be observed if there is no further additional interaction. The energy loss is due to the shake-up excitations created by the inner-shell core hole presented in the intermediate state; this core hole produces a strong electronic potential on the $3d$ valence electrons that gives rise to a core hole screening.

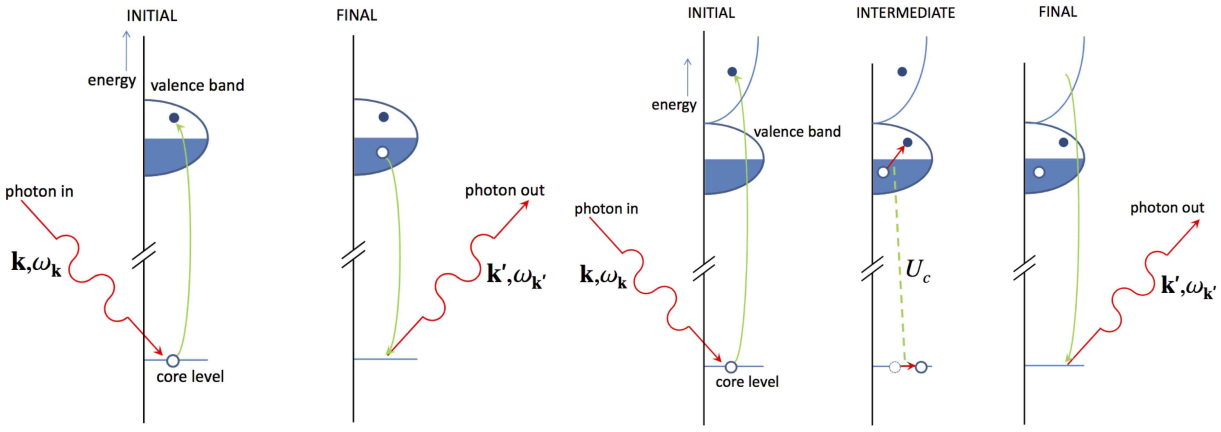

(a) Direct RIXS process (b) Indirect RIXS process

Figure 2.1: RIXS processes [2]. $\mathbf{k}$ is the wave vector of incident photon, and $\mathbf{k}'$ is the wave vector of scattered photon. ω_k and ω'_k is the temporal angular frequency of the incident photon and of the scattered photon, respectively

However, indirect RIXS exists largely at the transition metal K edges ($1s \rightarrow 4p$). At transition metal L edges, the main scattering process is described as direct RIXS.

Orbital d-d and f-f excitations deliver relevant properties of the solid state, such as energy levels splitting due to the crystal field effect ($3d$ orbitals) or spin-orbital coupling ($4f$ orbitals). Note that the crystal field effect plays a crucial role in energy levels splitting especially for $3d$ electrons. The effect of the crystal field ($\sim$ eV) is more important than the spin-orbital coupling ($\sim$ dozen of meV) for the $3d$ electrons. However for $4f$ orbitals, the Hund's rule takes the main weight factor, i.e. the crystal field effect becomes weaker than spin-orbit coupling. Using crystal field multiplet calculations [82, 83] performed for an ion with specific symmetry, one is able to empirically parametrize the effect of ligand-field acting on these electrons. The observation of such spectral features depends on the RIXS energy resolution.

In addition to being able to measure neutral excitations, the RIXS technique has also some main remarkable features amongst which:

- element specificity and orbital selectivity,
- polarization dependence,
- bulk sensitivity,
- energy and momentum dependence.

Element specificity and orbital selectivity

This characteristic behavior appears because each element has its own specific absorption edges. When the energy of X-ray is tuned to the feature of this absorption edge, a sharp increase in absorption appears. This phenomenon is called a resonant effect. Electric dipole transitions respect the following selection rule: the angular part of the wave function of electron must change its parity by $\Delta l = \pm 1$ from the initial state to the final state. The X-ray absorption spectrum (XAS) is acquired by tuning the incident photon energy, illustrates the absorption intensity as a function of incident photon energy. XAS measurement is an important step to probe the electronic structure using RIXS because one needs to select the feature energy in XAS spectrum and check the sample quality via the XAS spectral shape. Note that ions with different formal valence show different XAS spectral shape, in particular they are shifted in incident energy, *e.g.* Cu $L_{2,3}$ XAS of CuO ($2p_{1/2} \rightarrow 3d$ and $2p_{3/2} \rightarrow 3d$) and Cu_2O shown in the Fig. 2.2 [84].

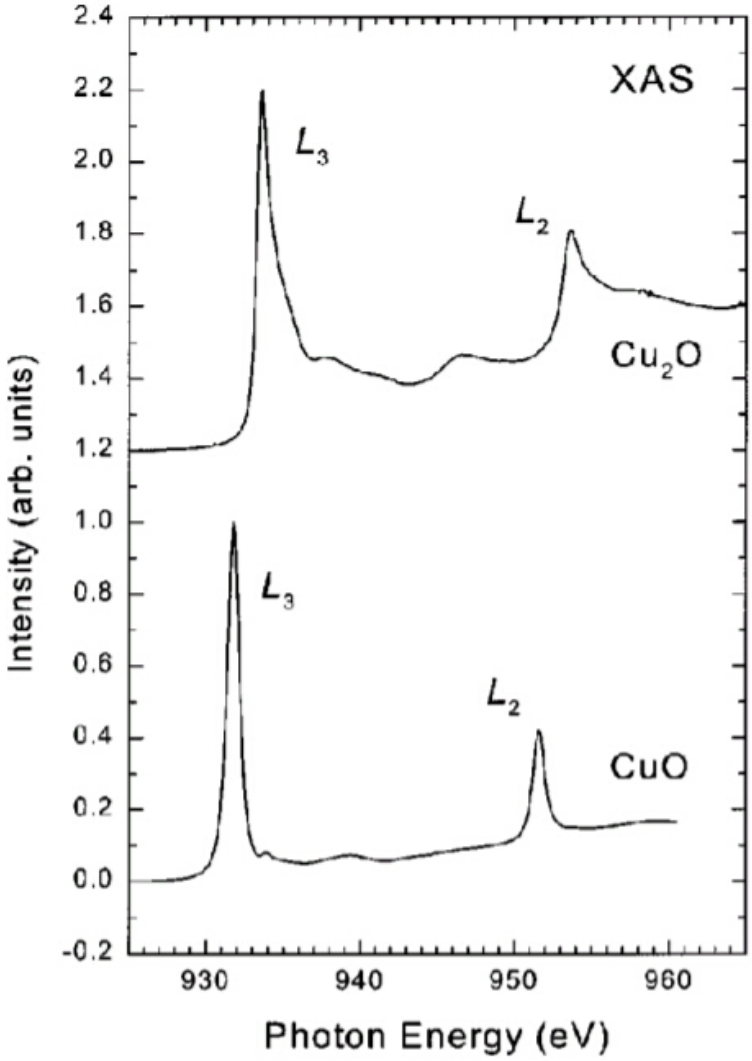

Figure 2.2: Cu $L_{2,3}$ X-ray absorption of CuO and Cu_2O. Both spectra were arbitrarily normalized to the L_3 maximum [84].

Polarization dependence

As the electric dipole transition operator is expressed as $\epsilon\dot{r}$, XAS spectra measured on a non-cubic single crystal show a polarization dependence, that is measured by changing the relative orientation between the sample and the incident polarization of the photon beam. The RIXS spectra of Cu $L_{2,3}$ of $Sr_2CuO_2Cl_2$ shown in Fig. 2.3 were measured at grazing and normal incidence (GI and NI) on the sample [85]. A vertical (V) and horizontal (H) polarization were used in both measurements. The energy shift for the peak of orbital excitation around 1.5 eV clearly shows the polarization dependence.

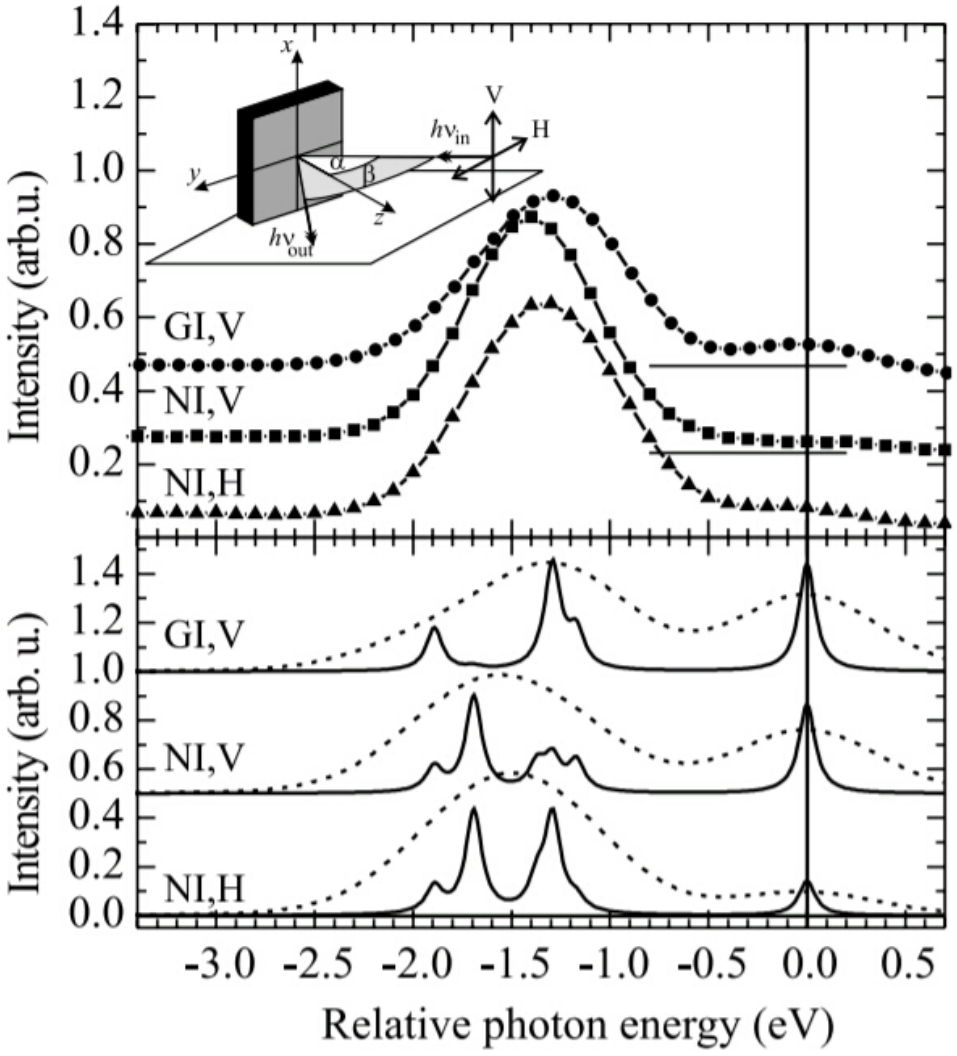

Figure 2.3: Upper panel: RIXS spectra of $Sr_2CuO_2Cl_2$ measured at grazing incident (GI) and normal incident (NI) sample geometry with vertical (V) and horizontal (H) polarizations ([GI,V],[NI,V],[NI,H]). Bottom panel: calculated spectra (solid line) for the same scattering geometries [85].

Bulk sensitivity

Hard X-ray have a large penetration depth, and soft X-ray have a relatively weaker energy. Nonetheless soft X-rays can penetrate a few hundred nanometers into the material at normal incidence. Higher grazing angles reduce to the probing depth, although even at low grazing angles the soft X-rays can still bring out bulk-type information.

Energy and momentum dependence

Since RIXS can take full advantage of the phenomenon that is both the energy and transferred momentum dependence for the cross section of photon scattering, it is able to check the existence of quasi-particle – magnon, viewed as a quantized spin wave (long range magnetic ordering). The transferred momentum $\vec{Q}$ is defined as the variation of the

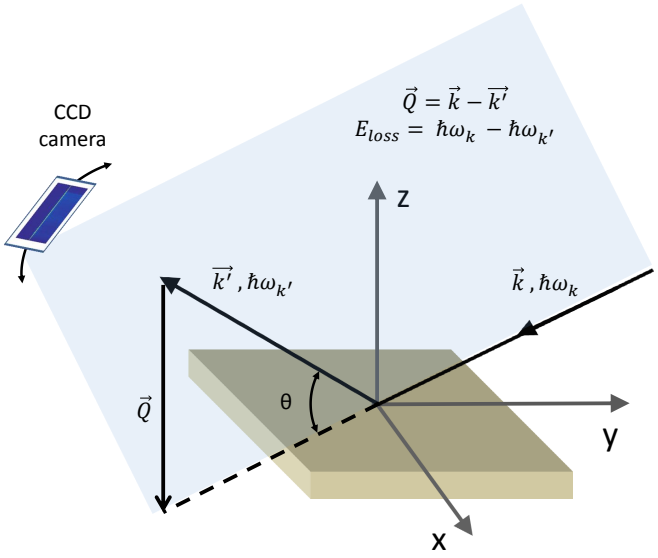

Figure 2.4: Scattering geometry of an inelastic scattering experiment, where the energy loss (relative transferred energy), $E_{loss} = \hbar\omega_k - \hbar\omega_{k'}$, the incident ($\vec{k}$) and scattered ($\vec{k'}$) wave vector form the scattering plan, vector $\vec{Q}$ is the transferred moment.

photon momentum due to the scattering $\vec{Q} = \vec{k} - \vec{k'}$ (shown in the Fig. 2.4). When the sample is fixed, the transferred momentum can be changed by rotating the CCD camera position (scattering geometries) to vary the momentum $\vec{Q}$. A rotatable RIXS detector arm was designed in the AERHA instrument. The method currently used in the AERHA instrument with layered systems is the CCD camera being fixed while one changes the sample orientation. The transferred momentum on the layer is varied by rotating the sample. This map of orbital excitations is obtained by combining the RIXS spectra with same incident energy but with different sample geometry. Fig 2.5 illustrates the map of orbital excitations as a function of transferred momentum and energy loss. Note that the shape of spinon dispersion is totally different from magnon dispersion.

Conclusion

In brief, RIXS is a powerful tool to probe the electronic structure of a specific element. It provides a "neutral" method, where the total number of electrons is conserved in the whole scattering process, to study the interactions among spin, orbital, charge, lattice, by measuring the in-site electronic structure and the pattern of magnon dispersion (correlated to spin dynamics).

The overall energy resolution that can be achieved becomes comparable in neutron scattering if the optical path of beam splitting is large enough. A wide range of excitations are accessible in RIXS as shown in Fig. 2.6, including the excitation of quasi-particle, *d-d* excitations, and charge transfer (CT). The observation of quasi-particles (*e.g.*, magnon, orbiton, polaron, phonon and so forth [87, 88, 89, 86]) while being of increasing interest, still remains a challenge for the experimental physicist because it generally requests that the instrument has a high energy resolving power. Actually, the collective nature of magnons can be confirmed by RIXS via the energy dispersion pattern. Similar energy

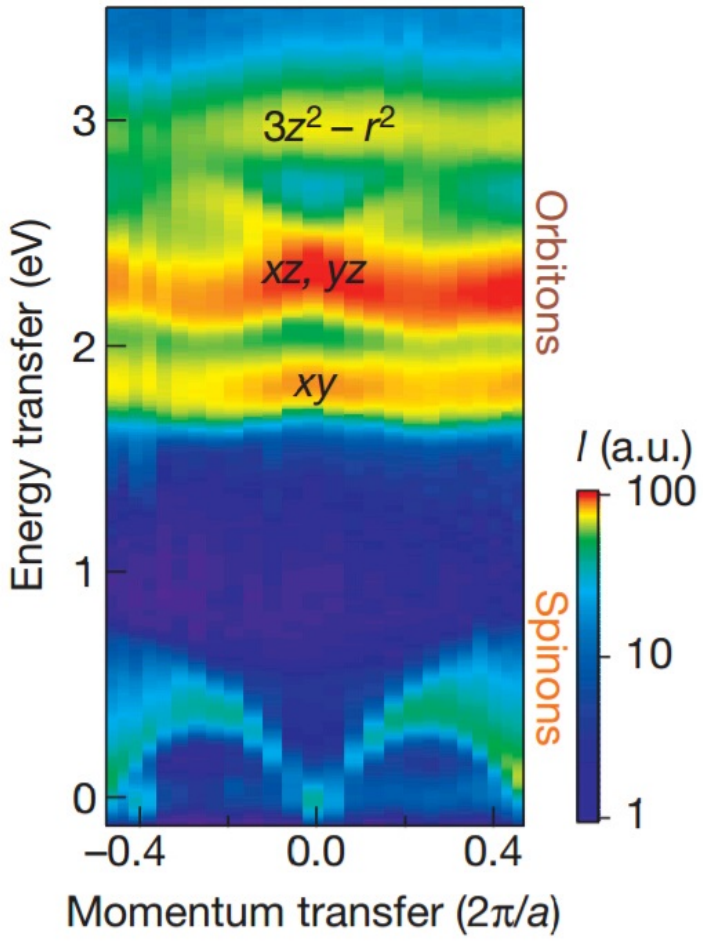

Figure 2.5: RIXS intensity map of dispersing spin and orbital excitations of Cu in Sr_2CuO_3 [86].

dispersion pattern are usually obtained from neutron scattering. Nevertheless, the scanned transferred momentum is continuous in the Brillouin zone in the case [90]. Provided that the RIXS instrument has a high enough energy resolution, RIXS can also probe the phonon excitations which are observed using Raman scattering. In addition RIXS is well adapted to small quantities of matter.

2.2 Experimental aspects of RIXS and presentation of AERHA spectrometer

2.2.1 Synchrotron radiation sources

From the viewpoint of quantum mechanics, the main effect produced by X-rays on an atom is the atom ionization or the excitation of an inner-shell electron that creates a core-hole, generally inducing an Auger decay in the soft X-ray. The scattering radiative process takes only a fairly minor part. In order to have a good statistics during a reasonable

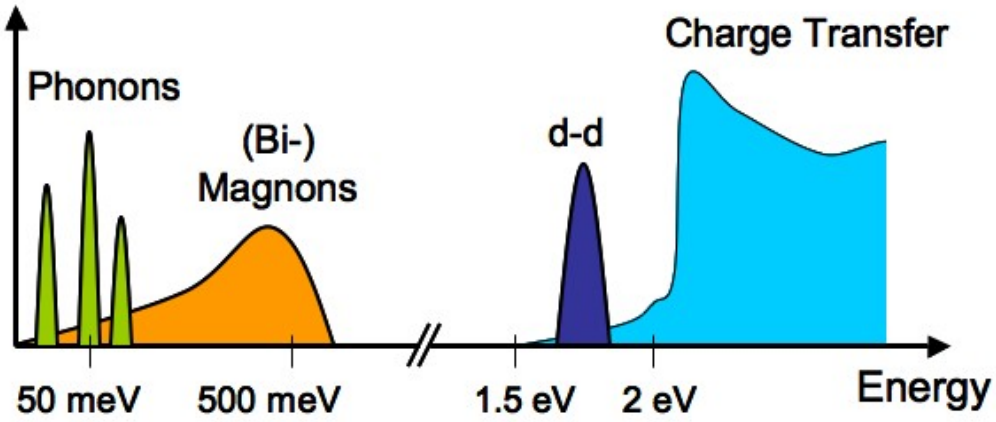

Figure 2.6: Elementary excitations in condensed matter systems that can be measured by RIXS [2].

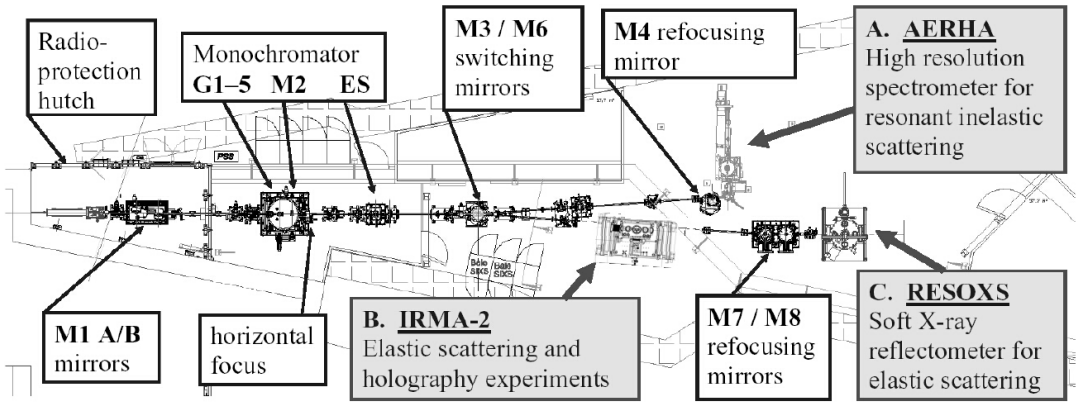

Figure 2.7: Scheme of the SEXTANTS soft X-ray beamline at SOLEIL [3].

measurement time, an X-ray source with high brightness is a prerequisite for using this spatial resolution instrument. As the brightness and stability of beamlines have greatly improved in the third generation of synchrotron sources, the RIXS technique has become gradually a largely utilized tool at these facilities.

In a synchrotron facility, the electron accelerator is a composited electron accelerator, which is constructed by two different devices: a linac and a booster. Electrons are accelerated up to relativistic velocities before being injected as discrete pulses inside the storage ring. The radiation is produced in the storage ring when the traveling electrons change their direction of propagation, upon the influence of bending magnets. When these electrons move across a undulator, they spontaneously deliver large synchrotron radiation. The undulator, which is a series of magnets composed of two parallel magnets having a period alternative change, is designed to laterally oscillate an electron under the applied specific magnetic field and decelerate it. The kinetic energy loss of the electron is equal to the energy of the emitted photon, and the polarization of the emitted photon depends on the relative spatial shift between two parallel magnets.

The generated polychromatic synchrotron beam is delivered to the beamline from the storage ring. For instance, on the SEXTANTS beamline at SOLEIL synchrotron, the

Energy range	$50 - 1700$ eV
Energy resolution	$E/\Delta E > 10^4$ up to 1200 eV
Source	Full range: $50 - 1700$ eV Optimized: $70 - 1500$ eV
Polarization	Circular left/right (CL/CR) Linear horizontal/vertical (LH/LV)
Flux on sample	1×10^{14} Phot./s/0.1%bw @ 100 eV 2×10^{13} Phot./s/0.1%bw @ 1000 eV
Optical element	M1 A/B: plane/spherical mirrors in horizontal deviation Monochromator: 5 VLS plane grating + M2 (spherical mirror) M3/M6 toroidal switching mirrors on hexapod, feeding two branches, one for inelastic (M3), the other for elastic (M6) scattering
Spot on the sample	100×2 μm^2 $(h \times v)$

Table 2.1: Technical information of the SEXTANTS beamline at SOLEIL

photon beam will go through some optical devices as shown in Fig. 2.7. These devices are designed to focus and monochromatize soft X-rays. Some beamlines set a filter for absorbing the low energy by a carbon or an aluminium film, but it does not exist on SEXTANTS beamline. The beam spot is limited by both vertical and horizontal slits. The photon energy is selected by the monochromator by tuning the angle position of mirrors because of the grating diffraction. The elliptical-cylindrical mirror (M4 indicated in Fig. 2.7) is used to focus the photon beam on the sample position, partly determining the spatial resolution of the RIXS experiments. The position of this mirror is controlled by an hexapod. The detailed information on SEXTANTS is listed in Tab. 2.1. The technical characteristics of this beamline are well suited for RIXS measurements.

2.2.2 Description of AERHA spectrometer

The AERHA (adjustable energy resolution high acceptance) instrument [4] is one of the several RIXS spectrometers with highly resolving power. All experimental data shown in my thesis have been measured with this spectrometer. It is permanently installed on the SEXTANTS beamline at SOLEIL. AERHA is especially designed for probing the electronic structure of specific elements, *e.g.* transition metals and rare earths. The adaptable photon energy (which is a trade-off between the energy resolution and photon counts) on this beamline is located in the soft X-ray region, between 50–1000 eV.

The schematic diagram of AERHA spectrometer is illustrated in Fig. 2.8, where the sample position is denoted as "S". A mobile slit is switchable to set closely to the sample. Installing this tiny slit (2.5 μm) aims to gain in energy resolution by limiting the size of emitted photon source. Its optical components involve a collecting mirror (CM), an elliptical mirror (EM), a grating (G) and a charge-coupled device camera (CCD). The mask setup is used to switch the optical path with/without collecting mirror. The CM is

to optimize the number of emitted photons. The EM is designed to get a RIXS spectrum with a high spatial resolution, because the EM possesses two focus points that are located on the position of the sample and of the CCD. The grating (G), which is in fact a VLS (varied line spacing) grating, plays an indispensable role in giving a diffraction angle (depended on the both ingredients - photon energy and incident angle). If the incident angle is fixed, the optical path of the diffracted photon with a certain energy is well defined by the grating equation. In order to acquire a high energy resolution, the optical path should be long enough in the RIXS instrument. For AERHA spectrometer, the distance between the G and CCD is equal to about 2 m.

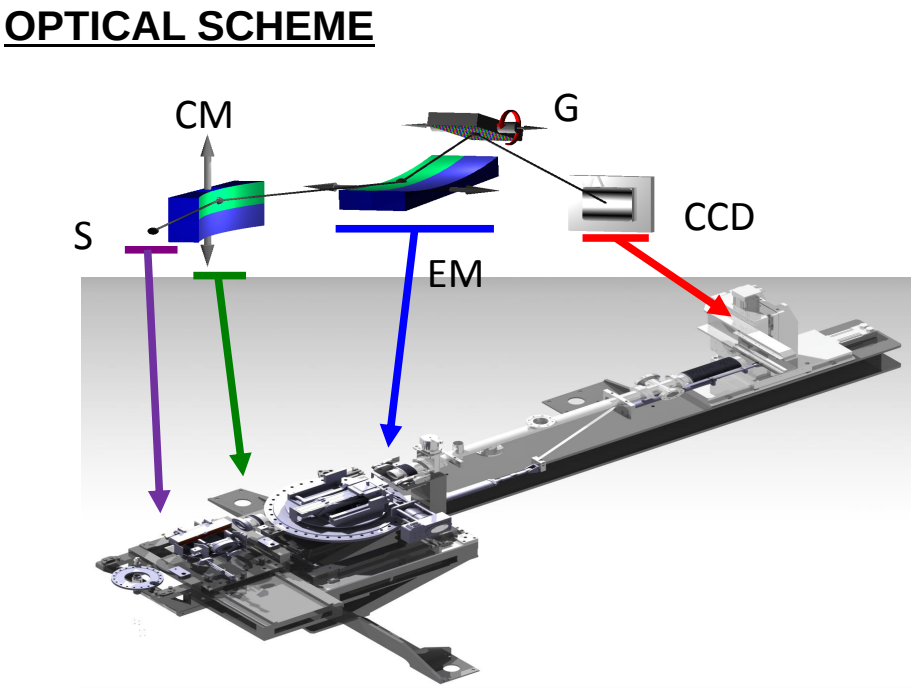

Figure 2.8: Optical scheme of the 3 m AERHA spectrometer, where S corresponds to the sample position, CM is the collecting mirror, EM is the elliptical focusing mirror, G is the varied line spacing grating, CCD is the detector of charge-coupled device camera.

The process of setting up the AERHA spectrometer is presented as following:

1. installation of sample
2. beamline setup
3. RIXS measurement

Sample preparation

A load-lock chamber is designed to allow sample transportation, as well as providing high vacuum conditions to clean the sample. Provided that the sample is not stable in the air, the oxidation will lead to the variation of electronic structure. However, in order to record precisely the electronic structure of the target element in these unstable samples, the sample quality should be guaranteed during measurement. A way to avoid

the influence of impurity due to oxidation on the surface is to polish or cleave the sample under high vacuum condition ($\sim 10^{-7}$ mbar).

For example, the Mott insulator $TbMnO_3$ sample, was glued by two components conductive epoxy from Epo-Tek on copper plate and fixed on the copper holder as shown in Fig. 2.9. The black mark on the copper substrate shows its axis direction $\vec{a}$. The sample orientation was identified by XRD (see support information shown in Fig. 4.1 for detailed information). Since this sample surface is not stable in air, a cleaning process was necessary. When the pressure in the pre-chamber stabilizes at 2×10^{-7} mbar, the surface layer covered with the oxidized part has been scratched by a diamond file until the surface is uniform. The sample is then transferred to the main chamber. Once the sample is detected, a fast XAS spectrum measurement was used to check the sample quality. If the XAS spectrum was abnormal, the sample of $TbMnO_3$ was scratched again.

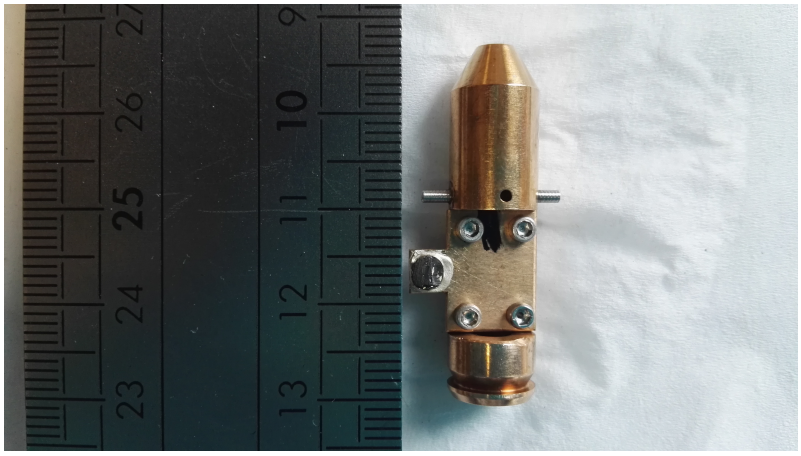

Figure 2.9: $TbMnO_3$ sample (black spot with size of 4×4 mm^2) is fixed on the copper holder. The black line mark on the copper sheet indicates the direction of b-axis sample (confirmed by the Laue X-ray diffraction see support information of $TbMnO_3$ Ch. 4).

Generally, the spot of the incident beam shall be put in the center of the homogeneous zone of the sample. Scanning the sample surface by moving the sample position in the xy plan shown in Fig. 2.10 is a method for identifying the sample quality. If XAS has similar spectral shape in a zone, the photon beam can be sent in the center of this homogeneous zone. The sample holder has four degrees of freedom as shown in the Fig. 2.10, involving the rotation around axis X, and three translation axes in the Cartesian coordinate system.

At normal incident geometry position ($R_z = 90°$), the XAS data can be acquired with different polarization of the incident photon beam, *e.g.*, linear horizontal (LH), linear vertical (LH), circlar left (CL) and circlar right (CR). If a sample displays a polarization dependence, the variation of the XAS spectral shape is evidently observed as shown in Ref. [52]. The polarization mode depends on the undulator settings [3]. For example, Hu44 (Apple-II undulator of 44 mm period) is a specifically designed undulator for the high energy range such as Mn or Ni L edge. This undulator produces merely the light beam with LH or LV polarizations. Hu80 (Apple-II undulator of 80 mm period) is another undulator, but it is specially designed for low energy range such as V L edge and O K edge. This undulator can provide light beams with three different polarizations (LH, CR or CL). The X-ray magnetic circular dichroism (XMCD) [91], a spectrum originated from the difference spectra of XAS spectra measured with CL and CR polarized light under a magnetic field, can be measured in AERHA spectrometer. Note that studies at a controlled

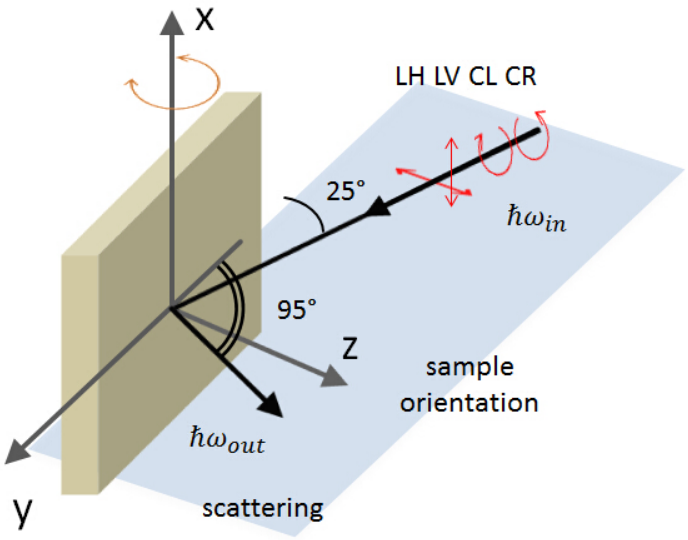

Figure 2.10: Sample geometry with grating angle of 25° during the RIXS measurement of single crystal $TbMnO_3$ (001). The polarization of linear horizontal (LH) mode is in the scattering plan which contains the incident and scattered photon with energy $\hbar\omega_{in}$ and $\hbar\omega_{out}$, respectively.

low temperature can be performed because a continuous-flow cryostat (cooled with liquid helium) is installed in the AERHA spectrometer.

XAS spectra of a conductive material is preferentially measured using the total electron yield (TEY) detection, which measures the current from the ground to the sample when the electron is ionized, thus a good electric conductivity is required in this measurement. Silver paint (especially for the sample that do not need to be polished) or UHV compatible epoxy (generally for samples that need to be polished) are commonly used in sample pasting because of their high electric conductivity. AERHA instrument also includes a multichannel plate (MCP) device. It is designed to measure XAS spectra of gases and insulators.

Description of the beamline

Putting the photon beam in the center of homogeneous zone allows the beam to move by a slight distance. The temperature fluctuation could result in the instability of photon beam position. If the homogeneous zone is large enough, it will not bring a detectable impact on the spectra during a long measurement. Nevertheless, this influence is a detrimental factor when a slit is set behind the sample, because the slit ($\sim 2.5\ \mu m$) blocks the optical path of the emitted photon. The small source size can narrow the full width at half maximum (FWHM) of the elastic peak from 2.55 to 1.91 pixel at zero order, for example at Ni L_3 edge ($\sim$ 850 eV). The overall energy resolution without the slit is 350 meV estimated from the FWHM of elastic peak at 1st order. After the slit is set in, the resolution increases and reaches 180 meV.

Note that RIXS spectra are obtained by integrating across the CCD image matrix (with a size of 2048 pixels $\times$ 2048 pixels). The pixel size of the CCD camera was 13.5 μm/pixel. Provided that the path of photon beam is long enough, two photon paths with small angu-

lar separation can be clearly distinguished (resolved) at the detector. The image acquired directly from CCD represents the spatial distribution of photon beam after diffraction. This integral path for this image matrix should comply with the curvature of bright line (illustrated in Fig. 2.11a) which becomes much more bended and inclined with the increase of included angle. A curvature can be obtained by appropriate numerical treatment in

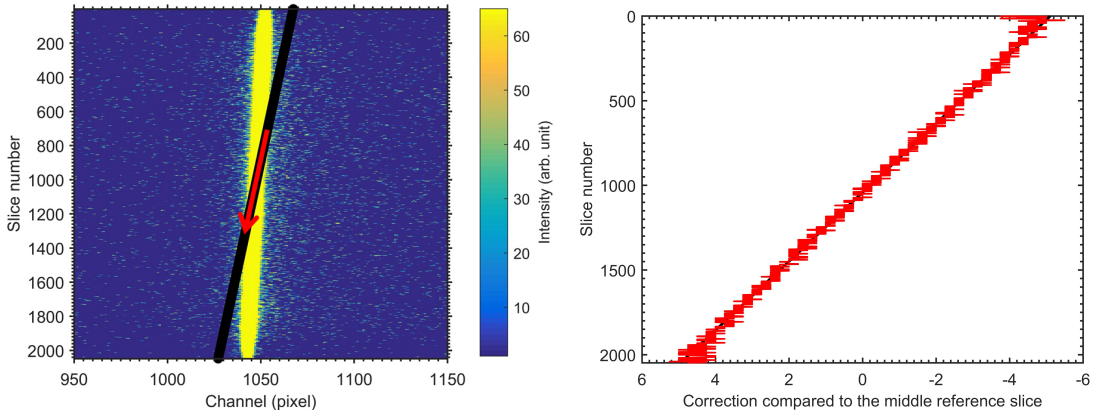

(a) CCD and associated curvature (black line) with integral direction (red line).

(b) Relative shift slice number.

Figure 2.11: CCD image of RIXS and associated integral method.

order to describe the position of the main reflection as a function of slice number at the CCD (shown in Fig. 2.11b). Thus, adding the slices along the curvature, preserves the full width at half maximum (FWHM) of the sum spectra from additional broadening due to image treatment.

The signal intensity and energy dispersion (shift channel number per eV) should be balanced through tuning the grating angle. The grating installed in the AERHA spectrometer is a varied line spacing plan grating (VLS-PG). It leads to the separation of emitted photons with different adjacent angles, depending on the photon energy. The

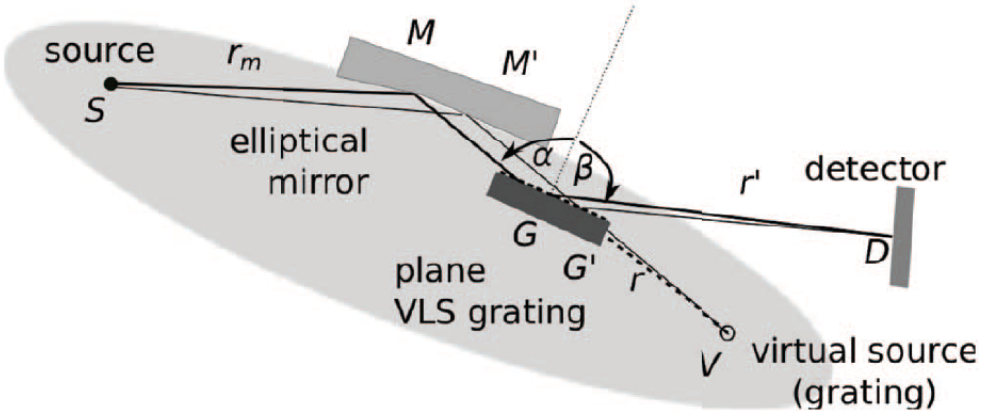

Figure 2.12: Global schematic presentation of the AERHA instrument [4].

grating equation describes this diffraction procedure shown in Fig. 2.12. The included

angle is composed by both incident and diffraction angles:

$$d(sin\alpha + sin\beta) = n\lambda, \tag{2.2}$$

where d is the distance between both lines (1800 lines/mm specially for high energy, $550 - 1000$ eV; 450 lines/mm specially for low energy, $50 - 550$ eV), λ is the wavelength of incident photon, α and β are incident and diffraction angles, respectively. If $n = 0$, the CCD position is in the zero order; If $n = -1$, the CCD position is in the first order, etc. The diffraction angle does not depend on the photon energy ($\lambda = 2\pi\hbar c/E$) when the spatial position is at zero order (means $\alpha + \beta = 0$), the incident photon therein is totally reflected by the VLS-PG. Note that the intensity sharply decreases when CCD position locates at second order ($n = -2$).

The curvature that describes the slope of the bright line (shown in Fig. 2.11a) is related to the included angle ($\alpha - \beta$). It is difficult to make a right decision to compromise between both weight factors – the overall energy resolution of RIXS spectra and the sufficient photon counts in a reasonable measuring time. In order to find out the empirical angle of VLS-PG with the best balance, several settings must be tested.

The grating angle is modulated by applying the electric pulse on a picomotor. During the move of grating angle, one should better follow the intense signal at the zero order by tuning the height of CCD (called CCD_z). Once the grating angle is fixed, the CCD position can be easily detected at zero order. The signal on CCD is set in the center by tuning the CCD_z. The distance between the CCD and EM have to be set at 2 m by tuning the CCD horizontal position (CCD_x). The curvature should be measured again before the focalization. In this regard, the focalization can be finished when the FWHM is minimum by tuning the angle of EM. Fig. 2.13 shows the image and spectrum of RIXS at zero order with the slit after the focalization, where the FWHM of intense peak at zero order can be used to determine the quality of the beamline focus. The FWHM we obtain is usually smaller than 2 pixels.

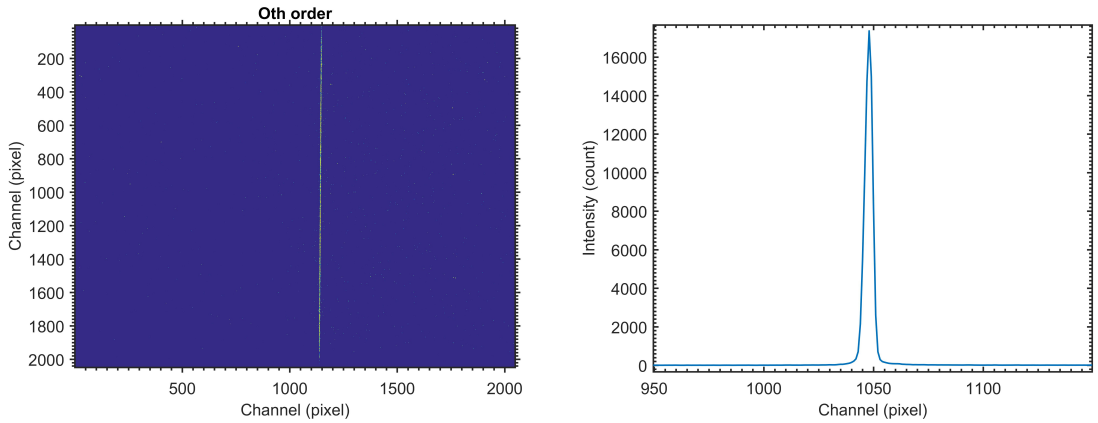

(a) Image 3D (b) 2D plot

Figure 2.13: RIXS data at zero order with slit of 5 µm.

By scanning upward the CCD_z from off zero order, the first order is easily determined. Note that the slit should not be set in the optical path because it cuts off a lot of intensity that will slow the alignment process. Optimization at 1st order is realized by tuning the CCD_x.

RIXS measurements

Alignment for spatial resolution instrument is usually time-consuming in order to obtain the best energy resolution. After this process, optical devices of the spectrometer are requested to be fixed for the RIXS measurement during a long time if the incident photon energy does not need to change widely. Calibration, the last step before the RIXS measurement, is aimed to convert from the channel scale to photon energy. The calibration for RIXS is performed by localizing the channel position of the elastic peak from the measurements with different incident photon energies. The LV polarized photon beams delivers higher intensity due to the reflection with s polarization. The elastic peak of these energies should cover the entire width of the CCD as shown in Fig. 2.14. Since, the intensity of RIXS spectrum is not strong, the RIXS measurement is normally taken with acquisitions of 10 minutes, in order to have a RIXS spectrum with good statistics. With the slit, the measurement of an energy incident at a resonance edge takes about one hour. This RIXS spectrum is obtained from the superimposition of several RIXS spectra, and each superimposition needs to obey autocorrelation for the elastic peak. This dividing operation is just to avoid the FWHM enlargement caused by spatial fluctuations (*e.g.* pump, ground and so on forth) or photon beam drifts.

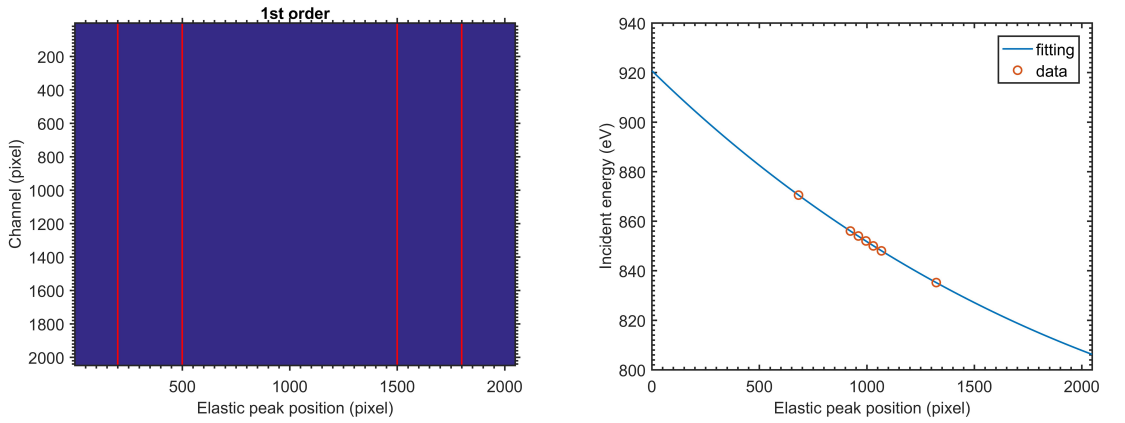

(a) Schematic elastic peak position in calibration (b) Energy calibration as a function of channel

Figure 2.14: Energy calibration for RIXS.

2.3 Commissioning of the collecting mirror

In fact, the CM is currently switchable to be inserted in the AERHA spectrometer (Fig. 2.8). The recent commissioning of the CM setup shows that the intensity is largely increased at 0th order as shown in Fig. 2.15. Based on the theoretical calculation shown in Fig. 2.16, CM is able to collect about two times more emitted photons.

We note that the reflectivity is related to the incident photon energy and matter. The CM is composed of two coatings (Ni and Pt) to minimize the loss of photon at each reflection. Hence, we always use the part with higher reflectance for acquiring the signal as strong as possible. In the AERHA instrument, the EM also has two coatings. In brief, the mirror coating has the energy specificity.

CM is an important optical element for realizing RIXS measurements with a good statistics during a short time. However, when a strong signal is present on CCD, it creates

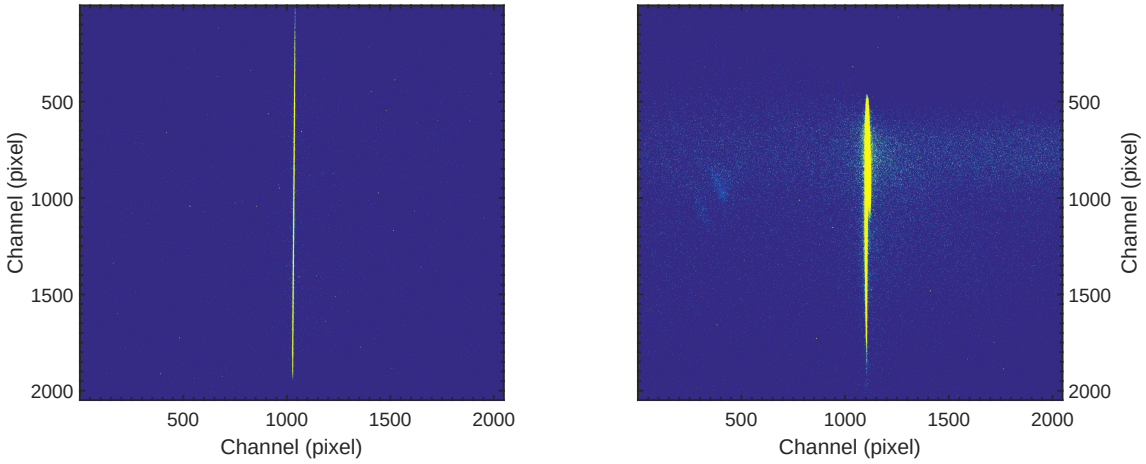

Figure 2.15: (left panel) Intensity of detected photons versus the spatial distribution (pixel × pixel) in the case of no entrance slit and without CM. The total number of photons at the CCD was estimated to be 1.68×10^4, (right panel) intensity of detected photons versus the spatial distribution (pixel × pixel) in the case of no entrance slit and with CM. The total number of photons at the CCD was estimated to be 2.69×10^5.

a residual image with increased background. Note that the last commissioning with the CM setup, the spectral shape of RIXS at Ni L edge of NiO compound is compatible with the published data [93]. The main work during this commissioning is to find out the position of CM. There are four degrees of freedom: pitch, height, yaw, roll as shown in Fig. 2.17. Their movement is carried out by giving a electric pulse on the picomotors.

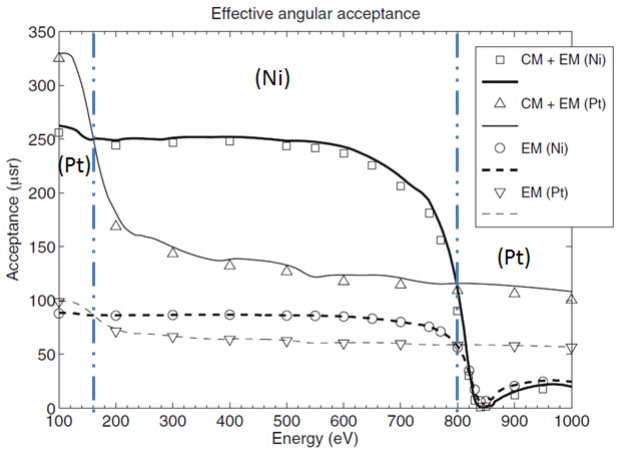

Figure 2.16: Effective angular acceptance of AERHA spectrometer versus incident photon energy [92], where the dot line presents the theoretical calculation of acceptance only with elliptic focalized mirror (EM); the solid line presents the theoretical calculation of acceptance with EM and collective mirror (CM). Both EM and CM contains two coating of Ni and Pt.

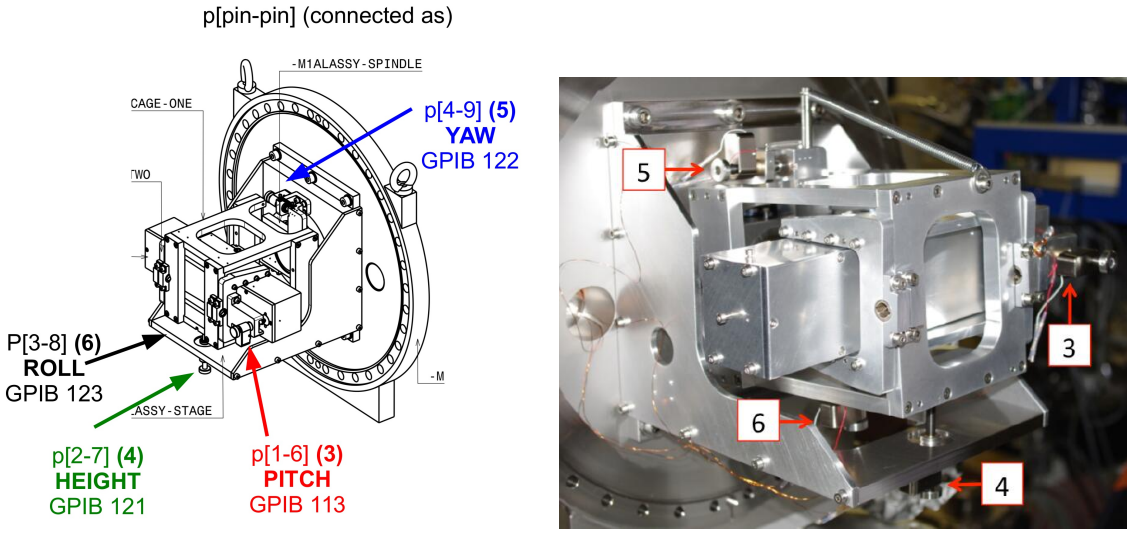

(a) Schematic of frame holding CM

(b) Photo of frame holding CM

Figure 2.17: Frame holding CM, picomotors are indicated by red arrows and numbered as in the Labview controlling program.

Note that the displacement is estimated as:

$$1\ pulse = \frac{d(mm) \times 48350}{1.3},$$

meaning that 50 pulses deliver $50 \times 1.3/48350 = 1.3\ \mu m$ displacement.

- **pitch movement**
  The pitch shifts the beam laterally. It was adjusted using the laser and should not be further modified. It has a relative small impact on the resolution, its position being imposed by the good illumination of the CCD. A precision of 0.1° should be sufficient for the pitch. Accounting for an arm $\sim$ 122 mm it leads to a similar step precision as for the yaw. Thus, the precision for the pitch must be equal or smaller than 5000 pico-pulses.

- **height movement**
  The height can be moved mm-wise for choosing the CM coating. However, its change involves re-adjustment of the roll, as expected from the design.

- **yaw movement**
  The yaw arm averages $\sim$ 130 mm. The precision needed is defined in a first approximation by the illumination of the detector and to a finer degree by the impact of yaw on the resolution. A change of the yaw by 0.2° from the ideal position has an impact on the resolution. A step of 0.1° in the yaw is therefore recommended, giving a distance equivalent to 0.113 mm. This gives that the precision for the yaw must be equal or smaller than 5000 pico-pulses.

- **roll movement**
  A change of the roll from the ideal value of 0.025° starts to have an impact on the resolution, as the FWHM of the image with the detector in 0 order goes from 11 to 16 μm; therefore, we need to target smaller angular precisions like 0.01°. The

roll arm was estimated to be about 78 mm from the drawing meaning that $0.01^\circ = 1.75 \times 10^4$ rad is equivalent to 13.6 μm. In conclusion, the precision for the roll must be equal or smaller than 500 pico-pulses.

2.4 Commissioning of RIXS measurements at the rare-earth $N_{4,5}$ edges

The XAS and RIXS spectra measured at the $N_{4,5}$ ($4d \rightarrow 4f$) resonant threshold of Tb and Dy illustrate the characteristics of the electronic structure. The measurement of XAS was performed at normal incidence. The RIXS spectra have been recorded at the grazing angle of 20°, where the energies of incident photon correspond to the features of absorption. During all measurements, the polarization of photon beam was set as LH mode. The applied incident energy was around 160 eV, the flux on sample was close to 1×10^{14} photon/s/0.1%bw. The overall energy resolution of RIXS spectra achieved from the AERHA spectrometer was 50 meV. All RIXS spectra are normalized by the same acquisition time of 1 hour. (see also section 4.1.2 and 4.2.2)

2.5 Conclusions

Alignment work is the most important part for RIXS, because it determines directly whether the intriguing low energy excitations can be successfully observed. Both factors of AERHA spectrometer, namely the overall energy resolution and the statistics of detectable photons in a reasonable time, need to be balanced. Optimizing the overall energy resolution by modulating the optical path requires much effort and considerable time. Most significant part during all our experiments is to find out this equilibrium point. The excitations at low energy range reveal the interaction among spin, orbit, charge and lattice in the strongly correlated system. Crystal field multiplet calculations, which are presented in the next chapter, will be used to explain the origin of the experimental spectral shapes of XAS and RIXS, providing a means of parameterization the local crystal field effect.

Chapter 3

Crystal field multiplet calculations

3.1 Principle

For strongly correlated systems, the single particle approach meets some difficulties when attempting to calculate accurately the XAS spectrum of an ion. The crystal field multiplet (CFM) approach [13] is able to obtain results, which are in good agreement with experimental results, especially for a localized state. The CFM approach has been implemented for spectra calculations in the TT-MULT code based on the work by Cowan, Butler and Thole [82, 83]. This approach was firstly used to map the absorption spectra at the $L_{2,3}$ ($|2p\rangle \rightarrow |3d\rangle$) edges of transition metals studied by De Groot [94] and at the $M_{4,5}$ ($|3d\rangle \rightarrow |4f\rangle$) threshold of rare-earths studied by Goedkoop [95].

In this chapter, the principles of the CFM approach applied to the calculation of the absorption cross section are introduced, and the calculation steps are also shown in this part. Below I list briefly key features of this theoretical approach:

1. The calculation uses multielectronic wave functions, which means that the cross section calculation is performed for the ion with N electrons. In both the initial and the final states, all electrons of the atom are taken into account for the electronic structure calculation. In the case of electric dipole transitions for the $L_{2,3}$ threshold ($2p \rightarrow 3d$) of Mn^{3+}, the electronic configuration of the initial state $\left|1s^2 2s^2 2p^6 3s^2 3p^6 3d^4\right\rangle$ transfers to the final state $\left|1s^2 2s^2 2p^5 3s^2 3p^6 3d^5\right\rangle$ by electric dipole transitions. Electron-electron repulsions and spin orbit coupling are important, which implies the need for a multi-electronic description. The core-hole potential is also considered during this process.

2. The calculation is performed by considering an ion in a crystal field potential. The crystal field Hamiltonian is parametrized, and the number of parameters depends on the point group symmetry. They are obtained by fitting, from the best match with the experimental spectral shape, or by using values obtained from other spectroscopies (optical absorption, EPR). In addition, the values of spin-orbit coupling (SOC) and Slater integrals (described in terms of Racah parameters B and C) can be reduced from their atomic values. Thus, the CMF approach is semi-empirical.

The absorption cross-section is calculated as:

$$\sigma(\hbar\omega) = 4\pi^2 \alpha \hbar\omega \sum_{i,f} \frac{1}{d_i} \left|\langle f| \hat{O} |i\rangle\right|^2 \delta(E_f - E_i - \hbar\omega). \tag{3.1}$$

The additional term of $\frac{1}{d_i}$ presents the degeneracy of the ground state. In fact, the ground state in the monoelectronic approach is non-degenerate. Conversely, in multielectronic approach, the state is generally degenerate, which must be taken into account. The absorption cross-section is generated from the sum of all discrete transitions from the ground state $|i\rangle$ to the final state $|f\rangle$ by the transition operator $\hat{O}$. The Dirac function ensures the conservation of energy. Commonly, the XAS spectra shape is depicted by convolving discrete states a Lorentzian broadening (accounting for the core hole lifetime) and a Gaussian broadening (accounting for the experimental resolution). At finite temperatures, one calculates the ground state as a combination of different states that are weighted by a Boltzmann distribution.

3.2 Calculation of the states

In order to calculate the multielectronic states, the Schrödinger equation for an ion with N electrons is solved: $H_{ion}\psi_{ion} = E_{ion}\psi_{ion}$. In the absence of an external magnetic field, the Hamiltonian of the ion, H_{ion}, is described as:

$$H_{ion} = T + H_{e-N} + H_{e-e} + H_{SO} + H_{crystal} \tag{3.2}$$

where T is the kinetic energy of the electrons, H_{e-N} is the nucleus-electron attraction, H_{e-e} is the Coulomb repulsions between electrons, H_{SO} is the spin-orbit coupling and $H_{crystal}$ is the crystal field Hamiltonian which describes the potential created by the surrounding ligands on the electrons of the central atom. The initial states are determined from the diagonalization of the matrix formed by the $\langle\psi'|\, \tau_q^{(k)}\, |\psi\rangle$, where $\tau_q^{(k)}$ is k^{th}-rank spherical tensors. This tensor is in fact used to express the Hamiltonian. The final states are determined using a similar procedure, but for the final state configuration. In spherical symmetry (for a free ion) the wave functions $|\psi\rangle$ are written as $|\alpha(L,S)JM_J\rangle$ functions, where J is the total moment combined with L and S ($J = L + S$). The relation among these quantum numbers are $|L - S| \leq J \leq |J + S|$. The total orbital moment of ion, L, and its total spin moment, S, are, via the coupling of N electrons with individual orbitals, l_i, and spin moments, s_i:

$$L = \sum_{i=1}^{N} l_i,$$
$$S = \sum_{i=1}^{N} s_i.$$

For all the shells presented in the electronic configuration, the spin-orbit coupling appears shell by shell [96]. The M quantum number respects $-J \leq M \leq J$. All necessary quantum numbers in order to identify the basis function are described by the α number. Actually, a known atomic configuration determines directly the kinetic energy T and the Coulomb interaction H_{e-N}. These effects just offer a contribution to the average energy of the associated configuration. Under spherical symmetry, the matrix elements $\langle\alpha'(L',S')J'M'_J|\, \tau_q^{(k)}\, |\alpha(L,S)JM_J\rangle$ are inferred as spherical SO_3 group in the irreducible representation notation. The Wigner–Eckart theorem gives the matrix elements relation:

$$\langle\alpha'J'M'|\, \tau_q^{(k)}\, |\alpha JM\rangle = (-1)^{J'-M'} \begin{pmatrix} J' & k & J \\ -M' & q & M \end{pmatrix} \langle\alpha'J'|\, |\tau^{(k)}|\, |\alpha J\rangle\,, \tag{3.3}$$

where $\langle \alpha' J' | \, | \tau^{(k)} | \, | \alpha J \rangle$ is called a reduced matrix element, and $\begin{pmatrix} J' & k & J \\ -M' & q & M \end{pmatrix}$ represents a $3j$ symbol [82]. For the crystal field Hamiltonian (non-spherical symmetry), the rank of the tensor is not zero, $k > 0$. The function $|\alpha j m\rangle$ is adapted to the SO_3 group, but no more appropriated for the eigentstate when the point group symmetry is lower. Fortunately, the subduction theory allows to create a link between the function in the SO_3 and point symmetry group, the explanation of this process is well described in the point group symmetry of Butler [97].

3.3 Calculation process

Generally, there are four steps to calculate the absorption cross section using the CFM approach:

- Step 1: The electronic configuration of the atom in both the initial and final states is chosen, and the code calculates the atomic (free ion) values: the average energy of initial and finial configurations, the direct and exchange Slater integrals, F^k and G^k respectively), and the spin-orbit coupling (ζ_j) in the *.rcg file (see annexes).

- Step 2: Calculation in spherical symmetry of the reduced matrix elements (Eq. 3.3) for the initial state $\langle \alpha'_i J'_i | \, | \tau | \, | \alpha_i J_i \rangle$ and the final states $\left\langle \alpha'_f J'_f \right| \, | \tau | \, | \alpha_f J_f \rangle$ and for dipole transitions from the initial state to the final state.

- Step 3: Calculation of the initial and final states and the transitions in a specific point symmetry group. The output of the calculation is listed in the *.rac_out file.

- Step 4: Convolution of the sticks to generate the absorption spectra. The broadenings are defined in the *.plo file (see annexes).

3.3.1 Atomic calculation

For Mn^{3+} the initial state is written as $2p^6 3d^4$, and the final state is written as $2p^5 3d^5$. The first step in the code is in order to determine the average energy of these states. The most interesting part is the description of electron-electron repulsions. This Coulomb interaction is presented by the matrix elements as the product of the integral over its radial part (numerical part) and its angular part as shown in the following:

$$\begin{aligned} \langle \alpha j m | \, H_{e-e} \, | \alpha' j' m' \rangle = & \sum_{i,j} \sum_{k=0}^{\infty} f_k(l_j, l_j) F^k(l_j, l_j) + f_k(l_i, l_j) F^k(l_i, l_j) \\ & + g_k(l_i, l_j) G^k(l_i, l_j). \end{aligned} \tag{3.4}$$

The (i, j) index denotes the shell of the ionic configuration. l_i and l_j are the quantum numbers of orbitals for each shell. The f_k and g_k functions are related to the orbital moment of the empty or full-filled shell and they have an analytical value [82]. Coulomb interactions, $f_k(l_j, l_j) F^k(l_j, l_j)$, between electrons at the same shell, and $f_k(l_i, l_j) F^k(l_i, l_j)$ between the electrons from different orbitals, are presented in Eq. 3.4. The last term of $g_k(l_i, l_j) G^k(l_i, l_j)$ product signifies the exchange Coulomb interactions of the electrons from different orbitals. An Hartree-Fock model is used to calculate the atomic values of

Slater integrals F^k and G^k. Note that the Slater integrals can be described with the Racah parameters (B and C) of the ion [98].

The matrix element of the spin-orbit coupling Hamiltonian can be described as:

$$\langle \alpha j m | \, H_{SO} \, | \alpha' j' m' \rangle = \sum_{j=1}^{q} \zeta_j d_j, \tag{3.5}$$

where ζ_j is the spin-orbit coupling constant and is a radial integral. The value of angular integral d_j depends on two factors: (i) shell filling and (ii) orbital moment of empty shells.

3.3.2 Reduced matrix elements calculation

In spherical symmetry, the reduced matrix elements $\langle \alpha j | \, | \tau | \, | \alpha' j' \rangle$ are calculated. The reduced matrix elements for H_{e-e} and H_{SO} are 0^{th}-rank spherical tensor $T^{(0)}$ in the SO_3 group. In the Butler notation, this tensor is noted as the completely symmetric representation $\mathbf{0}$ (SO_3) .

The crystal field Hamiltonian is determined by an electrostatic potential where the point symmetry group at the atom site determines how it shall be expressed. The $H_{crystal}$ can be written as a sum of k^{th}-rank spherical tensors:

$$H_{crystal} = \sum_{k=0,even}^{2l} \sum_{q=-k}^{k} \sum_{n}^{j=1} X_j^{kq} U_j^{kq}, \tag{3.6}$$

where, the X_j^{kq} are the crystal field parameters. Only the U_j^{kq} with $k = 0, 2, 4$ are taken into account in the sum.

3.3.3 Initial and final state calculation and calculation of transition intensities

The eigenstates and corresponding eigenvalues of the system for both initial and final state configurations are calculated in the point group symmetry using the subduction theory and the Wigner-Eckart theorem for finite point groups. For example, in an O_h symmetry, H_{e-e} and H_{SO} are described in O_3 as functions of a 0^{th}-rank tensor, which only give a contribution to the average energy of the configuration. The corresponding branch of subduction can be written as $0^+(O_3) \rightarrow 0^+(O_h) \rightarrow 0^+(D_{4h}) \rightarrow 0^+(C_{4h})$. Note that 0^+ is the group representation of the subgroup, where the + sign indicates an even parity. The function of an irreducible tensor $T^{0^+(O_3)0^+(O_h)0^+(D_{4h})0^+(C_{4h})}$ describes that, in O_h symmetry, the Hamiltonians are related to the $\mathbf{0}$ representation in all the groups and subgroups of the subduction. The crystal field acting on $3d$ orbitals of a transition metal ion, leads to parameters which are expressed by the sum of the 4^{th}- and the 2^{nd}-rank spherical tensors ($U^{(4)}$ and $U^{(2)}$, respectively) in SO_3. In fact, only the branches of the irreducible representations $\mathbf{2}^+$ (O_3) and $\mathbf{4}^+$ (O_3) which have the $\mathbf{0}^+$ (O_h) representation must be taken into account for the calculation in O_h symmetry. For the $\mathbf{2}^+$ (O_3) representation the following branching rules are involved Ref. [97] :

$$\begin{aligned}
&2^+(O_3) \rightarrow \tilde{1}^+(O_h) \rightarrow 1^+(D_{4h}) \rightarrow 1^+(C_{4h}) \\
&2^+(O_3) \rightarrow \tilde{1}^+(O_h) \rightarrow 1^+(D_{4h}) \rightarrow -1^+(C_{4h}) \\
&2^+(O_3) \rightarrow \tilde{1}^+(O_h) \rightarrow \tilde{2}^+(D_{4h}) \rightarrow 2^+(C_{4h}) \\
&2^+(O_3) \rightarrow 2^+(O_h) \rightarrow 0^+(D_{4h}) \rightarrow 0^+(C_{4h}) \\
&2^+(O_3) \rightarrow 2^+(O_h) \rightarrow 2^+(D_{4h}) \rightarrow 2^+(C_{4h})
\end{aligned}$$

Since there is no $\mathbf{0}^+(O_h)$ representation in these branches, none of the above branches are not taken into account of in the crystal filed Hamiltonian. For $\mathbf{4}^+(O_h)$, the branches considered are:

$$
\begin{aligned}
&4^+(O_3) \to 0^+(O_h) \to 0^+(D_{4h}) \to 0^+(C_{4h})\\
&4^+(O_3) \to 1^+(O_h) \to \tilde{0}^+(D_{4h}) \to 0^-(C_{4h})\\
&4^+(O_3) \to 1^+(O_h) \to 1^+(D_{4h}) \to 1^+(C_{4h})\\
&4^+(O_3) \to 1^+(O_h) \to 1^+(D_{4h}) \to -1^+(C_{4h})\\
&4^+(O_3) \to \tilde{1}^+(O_h) \to 1^+(D_{4h}) \to 1^+(C_{4h})\\
&4^+(O_3) \to \tilde{1}^+(O_h) \to 1^+(D_{4h}) \to -1^+(C_{4h})\\
&4^+(O_3) \to \tilde{1}^+(O_h) \to \tilde{2}^+(D_{4h}) \to -2^+(C_{4h})\\
&4^+(O_3) \to 2^+(O_h) \to 0^+(D_{4h}) \to 0^+(C_{4h})\\
&4^+(O_3) \to 2^+(O_h) \to 2^+(D_{4h}) \to 2^+(C_{4h})
\end{aligned}
$$

Only one branch that possesses the $0^+(O_h)$ representation is taken into account in the calculation. Hence in O_h symmetry, the $H_{crystal}$ is written as:

$$H_{crystal} = X^{4^+(O_3)0^+(O_h)0^+(D_{4h})0^+(C_{4h})} U^{4^+(O_3)0^+(O_h)0^+(D_{4h})0^+(C_{4h})}. \tag{3.7}$$

The notation of the crystal field parameter is X^{4000}. The link between the X^{4000} parameter and $10Dq$ is written as:

$$X^{4000} = \frac{18}{\sqrt{30}} 10Dq$$

3.3.4 Convolution of spectra

The stem of discrete transitions is calculated from previous steps. A transition is located at the energy $E = E_f - E_i$ and has an intensity of $|\langle f|\hat{O}|i\rangle|^2$. The spectrum is produced by the sum of all results obtained after convolving these stems with Voigt profile. The Voigt profile is a convolution of both Lorentzian and Gaussian function:

$$V(E) = G(E) * L(E) = \int G(\tau) L(E-\tau) d\tau, \tag{3.8}$$

where the Lorentzian $L(E)$ simulates the broadening due to the core-hole lifetime, and the Gaussian $G(E)$ implies the instrumental broadening. They are described as:

$$L(E) = \frac{2\Gamma}{\pi\left[\Gamma^2 + 4(E-E_0)^2\right]}$$

$$G(E) = \frac{1}{\sigma\sqrt{2\pi}} \exp\left[-\frac{(E-E_0)^2}{2\sigma^2}\right]$$

where Γ represents the full-width at half-maximum (FWHM) from the core-hole lifetime; σ is related to the FWHM due to the instrumental broadening.

3.3.5 Consideration in XAS spectra

Fig. 3.1 shows the crystal structure of $TbMnO_3$ (space group Pbnm), which has very similar parameters to $DyMnO_3$. Here, the MnO_6 clusters form a zig-zag chain along the c-axis with a Mn-O1-Mn bond angle of 144.7°. We consider that the symmetry at the Mn site is approximately D_{4h}. The C_4 axis, inclined towards different directions in both cluster types (α-MnO_6, β-MnO_6) are taken into account in the calculation of projection ratio for combining the XAS spectrum. The position of atoms for both clusters and structure parameters are listed in Tab. 1.1 (see chapter 1). The projected ratio (R_{perp} within perpendicular plane and R_{para} within parallel plane) is related to the adjacent angle θ between the polarized unit vector of incident X-ray, $\vec{\epsilon}_{in}$, and the asymmetric axis of C_4, $\vec{u}_{C_4}$. The direction $\vec{u}_{C_4}$ is defined by the position of the O ligands as

$$\vec{u}_{C_4} = \frac{\vec{l}_1 \times \vec{l}_2}{\left|\vec{l}_1\right| \cdot \left|\vec{l}_2\right|}, \tag{3.9}$$

where $\vec{l}_i$ is one of the O-Mn-O vector within the perpendicular plane of rotation axis. For the normal incidence photon beam on the $TbMnO_3$ sample surface, its wave vector, $\vec{k}_{in}$, is parallel with the crystallographic direction (001), then the adjacent angle θ can be calculated by

$$\theta = \arccos(\vec{u}_{C_4} \cdot \vec{\epsilon}_{in}). \tag{3.10}$$

A projected ratio within the perpendicular plane and within the parallel plane are described as

$$\begin{aligned} R_{para} &= \cos^2(\theta), \\ R_{perp} &= 1 - R_{para}. \end{aligned} \tag{3.11}$$

Since the theoretical XAS spectra are aimed to compare with the experimental XAS spectra performed at 20° grazing angle, the $\vec{u}_{C_4}$ needs to be rotated by 20° according to the y-axis indicated in Fig. 4.1. The Matlab code related to this polarization dependence is shown in annexes. Note that all calculations of RIXS maps are performed in the isotropic

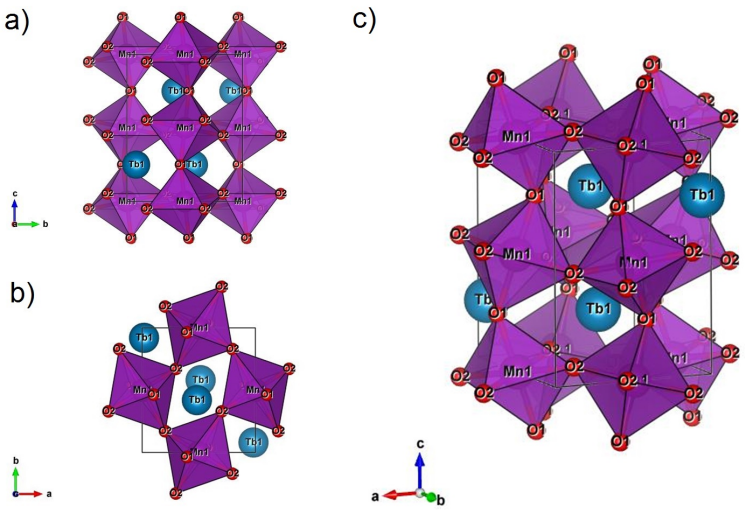

Figure 3.1: $TbMnO_3$ crystal structure within bc plane (a), within ab plane (b) and in global view (c)

case, hence these calculations take into account only the temperature dependence. The Boltzmann equation describes the relation between the weight factor of quasi-ground states (f_B) and the temperature. It can be written as

$$f_B = \exp\left(-\frac{\Delta E}{k_B}\right), \tag{3.12}$$

where the k_B is Boltzmann constant, ΔE is the energy difference between the lowest and higher energy of the ground states. The final matrix of RIXS map, which depends on the incident and emitted photon energy, is summed from the matrix for each state and is taken account with their own weight factor. The RIXS spectrum is depicted by a column vector in the matrix of RIXS map, which depends on the incident and emitted photon energy.

Chapter 4

Experimental results

In this chapter, the experimental data and interpretation for the samples are presented for the samples described in chapter 1.

$RMnO_3$ (R = Tb, Dy)

As previous described, the magnetic manganese ions in $RMnO_3$ (R = Tb, Dy) harbor intriguing physical properties, *e.g.*, specific orbital and special magnetic ordering. The investigation of the electronic structure of Mn^{3+} (with electronic configuration $|3d^4\rangle$) as well as the parametrization of the associated crystal field is useful to describe the microscopic mechanism of ferroelectricity. This is probably helpful in order to figure out a way for increasing the magnitude of presented ferroelectricity and the temperature of phase transition in these materials. In this section, the XAS and RIXS survey in the Mn $L_{2,3}$ threshold for $TbMnO_3$ and $DyMnO_3$ are shown. The oxygen ligands are equally studied at the O K edge.

The very similar crystal structure between $TbMnO_3$ and $DyMnO_3$ gives rise to analogous chemical and physical properties in both archetypes of type II multiferroics; the electric polarization spontaneously appears when the magnetic order becomes cycloid upon cooling. Nevertheless, a few weak differences still present between them. These phenomena might be related to the rare earths. The role of rare earths in the series of multiferroics $RMnO_3$ (R = rare earth) is not yet well understand so far. To study the role of the rare earth, we performed high-resolution XAS and RIXS measurements at the $N_{4,5}$ thresholds. The combined energy resolution of the RIXS spectra taken with the AERHA spectrometer was $\Delta E \approx 50$ meV.

At beginning of this section, both experimental and theoretical results of Mn in $TbMnO_3$ and $DyMnO_3$ are shown as article manuscripts. The results on rare earth from these two compounds are equally shown and discussed.

Support information

Based on the Laue X-ray diffraction pattern (shown in Fig. 4.1), the crystallographic direction of the sample surface was determined as the (001) direction (D_{2h}, space group Pbnm, No. 62, $a = 5.303$Å, $b = 5.830$Å, $c = 7.414$Å).

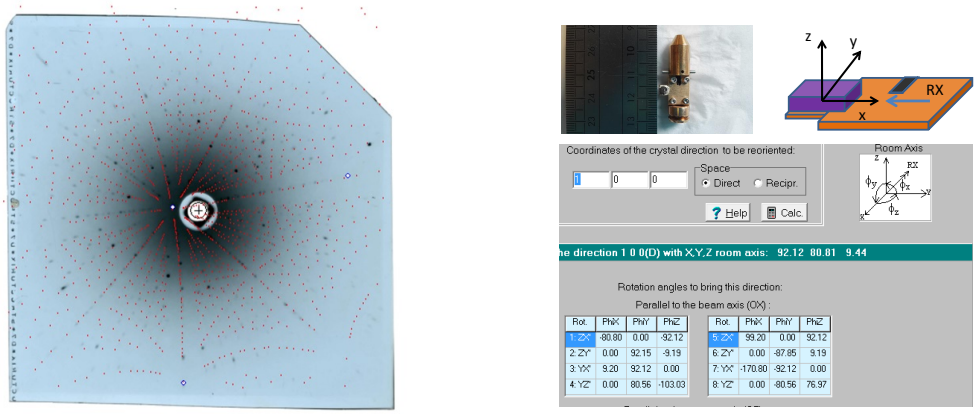

Figure 4.1: $TbMnO_3$ crystal orientation defined by Laue X-ray diffraction. The table shown in the left panel present the different rotation path from incident photon direction to the surface orientation (001), where the reference of rotation axis (ϕ_x, ϕ_y, ϕ_z) are also illustrated.

4.1 $TbMnO_3$

4.1.1 Article: Crystal-field excitations in multiferroic $TbMnO_3$ by Mn L_3 and O K resonant inelastic X-ray scattering

The results on $TbMnO_3$ were published in the Journal of Applied Physics (see Publication 1). As a member of the LCP–MR team, I played the main role during the beamtimes performed at Synchrotron SOLEIL in order to collect the Mn $L_{3,2}$ and O K data presented in the publication. More precisely I was in charge and actively participated in tasks like sample mounting and manipulation, instrument adjustment for high resolution, elaboration of the data collection strategy and in the effective data recording. I was responsible for the continuity of the measurements by restoring the optimal conditions following several thermal or software instabilities. I managed the calibration and the processing of the experimental data, which entered in the figures presented in Publication 1. I have performed the multiplet calculations shown in the paper and explored various working frames (high/low symmetries, photo-reduction, mixed-valences, charge transfer) which led to a reliable final result. In this context it is worth to mention that the final (Dq, Ds, Dt) set was obtained after a careful exploration of hundreds of combinations. The insight provided by the computational part and the broad insight in the specific literature allowed me to effectively participate in the discussion of the results and to actively shape the content of the paper.

4.1.2 Investigation of XAS and RIXS Tb $N_{4,5}$ threshold in $TbMnO_3$

Fig. 4.2 shows the XAS and RIXS spectra of Tb at $N_{4,5}$ resonant edge in the $TbMnO_3$ compound at room temperature. When the incident energy is at the pre-edge of Tb, no sign of inelastic scattering is observed. While increasing the energy, some features of f-f type excitations appear clearly at low energy range, below 1 eV and above 3 eV. Meanwhile, the intensity of these Raman-like excitations below 1 eV increase gradually.

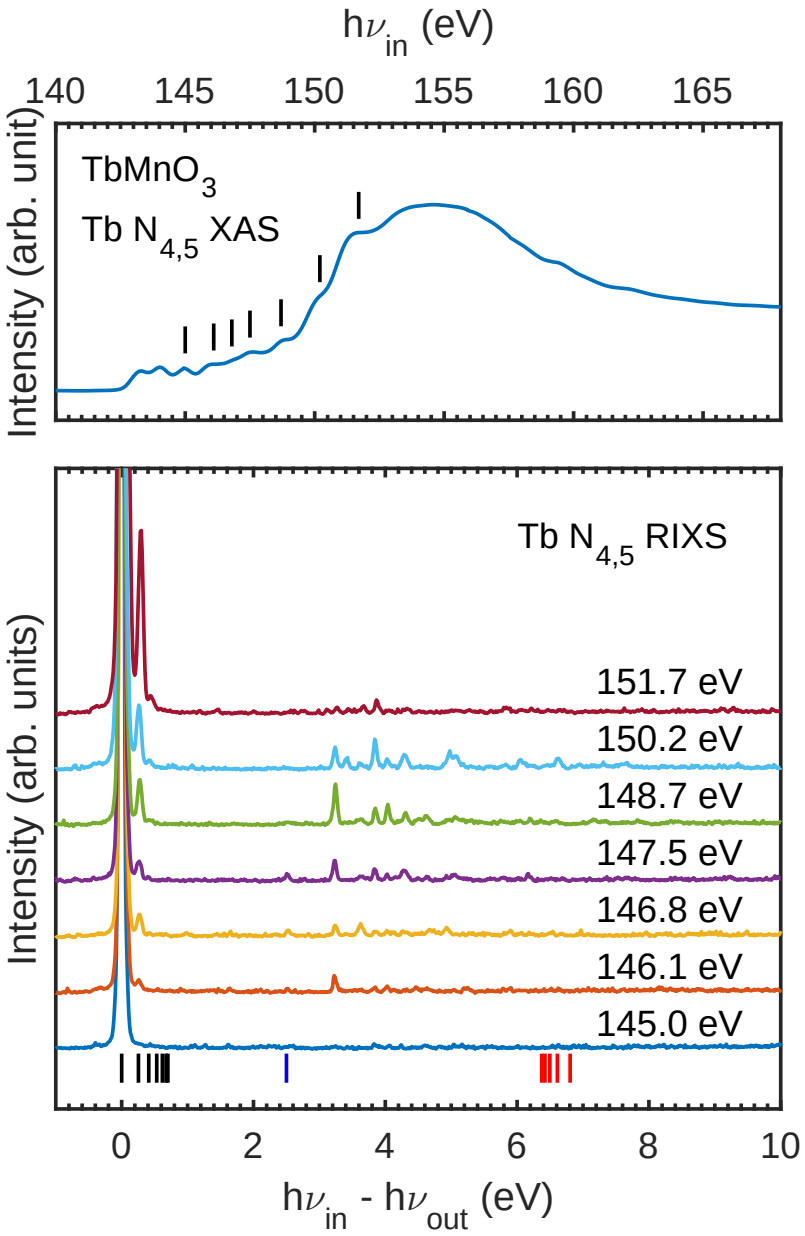

Figure 4.2: RIXS spectra at the Tb $N_{4,5}$ edge for $TbMnO_3$ recorded at the room temperature. The black bars in Tb $N_{4,5}$ edge XAS spectrum indicate the incident photon energies applied in the RIXS measurements. The RIXS spectra therein are presented as a function of energy loss, $h\nu_{in} - h\nu_{out}$, where, referred from the NIST database [99], the vertical black and red line are corresponding to the eigenstate ^7F and ^9D, respectively. The blue line is a Raman excitation not reproduced by calculation in Ref. [100].

The intensity of these Raman-like excitations above 3 eV present a more complex energy dependence. These excitations become clearer and clearer at the beginning of the photon energy increase, but they almost disappear when the incident photon energy is over 150.2 eV. The Raman excitations of Tb^{3+} in $TbMnO_3$, on the energy loss ($h\nu_{in} - h\nu_{out}$) axis, are similar to the observation of Tb^{3+} in the oxide compound Tb_4O_7 [101]; the Raman excitations hidden in the asymmetric elastic peak in the previous observation, are relatively well separated in our experimental measurement.

In the case of Tb, in the experiment, the feature of a Raman excitation is observed at the energy loss of 2.5 eV. This excitation was not found from atomic calculations in Ref. [101]. The Raman excitation (below 1 eV) beside the peak of elastic scattering is corresponding to the energy levels splitting of ^7F_J. These degeneracy states can be identified by using the NIST database [99]. The remaining Raman excitations are identified by the quantum calculation for the electronic configuration of $|4f^8\rangle$ [101].

In order to identify all Raman excitations, the measured electronic energy level structure with high energy resolution needs to match theoretical calculations. The crystal field effect therein could subtly change the eigenvalue of states. Almost all Raman excitations in $4f$ orbital reflect the atomic characteristics. Few identified or shifted features in RIXS spectra should be due to the presence of the weak crystal field effect. Note that the crystal field multiplet calculation is a reliable approach to build the theoretical XAS and RIXS spectra. Using this approach, our current work is focused on finding the crystal field parameters (involving the Slater integral and probably taking into account the crystal field).

The theoretical studies are carried out in the first approximation (neglecting the crystal field effect in the site of rare earth), where the atomic characteristic are fully determined by the calculated spectra. In this framework, the calculation of Lanthanide has been systematically studied through mapping the XAS spectra at the $N_{4,5}$ resonant edge of trivalent rare earth [102]. These theoretical results are in a good agreement with experiments. The measured RIXS spectra of rare earth are equally analyzed via a reliable calculation based on the Cowan-Butler-Thole code [82, 83].

Recently, we simulated the XAS and RIXS spectra, where the theoretical results are compatible with the experimental observations, via calculations [103, 104, 105] in an atomic framework. The atomic parameters used in the calculation are listed in Table 4.1. The

Atomic parameters	
F^2_{ff}	0.7379×14.911
F^4_{ff}	0.8384×9.3571
F^6_{ff}	0.8324×6.7321
ζ_{4f}	0.9561×0.2212

Table 4.1: Energetic values of the electronic structure parameters used in the calculations for Tb^{3+}, and all energies are in eV.

theoretical and experimental XAS spectra illustrated in Fig. 4.3a, demonstrate that the main observed features of absorption can be relatively well reproduced by the theoretical calculation. Nevertheless, calculating the cross section of absorption for each transition state remains a challenge.

The appearance of Raman excitations below 2 eV are due to the spin-orbital coupling induced energy level splitting. The ground state of Tb^{3+} is $^7F_6$. The two Raman excitations, which are close to the feature of elastic scattering, correspond to the $^7F_5$ and $^7F_4$ states. The excitation on energy loss scale at 2.5 eV appears in our calculation, unlike the calculation in the Ref. [101]. The calculated Raman excitations above 2 eV reveals a slight energy shift compared to the experimental result. This phenomenon is probably due to the weak crystal field effect in $4f$ orbital.

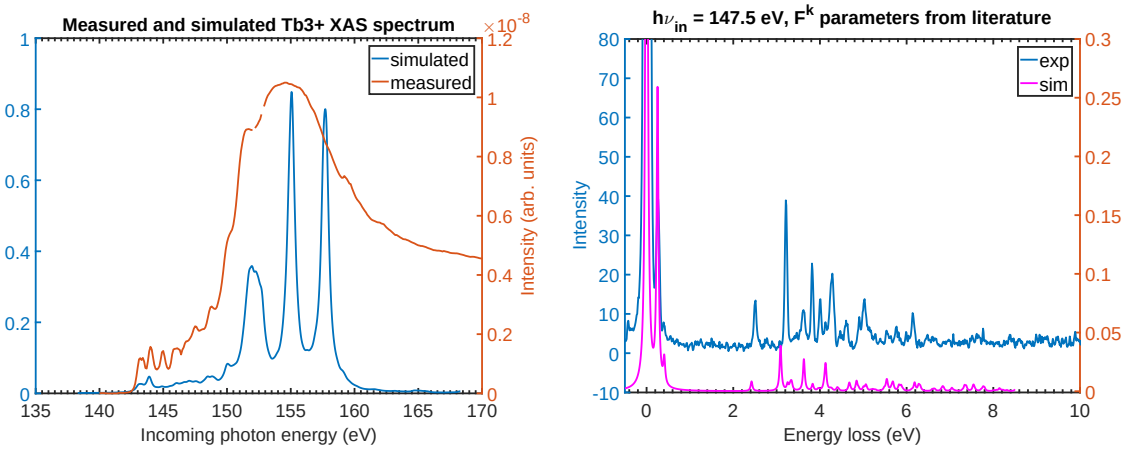

(a) XAS spectra

(b) RIXS spectra

Figure 4.3: Experimental and theoretical results at Tb $N_{4,5}$ threshold for single crystal $TbMnO_3$, where the intensity of XAS spectra versus incoming photon energy, hv_{in}; the intensity of RIXS spectra versus energy loss, $hv_{in} - hv_{out}$.

4.2 $DyMnO_3$

4.2.1 Article: Electronic structure of $DyMnO_3$ probed by resonant inelastic X-ray scattering at the Mn L_3 and O K edges

The experimental and theoretical results on $DyMnO_3$, are listed in a manuscript which will be submitted to J. Phys.: Condens. Matter, see Publication 2.

For this article, I made a similar contribution as for the $TbMnO_3$ studies, including experimental work, data analysis, and crystal field multiplet calculations. Furthermore, I realized high-quality figures to be used in the article.

4.2.2 Investigation of XAS and RIXS at the Dy $N_{4,5}$ threshold in $DyMnO_3$

Similar investigation was performed to study Dy in the $DyMnO_3$ compound. The XAS and RIXS spectra of Dy at the $N_{4,5}$ resonant edge is shown in Fig. 4.4. In the case of the $4f$ orbital of the rare earth, the Raman excitations arise gradually while increasing the photon energy, $h\nu_{in}$. The spin-orbit coupling induced energy level splitting is illustrated in the RIXS spectra. The intensity of these Raman excitations increases while increasing the photon energy. When $h\nu_{in}$ is set at the pre-edge of $N_{4,5}$, in RIXS spectrum, the signal comes merely from the elastic scattering. When $h\nu_{in}$ is above 153.4 eV, the Raman excitations above 2.4 eV appear and depend weakly on $h\nu_{in}$. The illustrated XAS and RIXS spectra of Dy in $DyMnO_3$ have a spectral shape which is highly similar with the one of the Dy in Dy_2O_3 [100].

In the case of Dy, the spin-orbit coupling gives rise to the Raman excitations (below 1 eV), which correspond to the lifted degeneracy state of ${}^6H_J$. The ground state of electronic configuration $|4f^9\rangle$ is ${}^6H_{15/2}$. We note that an excitation was listed in the the NIST database [99] at 1.0 eV energy loss but was not found in the experiment. The eigenvalue of this transition state is probably shifted. This behavior is probably due to the presence of crystal field effect in the Dy site. Note that the calculation [100] predicts that an f-f excitation arises at 2.5 eV, which is not in agreement with experimental measurement.

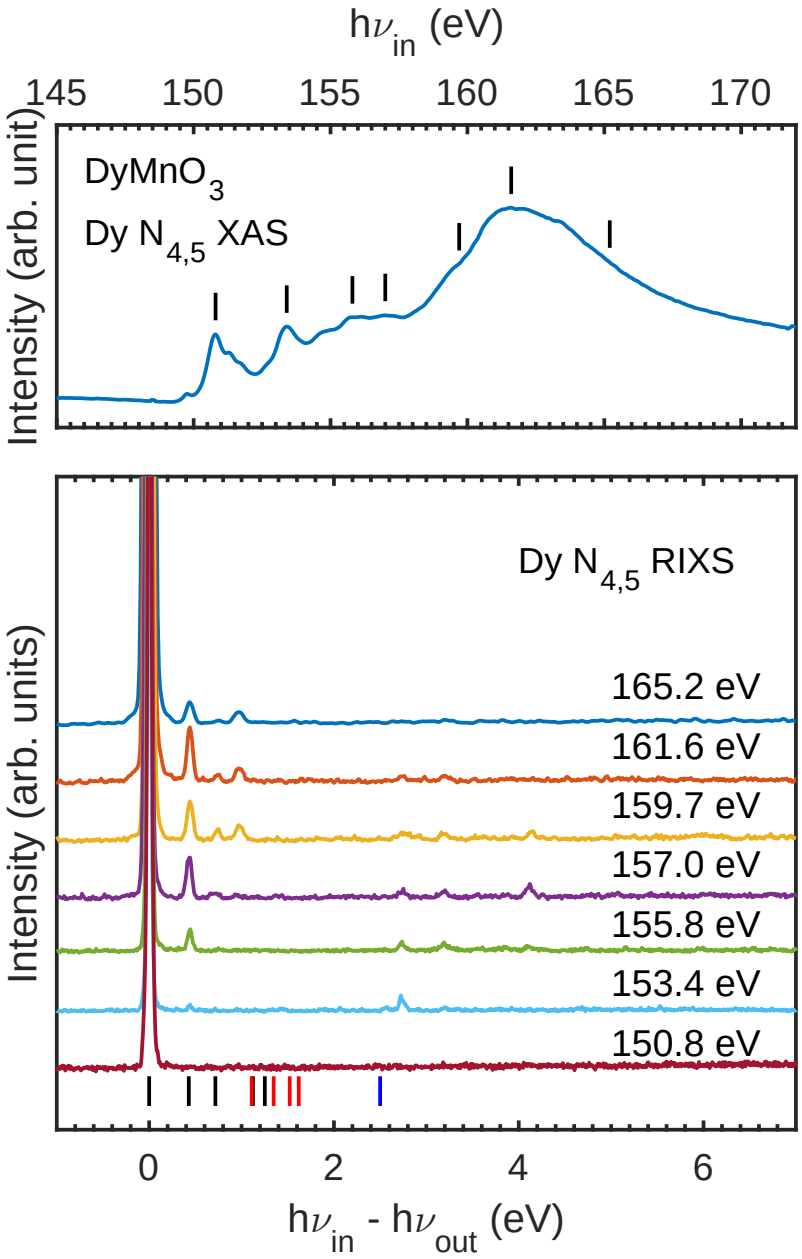

Figure 4.4: RIXS spectra at the Dy $N_{4,5}$ edge for $DyMnO_3$ recorded at room temperature. The black bars in the Dy $N_{4,5}$ edge XAS spectrum indicate the incident photon energies applied in the RIXS measurements. The RIXS spectra therein are presented as a function of energy loss, $h\nu_{in} - h\nu_{out}$, as referred from the NIST database [99], the vertical black and red line is corresponding to the eigenstate ^6H and ^6F, respectively. The blue line is a Raman excitation which was not resolved in Ref.[101].

4.3 $Lu_2V_2O_7$

By using resonant inelastic X-ray scattering (RIXS), the on-/inter-site electronic excitations in single crystal $Lu_2V_2O_7$ were probed at V L_3 ($2p$–$3d$) and O K ($1s$–$2p$) edges with an overall energy resolution of 140 meV. Similar peak position of extensive orbital excitations in both V L_3 and O K RIXS data indicate a high $2p3d$ orbital hybridization. We show below that mixed valence states can explain d-d excitation at 2.7 eV. XAS and RIXS simulations using quantitative weight factors for V^{3+}, V^{4+} and V^{5+} states, are shown to be consistent with experimental observations. We also note that the origin goal of magnon measurements was reconsidered as the predicted energies were later recalculated to average 26 meV [17].

4.3.1 Experimental method

Pyrochlore $Lu_2V_2O_7$ single crystalline with orientation (111) [106] was provided by Dr. ZHOU Haidong from National High Magnetic Field Laboratory at Tallahassee of USA. The sample was polished using diamond filer at 10^{-7} mbar in pre-chamber. All measurements were performed under ultra-high vacuum system (10^{-9} mbar) on adjustable energy resolution-high acceptance spectrometer (AERHA) [4] at the SEXTANTS beamline [3] (high photon flux on the sample with a spot of 100×2 μm^2, SOLEIL synchrotron, France). The XAS spectra (sampled with 10 points eV^{-1}) of room temperature was measured by total electron yield (TEY) method at both grazing and normal incident with linear horizontal (LH) and linear vertical (LV) polarization. RIXS spectra of room temperature and 25 K (cooling by liquid helium) were performed using LH polarization (resolution $E/\Delta E \sim 10^4$ for an exit slit opening of 10 μm). The incident photon energies were determined according to featured peaks of the atomic multiplet eigenvalues as well as the pre-edge. The overall resolution was estimated to be $\sim$ 140 meV from the FWHM of the elastic scattering measured at the V L_3 edge ($\sim$ 515 eV), and the resolution of O K edge ($\sim$ 530 eV).

4.3.2 Result and discussion

The rare-earth element Lu^{3+} with full shell $4f$ in this compound does not have any contribution neither for electronic nor for magnetic system. The total energy of the electron system for formal valence V^{4+} (with electronic configuration $3d^1$) corresponds to the splitted orbital energy levels under the crystal field effect. In the solid, the spin-orbit coupling is relatively weaker than crystal field effect for $3d$ orbital due to the orbital quenching. However, spin and orbital (the internal degrees of freedom) survive in the Mott insulator [35]. Therefore, only crystal field generated from the lattice plays a crucial role in this intriguing case.

The crystal field is described as two parts: one is octahedral VO_6 cluster with O_h symmetry; another one is a systematic distortion of O_h octahedra produced a trigonal crystal field to the vanadium ions [107]. It is important to note that crystal field effect from VO_6 occupies the leading position, which splits fivefold degeneracy $3d$ orbitals into a doublet e_g and a triplet t_{2g}. The crystal field effect from the tetrahedra is weaker than the octahedra. One can consider this crystal field to have a trigonal distortion, with point symmetry group of D_{3d} at V site [19]. This secondary effect replaces the triplet t_{2g} into e'_g and ground state a_{1g} with a splitting energy $\Delta_1 = 0.4$ eV and rises slightly the highest-energy state e_g; thus there is a splitting energy $\Delta_2 = 2$ eV between the e_g and a_{1g}.

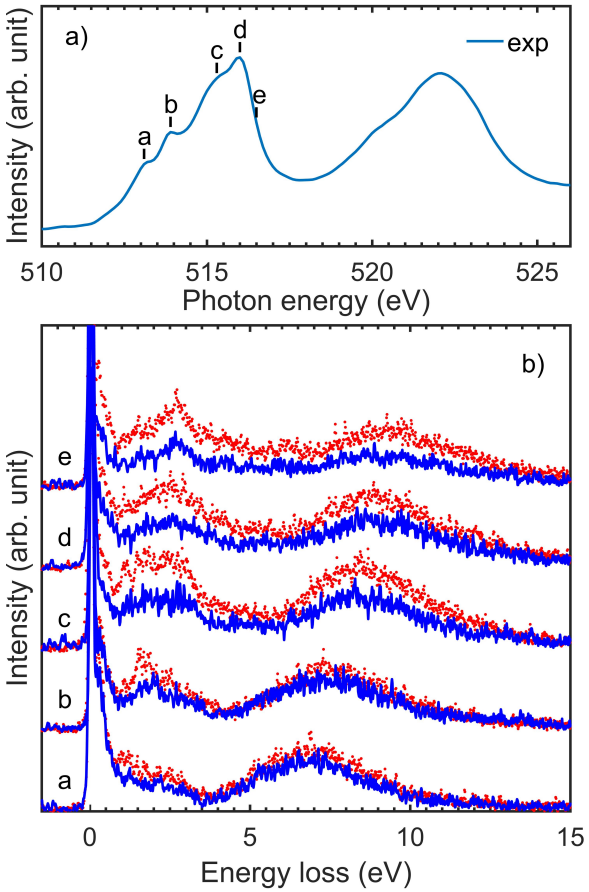

Figure 4.5: XAS of V at $L_{2,3}$ edge in the single crystal $Lu_2V_2O_7$ are shown in top panel, where the letters indicate the applied incident photon energy to gather the RIXS spectra at room temperature (red dot) and 25 K (blue line) shown in bottom panel.

In an alternative model, the ground state of electron system is written a linear combination of wave function from the t_{2g} states [18]. The crystal field in this case is related to the previous crystal field model [19]. By taking into account of the electron hopping process, it successfully describes the magnetic form factors which is consistent with neutron scattering diffraction measurement [18].

X-ray absorption spectrum (XAS) at V $L_{2,3}$ edge of $Lu_2V_2O_7$ is illustrated in the Fig. 4.5a, where the features at L_3 edge are enumerated by the letters. Resonant inelastic X-ray scattering (RIXS) data are gathered by using the incident photon energy corresponding to the energy position of featured peak on XAS spectrum. The RIXS spectra at room temperature and 25 K, illustrated in Fig. 4.5b, are normalized by the same time acquisition of one hour. These RIXS spectra show the intensity versus the energy loss, $\Delta E = h\nu_{in} - h\nu_{out}$, at different incident photon energies, $h\nu_{in}$. At low $h\nu_{in}$, the RIXS spectra at 25 K emerges with a similar spectral shape as the one at room temperature, but a subtle difference appears around 1 eV. As $h\nu_{in}$ is increased, RIXS spectra at both temperature have the same variation tendency, but for room temperature, the spectra show some relatively robust orbital excitations. In these RIXS spectra, the *d-d* excitations with constant energy loss do not appear as the narrow peaks like the theoretically discrete

states when we have a high energy resolution; instead they own a rather continuous spectral shape. However, the peaks of *d*-*d* excitation can be still identified at 0.4 eV, 1.8 eV and 2.7 eV in energy loss by Gaussian fitting. The exotic Raman excitation at 2.7 eV is not compatible with theoretical calculation for $|V^{4+}\rangle$ initial state.

The V-V dimerzation in VO_2 which has been theoretically and experimentally proved [108, 109], brings out the similar RIXS spectral shape due to the presence of the $|3d^2\rangle$ from the hopping process [110]. The large nearest neighbor (NN) distance ($r_{V-V} = 0.35$ nm) between the V position in $Lu_2V_2O_7$ rules out the formation of direct covalent-like V-V bonds. The size of this cubic lattice ($a = 0.994$ nm) [111] is modulated slightly (maximum 2 pm) by decreasing the temperature [112]. In addition, the decreasing temperature leads resistivity to rise up exponentially [113].

For $3d$ transition metal oxides, XAS spectrum can reveal the sign of charge fluctuation ($d_i^n d_j^n \leftrightarrow d_i^{n+1} d_i^{n-1}$) when the $2p3d$ hybridation is strong, in Mott-Hubbard insulators [114]. Additionally, core-hole propagation in the RIXS process can be ignored, since that the lifetime of intermediate state is short relative to the time for electron propagation [115]. Using the CTM4XAS and CTM4RIXS [116, 117] softwares for the crystal field multiplet calculation [118], one can simulate, via empirically parameterizing the crystal field, the experimental XAS and RIXS spectra of single valence ions with certain symmetry. The charge transfer effect was not taken into account in these calculations, because of the charge transfer effect only influenced the intensity of *d*-*d* excitations in RIXS spectra. The XAS and RIXS spectra calculations were performed for the single valence ions V^{3+}, V^{4+} and V^{5+} with D_{3d} symmetry. Theoretical spectra for mixed valence were obtained through a linear combination (see Fig. 4.6).

The parameters for describing the crystal field at V site were set to $10Dq = 1.5$ eV, $D\tau = D_\sigma = 0.05$ eV for D_{3d} symmetry, and Slater integrals are scaled down to 80% of their Hartree-Fock values. Note that calculated XAS spectra of V $L_{2,3}$ with D_{3d} symmetry are similar to the ones of O_h symmetry shown in the reference [20] when the distortion parameters are relatively weak. However, the obvious difference of XAS spectral shape for V^{5+} is due to the presence of strong ligand-to-metal charge transfer effect; the origin of this effect can be explained from chemical point of view, that is V^{5+} possessing an important electronic affinity attracts the electron clouds close to V nucleus [119].

The crystal field parameters used in the calculation of V L edge RIXS spectra are identical to the parameters used in XAS calculations. The effect of the temperature was included in the calculations. Firstly, the theoretical V L edge RIXS spectra are calculated only for the single valence of V^{4+} with electronic configuration $|3d^1\rangle$, depicting three clearly discrete features peaks (see Fig. 4.7): elastic peak locates at the origin of energy loss axis, inelastic peaks are at the transferred energies ΔE of 0.4 and 1.8 eV. This energy level splitting is compatible with the two different mentioned models, meaning the crystal field parameters are reasonable. A better agreement between experimental and theoretical results (see Fig. 4.8) is found in the case that, when V^{3+} and V^{5+} were considered with equal weight factor. The electronic configuration of V^{5+} is d^0-ness, hence the RIXS process cannot theoretically give any contribution to the feature peak of energy loss but it gives rise merely to elastic feature. The inelastic feature of $\Delta E = 2.7$ eV emerges if and only if the ground state of $|3d^2\rangle$ is taken into account. This indicates that a ground state $|3d^2\rangle$ is an indispensable ingredient of this *d*-*d* excitation. Thirdly, weight factors of $V^{3+} : V^{4+} : V^{5+} = 1 : 2 : 1$ are used in the crystal field multiplet calculations, illustrating the best compromise case between experimental observation and theoretical calculation for both XAS and RIXS spectra shown in Fig. 4.9. Summing up the RIXS results with V^{3+} , V^{4+}

and V^{5+}, taking into account a specific weight factor, is a successful means to draw the similarly continuous RIXS spectral shape, explicating the energy of *d*-*d* excitations.

Therefore, the RIXS spectra obtained from the experiment is due to presence of the ground state of $|3d^2\rangle$. This state might originate from either the charge fluctuation or dimerization. However the dimerization is hard to be formed in pyrochlore due to its less compacted crystal structure than VO_2. The specific weight factor points to that the origin of this manifestation is probable to be due to the presence of itinerant electrons in the system.

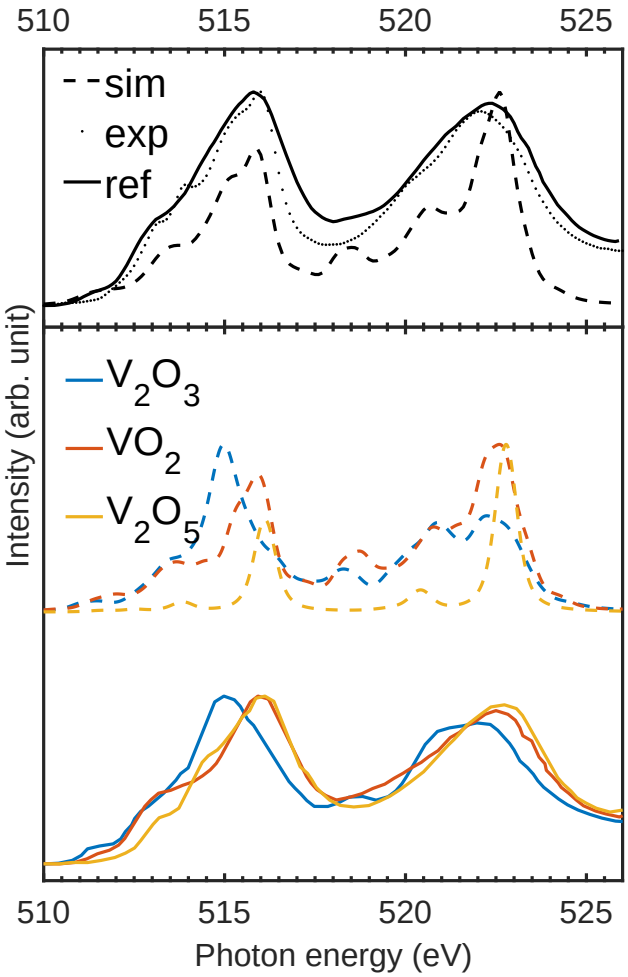

Figure 4.6: (bottom) Reference V $L_{2,3}$ XAS spectra (solid lines) for V_2O_3, VO_2 and V_2O_5 (from Ref. [20]) compared to single valence calculation. (top) measured V $L_{2,3}$ XAS spectra (dot line) of $Lu_2V_2O_7$ compared with a linear combination of measured (solid line) and calculated (dashed line) spectra (see bottom panel).

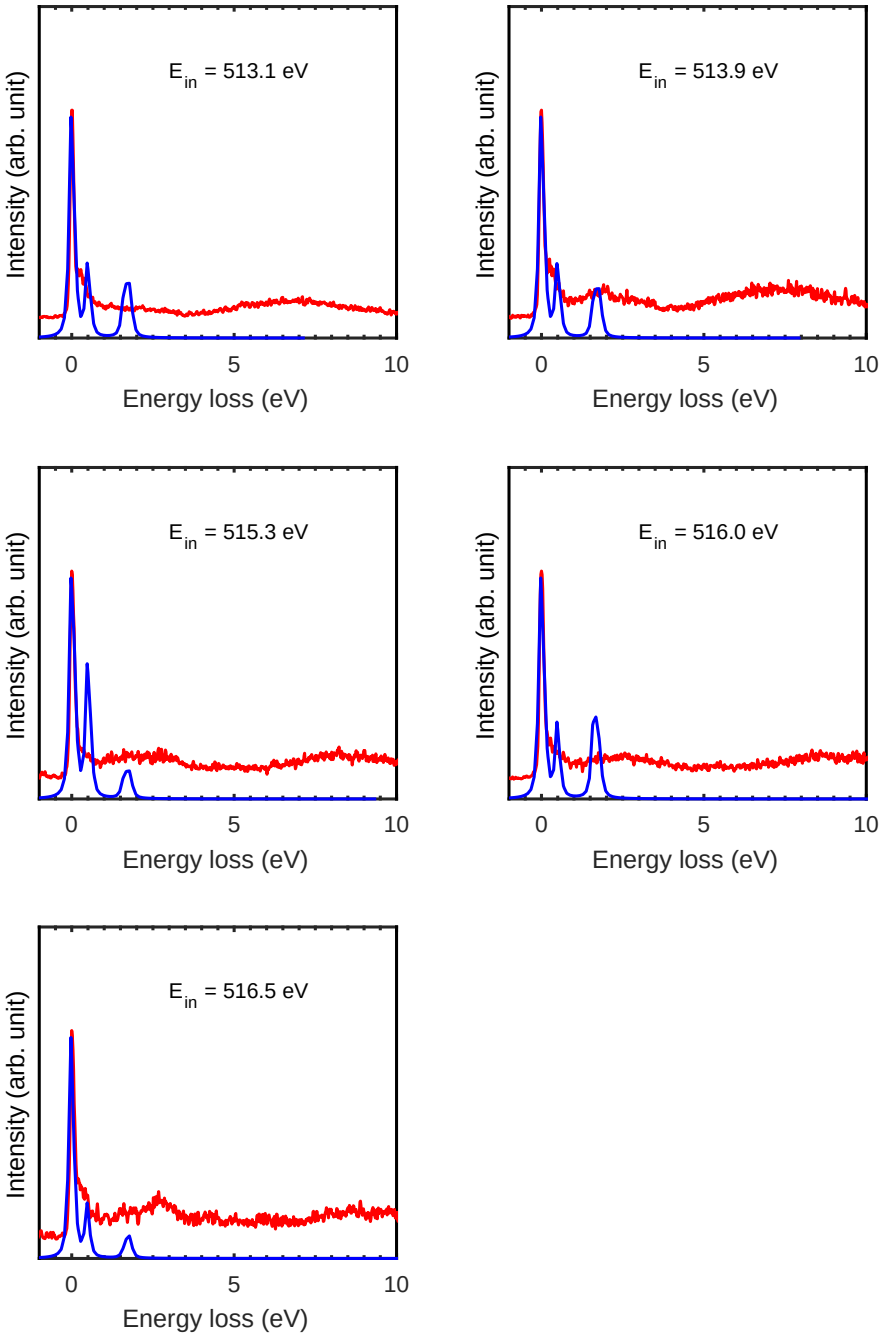

Figure 4.7: Experimental (blue line) and theoretical (red line) spectra of V L edge RIXS in $Lu_2V_2O_7$ at 25 K calculated with the weighting factors V^{3+}:V^{4+}:V^{5+} = 0:1:0.

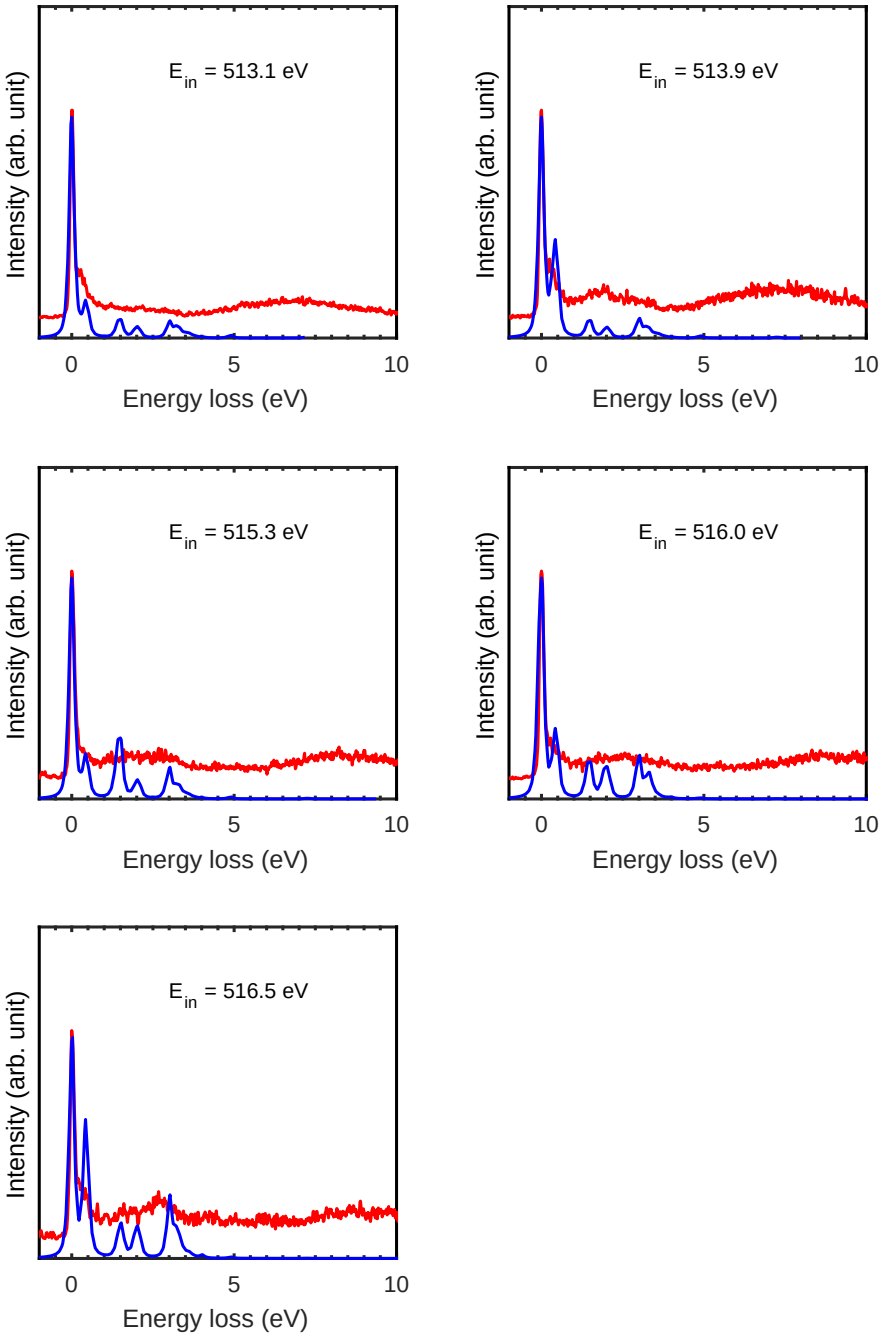

Figure 4.8: Experimental (blue line) and theoretical (red line) spectra of V L edge RIXS in $Lu_2V_2O_7$ at 25 K calculated with the weighting factors V^{3+}:V^{4+}:V^{5+} = 1:0:1.

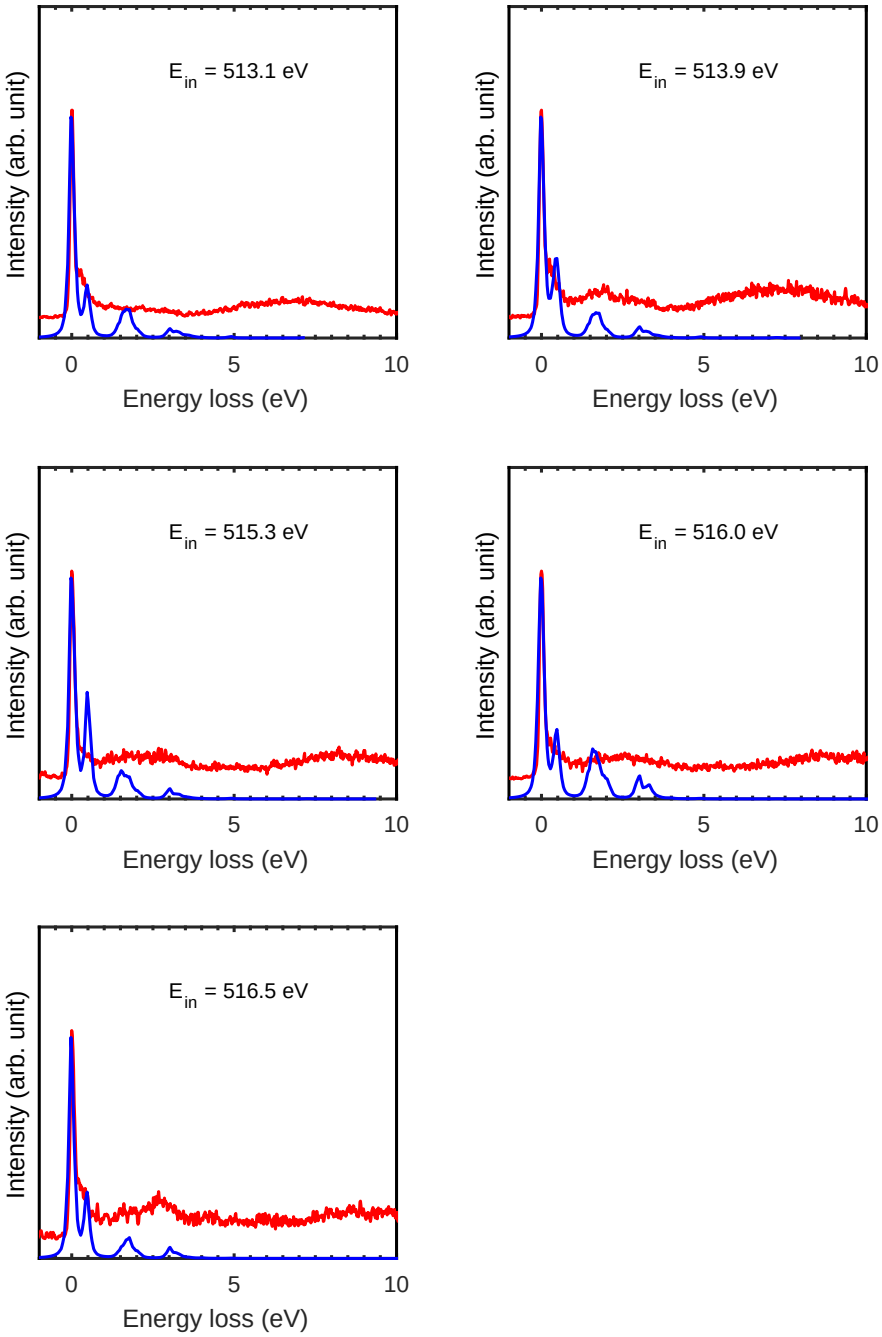

Figure 4.9: Experimental (blue line) and theoretical (red line) spectra of V L edge RIXS in $Lu_2V_2O_7$ at 25 K calculated with the weighting factors V^{3+}:V^{4+}:V^{5+} = 1:2:1.

Conclusions and perspectives

In this thesis, the local electronic structure of the ferromagnetic insulator $Lu_2V_2O_7$ and of type II multiferroics $RMnO_3$ (R = Tb, Dy) has been investigated using XAS and RIXS spectroscopic techniques. By comparing experimental and theoretical results, we have been able to be characterize quantitatively the crystal field using crystal field multiplet calculations. On the basis of the crystal field parameters obtained, we can now better understand the strongly correlated electron systems in these materials. The highlights of this thesis are briefly summarized:

- For the pyrochlore structure vanadate $Lu_2V_2O_7$ single crystal

  The measured XAS and RIXS spectra at the vanadium $L_{2,3}$ edges cannot be explained only by a V^{4+} monovalent state (with electronic configuration $3d^1$). With crystal field parameters (D_{3d}) at V site set to $10Dq = 1.5$ eV, $D_\tau = D_\sigma = 0.05$ eV, we have deduced that the system has mixed-valent state with the weight factors of V^{3+}:V^{4+}:V^{5+} = 1:2:1. From this mixed-valence state for vanadium, we suggested that the possible dynamical effects are present in this system due to the magnetic frustration.

- For the orthorhombic $RMnO_3$ (R = Tb, Dy) single crystal

  Combining element specific RIXS and XAS measurements at the Mn $L_{2,3}$ edges with crystal field multiplet calculations provides accurate parameters for the description of the tetragonal distortion of the Mn^{3+} environment in $TbMnO_3$. The crystal field parameters at the symmetry point D_{4h} were found as following: $10Dq = 1.6$ eV, $D_s = 0.31$ eV, $D_t = 0.06$ eV. Based on these values, a diagram of energy levels can be established. It is found that $\Delta e_g = 1.54$ eV (splitting between the energy level of e_g) and $\Delta t_{2g} = 0.63$ eV (splitting of energy level of t_{2g}). These values can be considered as a reliable reference to be compared with the band structure calculated with DFT. Note that a small energy difference between d_{z^2} and d_{xy} (shown in the established energy level diagram) is 0.06 eV, which suggests a mixed state.

  For $DyMnO_3$, using XAS and RIXS, the neutral electronic excitations at Mn $L_{2,3}$ and O K edges were probed. The results are similar to those of $TbMnO_3$. Considering Mn^{3+} ions at the a D_{4h} symmetry point, the local crystal field are parameterized in a reliable way by the comparison of experiments with theory. The crystal field parameters are: $10Dq = 1.6$ eV, $D_s = 0.36$ eV, $D_t = 0.06$ eV. The tetragonal splitting of e_g and t_{2g} branches are $\Delta e_g = 1.74$ eV and $\Delta t_{2g} = 0.78$ eV, respectively. Through comparison of the crystal field parameters between the $DyMnO_3$ and $TbMnO_3$, we showed that the tetragonal distortion of $DyMnO_3$ is slightly stronger. Note that this

small difference of D_s results in a t_{2g}-e_g orbital crossing. The rare earth might play a main role in this behavior.

The XAS and RIXS experimental investigation on rare earth Tb and Dy at the $N_{4,5}$ edges, have also been performed on the SEXTANTS beamline at SOLEIL synchrotron. The energy resolution of RIXS can reach 50 meV, which is the best resolution in the world for this soft X-ray energy range. With this high energy resolution, the crystal field effects were observed on the $4f$ orbital of rare earth. This opens a novel avenue for the research on crystal field effects that could influence the electronic structure of rare earth $4f$ orbital.

A temperature dependence is observed in the experimental RIXS spectra of Mn for $DyMnO_3$ when the incident energy is set at the feature of L_2. Through comparison of Boltzmann weighted RIXS calculation between at 25 K and at 300 K, no temperature dependence is shown. This behavior is probably due to the mixture of charge transfer effect which could increase the intensity of *d-d* excitations (such like in NiO [120]). However, in order to provide more precise explanations, further RIXS investigations with higher energy resolution ($\Delta E = 40$ meV) should be performed.

In $Lu_2V_2O_7$, magnon Hall effect was observed by Onose [16]. The original goal of $Lu_2V_2O_7$ studies was to observe the magnon excitations with an excitation energy of 260 meV predicted by Pereiro [71]. Nevertheless, the predicted energy was reconsidered to an average of 26 meV [17] after a recalculation. Thus, the observation of magnon excitation should be performed again with higher energy resolution (at least 15 meV). This demand in resolution is nowadays a challenge for experiments, even for the recently developed instruments.

Annexes

```
   10    1    0   14    2    4    1    1 SHELL03000000 SPIN03000000 INTER8 %
  orbit03000000 tensor11001000000 tensor21101000000 tensor01101000000
    0                        80998080            8065.47800     0000000
    1     2 1 12 1 10        00      0 00000000 0 8065.4790 .00       1
P 6  D 4
P 5  D 5
Mn3+ 2p06 3d04     4    0.0000   11.4151    7.1481    0.0462    0.0000HR99999999
Mn3+ 2p05 3d05     8  646.9810   12.2101    7.6491    6.8452    0.0592HR99999999
    6.9883    5.1794    2.9454
                  -99999999.
   -1
```

Figure 4.10: Template .rcg file of Mn^{3+}.

```
Y
    % vertical 1 1
 butler O3
 to    Oh
 to    D4h
 to    C4h
 endchain
 actor   0+ HAMILTONIAN ground  PRINTEIG
  OPER HAMILTONIAN
    BRANCH 0+ > 0 0+ > 0+    > 0+   1.0
  OPER SHELL2
    BRANCH 4+ > 0 0+ > 0+    > 0+   X40
    BRANCH 4+ > 0 2+ > 0+    > 0+   X42
    BRANCH 2+ > 0 2+ > 0+    > 0+   X22
  OPER SPIN2
    BRANCH 1+ > 0 1+ > ^0+   > 0+   0.0
 actor   0+ HAMILTONIAN excite  PRINTEIG
  OPER HAMILTONIAN
    BRANCH 0+ > 0 0+ > 0+    > 0+   1.0
  OPER SHELL2
    BRANCH 4+ > 0 0+ > 0+    > 0+   X40
    BRANCH 4+ > 0 2+ > 0+    > 0+   X42
    BRANCH 2+ > 0 2+ > 0+    > 0+   X22
  OPER SPIN2
    BRANCH 1+ > 0 1+ > ^0+   > 0+   0.0
 actor   1- left        transi PRINTTRANS
   oper MULTIPOLE
     branch  1- > 0 1- >  1- >  1-  1.000
 actor  -1- right       transi PRINTTRANS
   oper MULTIPOLE
     branch  1- > 0 1- >  1- > -1-  1.000
 actor   0- parallel    transi PRINTTRANS
   oper MULTIPOLE
     branch  1- > 0 1- > ^0- >  0-  1.000
  actor  0+  sz          ground PRINTTRANS 15
   OPER SPIN2
    branch 1+ > 0 1+ > ^0+   >  0+    1.0
  actor  0+  lz          ground PRINTTRANS 15
   OPER ORBIT2
    branch 1+ > 0 1+ > ^0+   >  0+    1.0

RUN
```

Figure 4.11: Template .rac file for the D_{4h} point group symmetry, where the symmetry is noted in terms of Butler.

```
energy_range 605 750
lorentzian 0.15 1e20 range 605 721
lorentzian 0.2 1e20 range 721 750
gaussian 0.2
old_racah      Mn3-D4h.rac_out
xy  Mn-D4h-right.xy 1000
spectrum operator 1- temp 2
xy Mn-D4h.xy 1000
spectrum operator -1- temp 2
xy Mn-D4h-parallel.xy 1000
spectrum operator 0- temp 2
xy Mn-D4h-perp.xy 1000
addlines operator  1- temp 2 scale 0.5
spectrum operator -1- temp 2 scale 0.5
xy Mn-D4h-3iso.xy 1000
spectrum temp 2
end
```

Figure 4.12: Template .plo file.

```
563     % to find C4 axis
564 -   u_c4 = cross(OMn-OO1,OMn-OO2);
565 -   u_c4 = u_c4/norm(u_c4);
566     % Coefficient of projection
567 -   position_ratio2_para = (u_LH * u_c4)^2;
568 -   position_ratio2_perp = 1 - position_ratio2_para ;
569     % Combination
570 -   ratio_project_para = position_ratio1_para + position_ratio2_para;
571 -   ratio_project_perp = position_ratio1_perp + position_ratio2_perp;
645 -   total_plo_y = ratio_project_para*para_plo_y  + ratio_project_perp*perp_plo_y;
```

Figure 4.13: Matlab code related to the part of polarization dependence.

Bibliography

[1] D. I. Khomskii, *Transition Metal Compounds*. Cambridge: Cambridge University Press, 2014.

[2] L. J. Ament, M. van Veenendaal, T. P. Devereaux, J. P. Hill, and J. van Den Brink, "Resonant inelastic X-ray scattering studies of elementary excitations," *Reviews of Modern Physics*, vol. 83, no. 2, p. 705, 2011.

[3] M. Sacchi, N. Jaouen, H. Popescu, R. Gaudemer, J. Tonnerre, S. Chiuzbaian, C. Hague, A. Delmotte, J. Dubuisson, G. Cauchon, *et al.*, "The sextants beamline at soleil: a new facility for elastic, inelastic and coherent scattering of soft X-rays," *Journal of Physics: Conference Series*, vol. 425, no. 7, p. 072018, 2013.

[4] S. G. Chiuzbăian, C. F. Hague, A. Avila, R. Delaunay, N. Jaouen, M. Sacchi, F. Polack, M. Thomasset, B. Lagarde, A. Nicolaou, *et al.*, "Design and performance of aerha, a high acceptance high resolution soft X-ray spectrometer," *Review of Scientific Instruments*, vol. 85, no. 4, p. 043108, 2014.

[5] W. Eerenstein, N. Mathur, and J. F. Scott, "Multiferroic and magnetoelectric materials," *Nature*, vol. 442, no. 7104, pp. 759–765, 2006.

[6] I. A. Sergienko and E. Dagotto, "Role of the Dzyaloshinskii-Moriya interaction in multiferroic perovskites," *Physical Review B*, vol. 73, no. 9, p. 094434, 2006.

[7] H. Katsura, N. Nagaosa, and A. V. Balatsky, "Spin current and magnetoelectric effect in noncollinear magnets," *Physical Review Letters*, vol. 95, no. 5, p. 057205, 2005.

[8] T. Kimura, T. Goto, H. Shintani, K. Ishizaka, T. Arima, and Y. Tokura, "Magnetic control of ferroelectric polarization," *Nature*, vol. 426, no. 6962, pp. 55–58, 2003.

[9] A. Flesch, G. Zhang, E. Koch, and E. Pavarini, "Orbital-order melting in rare-earth manganites: Role of superexchange," *Physical Review B*, vol. 85, p. 035124, 2012.

[10] X.-Y. Chen, L.-J. Chen, X.-B. Yang, Y.-J. Zhao, H.-C. Ding, and C.-G. Duan, "Tuning the polarization and magnetism in $BiCoO_3$ by strain and oxygen vacancy effect: A first-principle study," *Journal of Applied Physics*, vol. 111, no. 1, p. 013901, 2012.

[11] A.-M. Haghiri-Gosnet and J.-P. Renard, "CMR manganites: physics, thin films and devices," *Journal of Physics D: Applied Physics*, vol. 36, no. 8, p. R127, 2003.

[12] N. Hollmann, Z. Hu, T. Willers, L. Bohatý, P. Becker, A. Tanaka, H. H. Hsieh, H.-J. Lin, C. T. Chen, and L. H. Tjeng, "Local symmetry and magnetic anisotropy in multiferroic $MnWO_4$ and antiferromagnetic $CoWO_4$ studied by soft x-ray absorption spectroscopy," *Physical Review B*, vol. 82, p. 184429, 2010.

[13] F. de Groot and A. Kotani, *Core Level Spectroscopy of Solids*. Advances in Condensed Matter Science, Boca Raton, FL: CRC Press, 2008.

[14] R. Feyerherm, E. Dudzik, N. Aliouane, and D. Argyriou, "Commensurate Dy magnetic ordering associated with incommensurate lattice distortion in multiferroic $DyMnO_3$," *Physical Review B*, vol. 73, no. 18, p. 180401, 2006.

[15] O. Prokhnenko, R. Feyerherm, E. Dudzik, S. Landsgesell, N. Aliouane, L. Chapon, and D. Argyriou, "Enhanced ferroelectric polarization by induced Dy spin order in multiferroic $DyMnO_3$," *Physical Review Letters*, vol. 98, no. 5, p. 057206, 2007.

[16] Y. Onose, T. Ideue, H. Katsura, Y. Shiomi, N. Nagaosa, and Y. Tokura, "Observation of the magnon Hall effect," *Science*, vol. 329, no. 5989, pp. 297–299, 2010.

[17] M. Pereiro, D. Yudin, J. Chico, C. Etz, O. Eriksson, and A. Bergman, "Corrigendum: Topological excitations in a kagome magnet," *Nature Communications*, vol. 6, p. 7881, 2015.

[18] H. Ichikawa, L. Kano, M. Saitoh, S. Miyahara, N. Furukawa, J. Akimitsu, T. Yokoo, T. Matsumura, M. Takeda, and K. Hirota, "Orbital ordering in ferromagnetic $Lu_2V_2O_7$," *Journal of the Physical Society of Japan*, vol. 74, no. 3, pp. 1020–1025, 2005.

[19] A. A. Biswas and Y. Jana, "Crystal-field, exchange interactions and magnetism in pyrochlore ferromagnet $R_2V_2O_7$ (R^{3+}=Y,Lu)," *Journal of Magnetism and Magnetic Materials*, vol. 329, pp. 118–124, 2013.

[20] M. Abbate, H. Pen, M. Czyżyk, F. De Groot, J. Fuggle, Y. Ma, C. Chen, F. Sette, A. Fujimori, Y. Ueda, *et al.*, "Soft X-ray absorption spectroscopy of vanadium oxides," *Journal of Electron Spectroscopy and Related Phenomena*, vol. 62, no. 1-2, pp. 185–195, 1993.

[21] K. Ishii, K. Tsutsui, Y. Endoh, T. Tohyama, S. Maekawa, M. Hoesch, K. Kuzushita, M. Tsubota, T. Inami, J. Mizuki, *et al.*, "Momentum dependence of charge excitations in the electron-doped superconductor $Nd_{1.85}Ce_{0.15}CuO_4$: a resonant inelastic X-ray scattering study," *Physical Review Letters*, vol. 94, no. 20, p. 207003, 2005.

[22] M. Hasan, E. Isaacs, Z.-X. Shen, L. Miller, K. Tsutsui, T. Tohyama, and S. Maekawa, "Electronic structure of Mott insulators studied by inelastic X-ray scattering," *Science*, vol. 288, no. 5472, pp. 1811–1814, 2000.

[23] J. Chen, J. Lee, S. Huang, K. Lu, H. Jeng, C. Chen, S. Haw, T. Chou, S. Chen, N. Hiraoka, *et al.*, "Intra-and intersie eletronic excitations in multiferroic $TbMnO_3$ probed by resonant inelastic X-ray scattering," *Physical Review B*, vol. 82, no. 9, p. 094442, 2010.

[24] B. H. Kim, G. Khaliullin, and B. Min, "Electronic excitations in the edge-shared relativistic Mott insulator: Na_2IrO_3," *Physical Review B*, vol. 89, no. 8, p. 081109, 2014.

[25] H. Schmid, "Multi-ferroic magnetoelectrics," *Ferroelectrics*, vol. 162, no. 1, pp. 317–338, 1994.

[26] Optical Conductivity Group at LPEM, ESPCI, "https://www.lpem.espci.fr/ocg/."

[27] N. A. Spaldin and M. Fiebig, "The renaissance of magnetoelectric multiferroics," *Science*, vol. 309, no. 5733, pp. 391–392, 2005.

[28] P. Curie, "Sur la symétrie dans les phénomenes physiques, symétrie d'un champ électrique et d'un champ magnétique," *Journal de Physique Théorique et Appliquée*, vol. III, 3ème Série, no. 3, pp. 393–415, 1894.

[29] W. Brown Jr, R. Hornreich, and S. Shtrikman, "Upper bound on the magnetoelectric susceptibility," *Physical Review*, vol. 168, no. 2, p. 574, 1968.

[30] A. Chen and F. Chernow, "Nature of ferroelectricity in KNO_3," *Physical Review*, vol. 154, no. 2, p. 493, 1967.

[31] M. A. Saifi and L. Cross, "Dielectric properties of strontium titanate at low temperature," *Physical Review B*, vol. 2, no. 3, p. 677, 1970.

[32] T. Kimura, S. Ishihara, H. Shintani, T. Arima, K. Takahashi, K. Ishizaka, and Y. Tokura, "Distorted perovskite with e_g^1 configuration as a frustrated spin system," *Physical Review B*, vol. 68, no. 6, p. 060403, 2003.

[33] H. Xiang, S.-H. Wei, M.-H. Whangbo, and J. L. Da Silva, "Spin-orbit coupling and ion displacements in multiferroic $TbMnO_3$," *Physical Review Letters*, vol. 101, no. 3, p. 037209, 2008.

[34] S. Dhesi, A. Mirone, C. De Nadai, P. Ohresser, P. Bencok, N. Brookes, P. Reutler, A. Revcolevschi, A. Tagliaferri, O. Toulemonde, *et al.*, "Unraveling orbital ordering in $La_{0.5}Sr_{1.5}MnO_4$," *Physical Review Letters*, vol. 92, no. 5, p. 056403, 2004.

[35] Y. Tokura and N. Nagaosa, "Orbital physics in transition-metal oxides," *Science*, vol. 288, no. 5465, pp. 462–468, 2000.

[36] J. Alonso, M. Martinez-Lope, M. Casais, and M. Fernández-Diaz, "Evolution of the Jahn–Teller distortion of Mno6 octahedra in $RMnO_3$ perovskites (R = Pr, Nd, Dy, Tb, Ho, Er, Y): a neutron diffraction study," *Inorganic Chemistry*, vol. 39, no. 5, pp. 917–923, 2000.

[37] D. Senff, N. Aliouane, D. Argyriou, A. Hiess, L. Regnault, P. Link, K. Hradil, Y. Sidis, and M. Braden, "Magnetic excitations in a cycloidal magnet: the magnon spectrum of multiferroic $TbMnO_3$," *Journal of Physics: Condensed Matter*, vol. 20, no. 43, p. 434212, 2008.

[38] M. Kenzelmann, A. B. Harris, S. Jonas, C. Broholm, J. Schefer, S. Kim, C. Zhang, S.-W. Cheong, O. P. Vajk, and J. W. Lynn, "Magnetic inversion symmetry breaking and ferroelectricity in $TbMnO_3$," *Physical Review Letters*, vol. 95, no. 8, p. 087206, 2005.

[39] G. Lawes, A. B. Harris, T. Kimura, N. Rogado, R. J. Cava, A. Aharony, O. Entin-Wohlman, T. Yildirim, M. Kenzelmann, C. Broholm, *et al.*, "Magnetically driven ferroelectric order in $Ni_3V_2O_8$," *Physical Review Letters*, vol. 95, no. 8, p. 087205, 2005.

[40] H. Walker, F. Fabrizi, L. Paolasini, F. de Bergevin, J. Herrero-Martin, A. Boothroyd, D. Prabhakaran, and D. McMorrow, "Femtoscale magnetically induced lattice distortions in multiferroic $TbMnO_3$," *Science*, vol. 333, no. 6047, pp. 1273–1276, 2011.

[41] S. Ishihara, J. Inoue, and S. Maekawa, "Effective hamiltonian in manganites: mstudy of the orbital and spin structures," *Physical Review B*, vol. 55, no. 13, p. 8280, 1997.

[42] A. Munoz, M. Casáis, J. Alonso, M. Martínez-Lope, J. Martinez, and M. Fernández-Díaz, "Complex magnetism and magnetic structures of the metastable $HoMnO_3$ perovskite," *Inorganic Chemistry*, vol. 40, no. 5, pp. 1020–1028, 2001.

[43] S. Quezel, F. Tcheou, J. Rossat-Mignod, G. Quezel, and E. Roudaut, "Magnetic structure of the perovskite-like compound $TbMnO_3$," *Physica B+ C*, vol. 86, pp. 916–918, 1977.

[44] J. S. Smart and S. Greenwald, "Crystal structure transitions in antiferromagnetic compounds at the Curie temperature," *Physical Review*, vol. 82, no. 1, p. 113, 1951.

[45] M. Date, J. Kanamori, and M. Tachiki, "Origin of magnetoelectric effect in Cr_2O_3," *Journal of the Physical Society of Japan*, vol. 16, no. 12, pp. 2589–2589, 1961.

[46] G. Rado and V. Folen, "Magnetoelectric effects in antiferromagnetics," *Journal of Applied Physics*, vol. 33, no. 3, pp. 1126–1132, 1962.

[47] K. Siratori and E. Kita, "Magnetoelectric effect in $ZnCr_2Se_4$ with screw spin structure," *Journal of the Physical Society of Japan*, vol. 48, no. 5, pp. 1443–1448, 1980.

[48] J. Hu, "Microscopic origin of magnetoelectric coupling in noncollinear multiferroics," *Physical Review Letters*, vol. 100, no. 7, p. 077202, 2008.

[49] I. Dzyaloshinskii, "Theory of helicoidal structures in antiferromagnets. 1. Nonmetals," *Soviet Physics Journal of Experimental and Theoretical Physics*, vol. 19, pp. 960–971, 1964.

[50] T. Moriya, "Anisotropic superexchange interaction and weak ferromagnetism," *Physical Review*, vol. 120, no. 1, p. 91, 1960.

[51] S.-W. Cheong and M. Mostovoy, "Multiferroics: a magnetic twist for ferroelectricity," *Nature Materials*, vol. 6, no. 1, pp. 13–20, 2007.

[52] J. Chen, J. Lee, C. Chen, T. Chou, K. Lu, S. Haw, K. Liang, C. Chen, H. Jeng, S. Huang, *et al.*, "Bonding anisotropy in multiferroic $TbMnO_3$ probed by polarization dependent X-ray absorption spectroscopy," *Applied Physics Letters*, vol. 94, no. 4, p. 044105, 2009.

[53] K. Wu, I. Gou, C. Luo, T. Uen, J.-Y. Lin, J. Juang, C. Chen, J. Lee, and J. Chen, "Anisotropic electronic structure in single crystalline orthorhombic $TbMnO_3$ thin films," *Thin Solid Films*, vol. 518, no. 8, pp. 2275–2279, 2010.

[54] H. Zenia, G. Gehring, and W. Temmerman, "Orbital ordering in cubic $LaMnO_3$ from first principles calculations," *New Journal of Physics*, vol. 7, no. 1, p. 257, 2005.

[55] C. Castleton and M. Altarelli, "Orbital ordering in the manganites: resonant x-ray scattering predictions at the manganese L_{II} and L_{III} edges," *Physical Review B*, vol. 62, no. 2, p. 1033, 2000.

[56] M. E. Bolivar Guarin, A. d. M. Moreira, and N. L. Speziali, "Structural study of manganites: site occupancy and coexistence of hexagonal and orthorhombic phases," *Journal of Applied Crystallography*, vol. 46, no. 3, pp. 644–648, 2013.

[57] J. Kanamori, "Crystal distortion in magnetic compounds," *Journal of Applied Physics*, vol. 31, no. 5, pp. S14–S23, 1960.

[58] T. Mori, K. Aoki, N. Kamegashira, T. Shishido, and T. Fukuda, "Crystal structure of $DyMnO_3$," *Materials Letters*, vol. 42, no. 6, pp. 387–389, 2000.

[59] N. Narayanan, P. Graham, N. Reynolds, F. Li, P. Rovillain, J. Hester, J. Kimpton, M. Yethiraj, G. McIntyre, W. Hutchison, *et al.*, "Subpicometer-scale atomic displacements and magnetic properties in the oxygen-isotope substituted multiferroic $DyMnO_3$," *Physical Review B*, vol. 95, no. 7, p. 075154, 2017.

[60] T. Kimura, G. Lawes, T. Goto, Y. Tokura, and A. Ramirez, "Magnetoelectric phase diagrams of orthorhombic $RMnO_3$ (R = Gd, Tb, and Dy)," *Physical Review B*, vol. 71, no. 22, p. 224425, 2005.

[61] J. Strempfer, B. Bohnenbuck, M. Mostovoy, N. Aliouane, D. Argyriou, F. Schrettle, J. Hemberger, A. Krimmel, and M. v. Zimmermann, "Absence of commensurate ordering at the polarization flop transition in multiferroic $DyMnO_3$," *Physical Review B*, vol. 75, no. 21, p. 212402, 2007.

[62] M. Iliev, M. Abrashev, J. Laverdiere, S. Jandl, M. Gospodinov, Y.-Q. Wang, and Y.-Y. Sun, "Distortion-dependent Raman spectra and mode mixing in $RMnO_3$ perovskites (R = La, Pr, Nd, Sm, Eu, Gd, Tb, Dy, Ho, Y)," *Physical Review B*, vol. 73, no. 6, p. 064302, 2006.

[63] M. Iliev, M. Abrashev, H.-G. Lee, V. Popov, Y. Sun, C. Thomsen, R. Meng, and C. Chu, "Raman spectroscopy of orthorhombic perovskitelike $YMnO_3$ and $LaMnO_3$," *Physical Review B*, vol. 57, no. 5, p. 2872, 1998.

[64] R. Feyerherm, E. Dudzik, O. Prokhnenko, and D. Argyriou, "Rare earth magnetism and ferroelectricity in $RMnO_3$," in *Journal of Physics: Conference Series*, vol. 200, p. 012032, IOP Publishing, 2010.

[65] V. Cuartero, S. Lafuerza, G. Subías, J. García, E. Schierle, J. Blasco, and J. Herrero-Albillos, "X-ray magnetic circular dichroism study of the magnetic anisotropy on $TbMnO_3$," *Physical Review B*, vol. 91, no. 16, p. 165111, 2015.

[66] N. Agladze and M. Popova, "Hyperfine structure in optical spectra of $LiYF_4$-Ho," *Solid State Communications*, vol. 55, no. 12, pp. 1097–1100, 1985.

[67] G. Liu and B. Jacquier, *Spectroscopic properties of rare earths in optical materials*, vol. 83. Springer Science & Business Media, 2006.

[68] W. Carnall, G. Goodman, K. Rajnak, and R. Rana, "A systematic analysis of the spectra of the lanthanides doped into single crystal LaF_3," *The Journal of Chemical Physics*, vol. 90, no. 7, pp. 3443–3457, 1989.

[69] D. Xiao, M.-C. Chang, and Q. Niu, "Berry phase effects on electronic properties," *Reviews of Modern Physics*, vol. 82, no. 3, p. 1959, 2010.

[70] N. Nagaosa, J. Sinova, S. Onoda, A. MacDonald, and N. Ong, "Anomalous Hall effect," *Reviews of Modern Physics*, vol. 82, no. 2, p. 1539, 2010.

[71] M. Pereiro, D. Yudin, J. Chico, C. Etz, O. Eriksson, and A. Bergman, "Topological excitations in a kagome magnet," *Nature Communications*, vol. 5, 2014.

[72] L. Balents, "Spin liquids in frustrated magnets," *Nature*, vol. 464, no. 7286, pp. 199–208, 2010.

[73] D. J. P. Morris, D. Tennant, S. Grigera, B. Klemke, C. Castelnovo, R. Moessner, C. Czternasty, M. Meissner, K. Rule, J.-U. Hoffmann, *et al.*, "Dirac strings and magnetic monopoles in the spin ice $Dy_2Ti_2O_7$," *Science*, vol. 326, no. 5951, pp. 411–414, 2009.

[74] T. Fennell, P. Deen, A. Wildes, K. Schmalzl, D. Prabhakaran, A. Boothroyd, R. Aldus, D. McMorrow, and S. Bramwell, "Magnetic Coulomb phase in the spin ice $Ho_2Ti_2O_7$," *Science*, vol. 326, no. 5951, pp. 415–417, 2009.

[75] H. Kadowaki, Y. Ishii, K. Matsuhira, and Y. Hinatsu, "Neutron scattering study of dipolar spin ice $Ho_2Sn_2O_7$: frustrated pyrochlore magnet," *Physical Review B*, vol. 65, no. 14, p. 144421, 2002.

[76] S. T. Bramwell and M. J. Gingras, "Spin ice state in frustrated magnetic pyrochlore materials," *Science*, vol. 294, no. 5546, pp. 1495–1501, 2001.

[77] M. Hirschberger, J. W. Krizan, R. Cava, and N. Ong, "Large thermal Hall conductivity of neutral spin excitations in a frustrated quantum magnet," *Science*, vol. 348, no. 6230, pp. 106–109, 2015.

[78] H. Takatsu, H. Kadowaki, T. J. Sato, J. W. Lynn, Y. Tabata, T. Yamazaki, and K. Matsuhira, "Quantum spin fluctuations in the spin-liquid state of $Tb_2Ti_2O_7$," *Journal of Physics: Condensed Matter*, vol. 24, no. 5, p. 052201, 2011.

[79] M. Elhajal, B. Canals, and C. Lacroix, "Symmetry breaking due to Dzyaloshinsky-Moriya interactions in the kagomé lattice," *Physical Review B*, vol. 66, no. 1, p. 014422, 2002.

[80] M. Mena, R. Perry, T. Perring, M. Le, S. Guerrero, M. Storni, D. Adroja, C. Rüegg, and D. McMorrow, "Spin-wave spectrum of the quantum ferromagnet on the pyrochlore lattice $Lu_2V_2O_7$," *Physical Review Letters*, vol. 113, no. 4, p. 047202, 2014.

[81] W. Schülke, *Electron dynamics by inelastic X-ray scattering*, vol. 7 of *Oxford Series on Synchrotron Radiation*. Oxford: Oxford University Press, 2007.

[82] R. D. Cowan, *The Theory of Atomic Spectra and Structure*, vol. 3 of *Los Alamos Series in Basic and Applied Sciences*. Berkeley: University of California Press, 1981.

[83] B. Thole, G. van Der Laan, and P. Butler, "Spin-mixed ground state of fe phthalocyanine and the temperature-dependent branching ratio in X-ray absorption spectroscopy," *Chemical Physics Letters*, vol. 149, no. 3, pp. 295–299, 1988.

[84] M. Finazzi, G. Ghiringhelli, O. Tjernberg, P. Ohresser, and N. Brookes, "Radiationless Raman versus Auger behavior at the Cu L_3 resonance of CuO and Cu_2O," *Physical Review B*, vol. 61, no. 7, p. 4629, 2000.

[85] G. Ghiringhelli, N. Brookes, E. Annese, H. Berger, C. Dallera, M. Grioni, L. Perfetti, A. Tagliaferri, and L. Braicovich, "Low energy electronic excitations in the layered cuprates studied by copper L_3 resonant inelastic X-ray scattering," *Physical Review Letters*, vol. 92, no. 11, p. 117406, 2004.

[86] J. Schlappa, K. Wohlfeld, K. Zhou, M. Mourigal, M. Haverkort, V. Strocov, L. Hozoi, C. Monney, S. Nishimoto, S. Singh, *et al.*, "Spin-orbital separation in the quasi-one-dimensional Mott insulator Sr_2CuO_3," *Nature*, vol. 485, no. 7396, pp. 82–85, 2012.

[87] G. Ghiringhelli, A. Piazzalunga, C. Dallera, T. Schmitt, V. Strocov, J. Schlappa, L. Patthey, X. Wang, H. Berger, and M. Grioni, "Observation of two nondispersive magnetic excitations in NiO by resonant inelastic soft-X-ray scattering," *Physical Review Letters*, vol. 102, no. 2, p. 027401, 2009.

[88] H. Yavaş, M. van Veenendaal, J. van den Brink, L. Ament, A. Alatas, B. Leu, M. Apostu, N. Wizent, G. Behr, W. Sturhahn, *et al.*, "Observation of phonons with resonant inelastic X-ray scattering," *Journal of Physics: Condensed Matter*, vol. 22, no. 48, p. 485601, 2010.

[89] R. Kraus, M. Schrade, R. Schuster, M. Knupfer, A. Revcolevschi, B. Büchner, and J. Geck, "Signatures of electronic polarons in $La_{1-x}Sr_{1+x}MnO_4$ observed by electron energy-loss spectroscopy," *Physical Review B*, vol. 83, no. 16, p. 165130, 2011.

[90] L. Braicovich, J. van den Brink, V. Bisogni, M. M. Sala, L. Ament, N. Brookes, G. De Luca, M. Salluzzo, T. Schmitt, V. Strocov, *et al.*, "Magnetic excitations and phase separation in the underdoped $La_{2-x}Sr_xCuO_4$ superconductor measured by resonant inelastic X-ray scattering," *Physical Review Letters*, vol. 104, no. 7, p. 077002, 2010.

[91] J. Stöhr, "Exploring the microscopic origin of magnetic anisotropies with X-ray magnetic circular dichroism (XMCD) spectroscopy," *Journal of Magnetism and Magnetic Materials*, vol. 200, no. 1, pp. 470–497, 1999.

[92] Lawrence Berkeley National Laboratory, Center for X-Ray Optics, "http://www.cxro.lbl.gov/."

[93] L.-C. Duda, T. Schmitt, M. Magnuson, J. Forsberg, A. Olsson, J. Nordgren, K. Okada, and A. Kotani, "Resonant inelastic X-ray scattering at the oxygen k resonance of NiO: nonlocal charge transfer and double-singlet excitations," *Physical Review Letters*, vol. 96, no. 6, p. 067402, 2006.

[94] F. de Groot, *X-ray absorption of transition metal oxides*. PhD thesis, University of Nijmegen (The Nethelands), 1991.

[95] J. Goedkoop, *X-ray dichroism of rare-earth materials*. PhD thesis, University of Nijmegen (The Nethelands), 1989.

[96] M.-A. Arrio, *Dichroïsme circulaire magnétique d'aimants à base moléculaire par absorption des rayons X*. PhD thesis, Université Paris Sud (France), 1995.

[97] P. Butler, *Point group symmetry: Applications, methods and tables*. Plenum, New York, 1981.

[98] R. Burns, *Mineralogical applications of crystal field theory*. Cambridge Topics in Mineral Physics and Chemistry, 1993.

[99] A. Kramida, Y. Ralchenko, J. Reader, *et al.*, "Nist atomic spectra database (ver. 5.2)," *National Institute of Standards and Technology, Gaithersburg, MD*, 2013.

[100] A. Moewes, M. M. Grush, T. A. Callcott, and D. L. Ederer, "Decay mechanisms of the 4d core hole through the 4d-4f resonance in dysprosium," *Physical Review B*, vol. 60, no. 23, p. 15728, 1999.

[101] A. Moewes, R. P. Winarski, D. L. Ederer, M. M. Grush, and T. A. Callcott, "Study of 4f inner shell excitations in Gd and Tb using resonant inelastic soft X-ray scattering," *Journal of Electron Spectroscopy and Related Phenomena*, vol. 101, pp. 617–622, 1999.

[102] H. Ogasawara and A. Kotani, "Calculation of magnetic circular dichroism of rare-earth elements," *Journal of the Physical Society of Japan*, vol. 64, no. 4, pp. 1394–1401, 1995.

[103] M. Haverkort, M. Zwierzycki, and O. Andersen, "Multiplet ligand-field theory using wannier orbitals," *Physical Review B*, vol. 85, no. 16, p. 165113, 2012.

[104] Y. Lu, M. Höppner, O. Gunnarsson, and M. Haverkort, "Efficient real-frequency solver for dynamical mean-field theory," *Physical Review B*, vol. 90, no. 8, p. 085102, 2014.

[105] M. Haverkort, G. Sangiovanni, P. Hansmann, A. Toschi, Y. Lu, and S. Macke, "Bands, resonances, edge singularities and excitons in core level spectroscopy investigated within the dynamical mean-field theory," *Europhysics Letters*, vol. 108, no. 5, p. 57004, 2014.

[106] X. Zhang, H. Zhou, L. Yu, H. J. Gardner, S. von Molnár, C. Wiebe, and P. Xiong, "Electronic transport in the ferromagnetic pyrochlore $Lu_2V_2O_7$: Role of magnetization," *Physical Review B*, vol. 91, no. 20, p. 205107, 2015.

[107] L. Soderholm and J. Greedan, "Relationship between crystal structure and magnetic properties of $(RE)_2V_2O_7$; RE= Lu, Yb, Tm," *Materials Research Bulletin*, vol. 17, no. 6, pp. 707–713, 1982.

[108] T. Mizokawa, "Metal-insulator transitions: Orbital control," *Nature Physics*, vol. 9, no. 10, pp. 612–613, 2013.

[109] M. W. Haverkort, Z. Hu, A. Tanaka, W. Reichelt, S. V. Streltsov, M. A. Korotin, V. I. Anisimov, H. H. Hsieh, H.-J. Lin, C. T. Chen, D. I. Khomskii, and L. H. Tjeng, "Orbital-assisted metal-insulator transition in VO_2," *Physical Review Letters*, vol. 95, p. 196404, 2005.

[110] H. He, A. X. Gray, P. Granitzka, J. W. Jeong, N. P. Aetukuri, R. Kukreja, L. Miao, S. A. Breitweiser, J. Wu, Y. B. Huang, P. Olalde-Velasco, J. Pelliciari, W. F. Schlotter, E. Arenholz, T. Schmitt, M. G. Samant, S. S. P. Parkin, H. A. Dürr, and L. A.

Wray, "Measurement of collective excitations in VO_2 by resonant inelastic X-ray scattering," *Physical Review B*, vol. 94, p. 161119, 2016.

[111] G. Knoke, A. Niazi, J. Hill, and D. Johnston, "Synthesis, structure, and ferromagnetism of the oxygen defect pyrochlore system $Lu_2V_2O_{7-x}$ (x= 0.40–0.65)," *Physical Review B*, vol. 76, no. 5, p. 054439, 2007.

[112] H. Zhou, E. Choi, J. Souza, J. Lu, Y. Xin, L. Lumata, B. Conner, L. Balicas, J. Brooks, J. Neumeier, *et al.*, "Magnetic-polaron-driven magnetoresistance in the pyrochlore $Lu_2V_2O_7$," *Physical Review B*, vol. 77, no. 2, p. 020411, 2008.

[113] T. Ideue, Y. Onose, H. Katsura, Y. Shiomi, S. Ishiwata, N. Nagaosa, and Y. Tokura, "Effect of lattice geometry on magnon Hall effect in ferromagnetic insulators," *Physical Review B*, vol. 85, no. 13, p. 134411, 2012.

[114] J. Zaanen, G. A. Sawatzky, and J. W. Allen, "Band gaps and electronic structure of transition-metal compounds," *Physical Review Letters*, vol. 55, pp. 418–421, 1985.

[115] M. van Veenendaal, P. Carra, and B. T. Thole, "X-ray resonant Raman scattering in the rare earths," *Physical Review B*, vol. 54, pp. 16010–16023, 1996.

[116] E. Stavitski and F. M. De Groot, "The CTM4XAS program for EELS and XAS spectral shape analysis of transition metal L edges," *Micron*, vol. 41, no. 7, pp. 687–694, 2010.

[117] J. Laverock, B. Chen, A. Preston, K. Smith, N. R. Wilson, G. Balakrishnan, P.-A. Glans, and J.-H. Guo, "Electronic structure of the kagome staircase compounds $Ni_3V_2O_8$ and $Co_3V_2O_8$," *Physical Review B*, vol. 87, no. 12, p. 125133, 2013.

[118] M. M. van Schooneveld, R. Kurian, A. Juhin, K. Zhou, J. Schlappa, V. N. Strocov, T. Schmitt, and F. M. de Groot, "Electronic structure of CoO nanocrystals and a single crystal probed by resonant X-ray emission spectroscopy," *The Journal of Physical Chemistry C*, vol. 116, no. 29, pp. 15218–15230, 2012.

[119] Q.-H. Wu, A. Thissen, W. Jaegermann, M. Schüz, and P. C. Schmidt, "Resonant photoemission spectroscopy study of electronic structure of V_2O_5," *Chemical Physics Letters*, vol. 430, no. 4, pp. 309–313, 2006.

[120] G. Ghiringhelli, M. Matsubara, C. Dallera, F. Fracassi, R. Gusmeroli, A. Piazzalunga, A. Tagliaferri, N. Brookes, A. Kotani, and L. Braicovich, "NiO as a test case for high resolution resonant inelastic soft x-ray scattering," *Journal of Physics: Condensed Matter*, vol. 17, no. 35, p. 5397, 2005.

Part I

Publications

Chapter 1

article $TbMnO_3$

JOURNAL OF APPLIED PHYSICS **122**, 194101 (2017)

Crystal-field excitations in multiferroic $TbMnO_3$ by Mn L_3 and O K resonant inelastic X-ray scattering

Jiatai Feng,[1] Amélie Juhin,[2] Renaud Delaunay,[1,3] Romain Jarrier,[1,3] Nicolas Jaouen,[3] Alessandro Nicolaou,[3] Ryan Sinclair,[4] Haidong Zhou,[4] Jean-Michel Mariot,[1,3] and Sorin G. Chiuzbăian[1,3,a)]

[1]*Sorbonne Universités, UPMC Univ Paris 06, CNRS, Laboratoire de Chimie Physique–Matière et Rayonnement (UMR 7614), 4 place Jussieu, 75252 Paris Cedex 05, France*
[2]*Sorbonne Universités, UPMC Univ Paris 06, CNRS, IRD, MNHN, Institut de Minéralogie, de Physique des Matériaux et de Cosmochimie (UMR 7590), 4 place Jussieu, 75252 Paris Cedex 05, France*
[3]*Synchrotron SOLEIL, L'Orme des Merisiers, Saint-Aubin, B. P. 48, 91192 Gif-sur-Yvette, France*
[4]*Department of Physics and Astronomy, Experimental Condensed Matter Physics, University of Tennessee, 407A Nielsen Physics Building, Knoxville, Tennessee 37996-1200, USA*

(Received 16 June 2017; accepted 28 October 2017; published online 16 November 2017)

d–d excitations in multiferroic $TbMnO_3$ have been investigated by X-ray absorption spectroscopy and resonant inelastic X-ray scattering at the Mn $L_{3,2}$ and O K edges. Confrontation between experimental data and multiplet crystal-field calculations performed for Mn^{3+} ions in D_{4h} symmetry has enabled us to identify the origin of the observed excitations and has provided reliable manganese crystal-field parameters that enter the description of the antisymmetric exchange interaction responsible for the multiferroicity in this compound. *Published by AIP Publishing.*
https://doi.org/10.1063/1.4990683

I. INTRODUCTION

Magnetic ferroelectric materials, usually referred to as multiferroics, are presently one of the most actively studied fields in solid state physics.[1,2] Interest in multiferroics arises from the prospect of controlling magnetic polarization, **M**, by means of an applied electric field or, inversely, by using a magnetic field to switch electrical polarization **P**. The interdependence of **M** and **P** is clearly inspiring for applications in the field of memory devices and spintronics. Two main classes of multiferroics have been identified.[2,3] For type-I multiferroics, the ferroelectricity is driven by structural effects generally described as ionic displacements starting from a centrosymmetric structure. $BiFeO_3$ is a renowned example with a large **P**, on the order of 100 μC cm^{-2}. In the case of type-II multiferroics, the electric polarization arises specifically as a consequence of the breaking of the magnetic order inversion symmetry. One of the most prominent examples in this class is $TbMnO_3$[4–6] where a spiral magnetic structure, present below 28 K, results in an electric polarization ascribed to electronic charge/spin currents.[7,8] When the inversion symmetry of the magnetic structure is broken, ferroelectric polarization can develop. While the polarization **P** obtained for $TbMnO_3$ is relatively small, about 0.06 μC cm^{-2}, the displayed magnetoelectric coupling between **M** and **P** is particularly strong.[4]

In more recent studies on $TbMnO_3$, Wilkins *et al.*[9] have produced evidence in favor of two noncollinear magnetic structures below 28 K, while Walker *et al.* have indicated that ionic displacements on a femtometer scale are present when a magnetic field is applied.[10,11] Therefore, it is likely that the origin of ferroelectric polarization in $TbMnO_3$ is very complex and may well involve some aspects of both type-II and type-I materials. A crucial ingredient for answering this question is the value of the crystal field (CF) acting on the transition-metal sites. For instance, the knowledge of the CF can be used as benchmark for the electronic structure calculations in both types of multiferroics,[12,13] as it includes the effective on-site electronic correlations. Furthermore, the single ion magnetic anisotropy of Mn^{3+} ions depends explicitly on the 3*d* CF splittings[14,15] and plays a pivotal role in the antisymmetric exchange interaction which drives the type-II multiferroicity. This paper deals with the quantification of the CF on Mn sites in $TbMnO_3$.

In an ideal ABO_3 perovskite structure, corner-sharing BO_6 octahedra are stacked along equivalent [1 0 0] directions, where A is a large radius cation (e.g., alkaline earths, some 4*d* transition metals, and rare earths) and B is a small radius 3*d* transition-metal cation. The A cations are located at the center of the cuboctahedral void created by the assembly of eight BO_6 octahedra. In the rare-earth manganites, A and B are rare earth and manganese trivalent ions (Mn^{3+}), respectively. The strain due to the large mismatch between the volume of the rare-earth ion and that of the void between the MnO_6 octahedra is at the origin of the departure from the ideal cubic perovskite structure in rare-earth manganites: the so-called $GdFeO_3$ orthorhombic distortion, i.e., a symmetry lowering from the $Pm\bar{3}m$ to the $Pbnm$ space group due to a cooperative rotation of the MnO_6 octahedra along the orthorhombic [0 1 0] and [0 0 1] directions [see Figs. 1(a) and 1(b)]. This distortion alters the Mn–O–Mn bond angle from 180° in the undistorted structure to ≈ 150°, a much smaller value. The octahedral environment of the Mn^{3+} ($3d^4$) ion splits the 3*d* atomic level into t_{2g} and e_g orbitals, leading to the high-spin $t_{2g}^3 e_g^1$ configuration. According to the Jahn–Teller theorem, the degeneracy of these orbitals should be lifted by distorting the BO_6

a)Author to whom correspondence should be addressed: gheorghe.chiuzbaian@upmc.fr

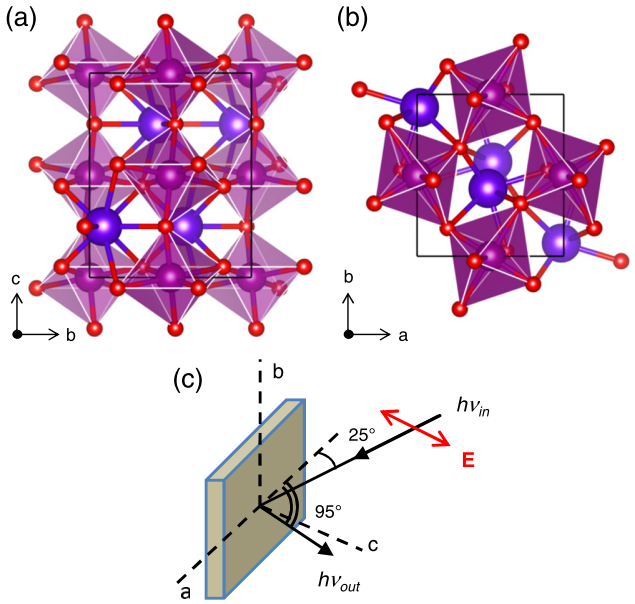

FIG. 1. $TbMnO_3$ crystalline structure and experimental arrangement. (a) and (b) Tilt of the MnO_6 octahedra as viewed facing the **a** and **c** axis, respectively. (c) Layout of the scattering geometry used in the RIXS measurements. **E** denotes the electric vector of the incoming LH polarized light (π polarization).

octahedra.[16] In the case of $TbMnO_3$, the MnO_6 octahedra are elongated along one O–Mn–O direction (Mn–O bond length of 2.25 Å), the bond lengths in the plane perpendicular to this direction being 1.89 and 1.95 Å; all O–Mn–O angles are conserved.[17]

Due to the presence of an inversion center in the crystal structure, $TbMnO_3$ is paraelectric at room temperature. Upon lowering the temperature, $TbMnO_3$ undergoes three magnetic phase transitions. The first two are related to spin ordering of the Mn^{3+} ions; the third is related to the Tb^{3+} ions. An A-type antiferromagnetic order sets in at $T_{N_1} \approx 41$ K as an incommensurate sinusoidal order; then, at $T_{N_2} \approx 28$ K, a transversally modulated spiral structure appears and gives birth to a ferroelectric polarization along the **c** axis;[4,6] finally, at ≈7 K, the magnetic moments of the Tb^{3+} ions order antiferromagnetically along the **a** axis.[5,18]

Here, we present high-resolution resonant inelastic X-ray scattering (RIXS) measurements on $TbMnO_3$ performed with soft X-rays at the Mn L_3 and O K edges. RIXS is ideally suited for observing neutral low-energy excitations[19] and charge transfer (CT) between a transition metal and a ligand. The dipole selection rules in both the excitation and the relaxation channels make RIXS uniquely adapted to measuring d–d excitations. Hence, importantly here, it provides a precise means of determining the CF by confronting CF multiplet calculations with experimental data.

Experimental conditions are reported in Sec. II. Section III introduces the framework of the CF multiplet calculations for both XAS and RIXS. The comparison between calculations and measurements is given in Sec. IV, followed by a more general discussion (Sec. V). Conclusions are drawn in Sec. VI.

II. EXPERIMENTAL

$TbMnO_3$ single crystals were grown in an Ar atmosphere using the floating zone technique.[20] The crystalline structure of the sample was checked by X-ray diffraction and its orientation determined from Laue X-ray diffraction patterns. The sample was bonded to a holder using a conductive epoxy resin such that its surface normal was oriented parallel to the (0 0 1) plane. The surface of the sample was scraped with a diamond file in the load-lock chamber under a pressure of 2×10^{-7} mbar and immediately transferred to the analysis chamber under a pressure lower than 5×10^{-9} mbar. As the sample is scraped in a vertical position, the presence of randomly oriented crystallites at the surface that might contribute to the XAS/RIXS signals is unlikely.

The experiments were carried out at the SEXTANTS beamline[21] of Synchrotron SOLEIL (France). A He flow cryostat was used to lower the sample temperature. XAS spectra were recorded in total electron yield (TEY) mode by measuring the sample drain current. The RIXS measurements were performed with the AERHA spectrometer.[22] The beam, tuned to a specific resonance with an energy $h\nu_{in}$, impinged on the sample at 25° grazing incidence. The energy distribution of the scattered photons, $h\nu_{out}$, was analyzed using a 1800 lines/mm diffraction grating and recorded with a charge-coupled device cooled to –110 °C. Thanks to the specific design of the AERHA spectrometer, the energy resolution can be varied to get a satisfactory compromise between resolving power and counting rate. In the present experiment, the overall energy resolution of the RIXS data was 170 meV at the Mn $2p_{3/2}$–$3d$ resonance (L_3 edge ∼640 eV) and 140 meV at the O $1s$–$2p$ threshold (K edge ∼530 eV). The values of the beamline slits were such that $h\nu_{in}$ contributed a broadening of 140 meV at Mn L_3 and 100 meV at O K edges.

III. XAS AND RIXS CALCULATIONS

Semi-empirical CF multiplet calculations based on the Cowan–Butler–Thole code[23,24] were performed to match both the experimental Mn $L_{3,2}$ XAS and L_3 RIXS spectra with the *same* set of parameters. A detailed account of the methodology used in the present calculations is given in Ref. 25. CT effects were not taken into account in order to reduce the number of parameters involved. In the vicinity of the $L_{3,2}$ XAS white lines, the spectral features are only slightly affected by CT effects.[26] In the case of the L_3 RIXS spectra, the inclusion of CT shifts spectral weight to higher transferred energies, ($h\nu_{in} - h\nu_{out}$), and gives rise to CT spectral features, but *does not* alter the position of the CF multiplets.[25] A reduction factor of 65% is applied to the *ab initio* Hartree–Fock values of the direct (F^k) and exchange (G^k) Slater–Condon integrals to take into account the expansion of the electron cloud in the solid compared to the atomic distribution. The computed spectra were broadened by the intrinsic and experimental effects. The XAS final state has a Lorentzian broadening determined by the $2p$ core-hole lifetime: ≈0.20 eV and ≈0.32 eV for Mn $2p_{3/2}$ (L_3) and $2p_{1/2}$ (L_2), respectively.[27] For RIXS, the values given in Sec. II for the resolution of the beamline and of the AERHA spectrometer were taken into account as a Gaussian broadening.

Within the plane lying perpendicular to the elongated axis, there are small Mn–O bond length differences (see Sec. I), which we neglect in the following analysis, i.e., we simply assume that the distortion lowers the symmetry of the Mn local environment from O_h to D_{4h}. The atomic matrix elements are branched[28–30] from the spherical symmetry corresponding to the atomic situation to the D_{4h} symmetry relevant to the local environment of the atom involved in the process. Writing the in-plane and the out-of-plane Mn–O distances as $a^\star$ and $b^\star$, respectively, the CF acting on Mn sites can be parametrized using Dq, Ds, and Dt as follows:[31] $Dq(u) = (1/6)ze\overline{r^4}/u^5$ ($u = a^\star$ or $b^\star$), $Ds = Cp(a^\star) - Cp(b^\star)$, where $Cp(u) = (2/7)ze\overline{r^2}/u^3$, and $Dt = (4/7)[Dq(a^\star) - Dq(b^\star)]$. Here, ze represents the charge of the ligand and $\overline{r^n}$ is the mean n^{th} power of the electron radial distribution of the 3d transition-metal ion. These parameters are related to the CF parameters used by Butler[25,28] as: $Dq = [1/(6\sqrt{30})]X_{400} - [7/(30\sqrt{42})]X_{420}$, $Ds = -(1/\sqrt{70})X_{220}$, and $Dt = -[2/(5\sqrt{42})]\,X_{420}$.

In the XAS simulations (see below the comparison with the experiment), the orientation of the electric vector of the linearly polarized light relative to the tilts of the C_4 axis of the MnO_6 octahedra is fully taken into account. State-of-the-art RIXS calculations were performed to obtain the isotropic response of the system. The implementation of anisotropic aspects in RIXS calculations is presently under development.[32] We note, however, that the CF parameters extracted from our simulations are reliable because the *energies* of the Mn d–d excitations are determined by the local D_{4h} symmetry of the Mn^{3+} ions, whatever the orientation of the octahedra to which they belong.

IV. EXPERIMENTAL AND COMPUTATIONAL RESULTS

The Mn $L_{3,2}$ XAS spectra of $TbMnO_3$ recorded at room temperature are shown in Fig. 2. According to the orientation of the crystallographic axes relative to the sample position [see Fig. 1(c)], at normal incidence, linear horizontal (LH) and linear vertical (LV) polarizations correspond to $(\mathbf{q}_{in} \perp \mathbf{a}, \mathbf{E} \parallel \mathbf{b}, \mathbf{q}_{in} \parallel \mathbf{c})$ and $(\mathbf{E} \parallel \mathbf{a}, \mathbf{q}_{in} \perp \mathbf{b}, \mathbf{q}_{in} \parallel \mathbf{c})$, respectively, where $\mathbf{q}_{in}$ is the wave vector of the incident beam with electric field $\mathbf{E}$. When the sample surface is oriented to 25° grazing incidence, the use of LH polarization delivers a configuration close to $(\mathbf{q}_{in} \perp \mathbf{a}, \mathbf{q}_{in} \parallel \mathbf{b}, \mathbf{E} \parallel \mathbf{c})$, while for LV polarization, the orientation can be described as $(\mathbf{E} \parallel \mathbf{a}, \mathbf{q}_{in} \parallel \mathbf{b}, \mathbf{q}_{in} \perp \mathbf{c})$. As these measurements were made in TEY mode, they are expected to be sensitive to the quality of the surface. It is seen that the spectra are hardly affected by the change in incidence angle of the incoming light indicating that contribution from surface contamination is negligible. This reinforces the reliability of far less surface sensitive RIXS data as compared to TEY. At low temperatures (≈25 K), the sample conductivity is substantially reduced, thus preventing measurements using the sample drain current.

All XAS spectra display a pronounced shoulder (denoted by a in Fig. 2) initiating a white line with three well-resolved maxima (b, c, and d) followed by a shoulder (e). Our spectra show only very slight polarization dependence, at variance with XAS TEY data previously reported for a single crystal[33] or thin films[34] with the same composition. However, our data are in excellent agreement with more recent XAS spectra.[35]

Mn L_3 RIXS spectra were recorded, with incoming LH polarized light (π polarization), at room temperature and at 25 K for all incoming photon energies $h\nu_{in}$ defined in Fig. 2. As the data show very similar spectral features for both temperatures, only the 25 K data are presented in Fig. 3. The main features indicated with dashed lines in Fig. 3 correspond to energy loss values of 1.6, 2.4, and 3.0 eV. As they appear at constant ($h\nu_{in} - h\nu_{out}$), we attribute them to *on-site* Mn d–d excitations. Broader features are also observed at higher energy, e.g., between ≈4 and 10 eV in the RIXS spectrum recorded at $h\nu_{in} = 640.0$ eV (see a in Fig. 2). As the energy loss associated with these features increases in the same way as the incoming photon energy, they are related either to CT excitations corresponding to $3d^4 \rightarrow 3d^5\underline{L}^{-1}$, where $\underline{L}$ denotes an oxygen ligand around the Mn site, or to fluorescence (or a combination of both).[36]

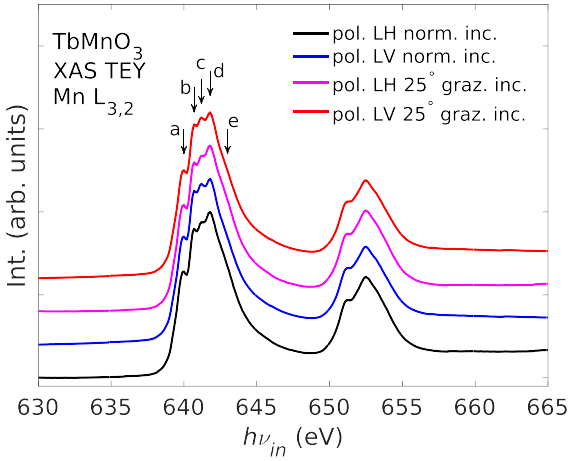

FIG. 2. Mn $L_{3,2}$ XAS for $TbMnO_3$ recorded at room temperature with photons having linear horizontal (LH) and linear vertical (LV) polarizations, as well as in two geometries: at normal incidence and 25° grazing incidence of the beam relative to the sample surface.

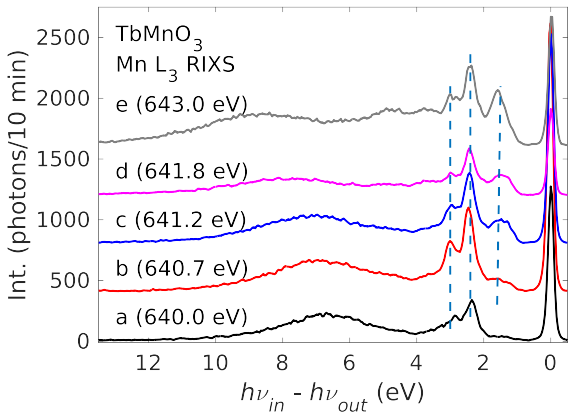

FIG. 3. Mn L_3 RIXS for $TbMnO_3$ recorded at 25 K. The letters refer to the Mn $L_{3,2}$ XAS spectrum (Fig. 2) and indicate the incident photon energies used in the RIXS measurements. The abscissa is given as the energy ($h\nu_{in} - h\nu_{out}$) lost by the photons in the inelastic scattering process. Vertical dashed lines are guide to the eye for the main groups of losses.

It is interesting to note that optical spectroscopy of the parent rare-earth manganites has outlined the difficulty of classifying these compounds either as CT or as Mott–Hubbard insulators[37] and has revealed the presence of an inter-site (Mn 3*d*–Mn' 3*d*) excitation.[38] RIXS measurements at the Mn *K* edge, obtained with an overall energy resolution of ~ 1 eV, have shown a broad energy-loss feature at ≈ 2.9 eV that has been interpreted on the basis of first principles band structure calculations to a mixture of on-site (Mn 3*d*–Mn 3*d*) and inter-site (Mn 3*d*–Mn' 3*d*) excitations.[39] Considering only on-site *d*–*d* excitations delivers an adequate interpretation of the Mn L_3 RIXS measurements in the present contribution.

Because of the overlap between Mn 3*d* states and O 2*p* ligand states, we expect to observe the signature of Mn *d*–*d* excitations when performing RIXS measurements at the O *K* resonance. This possibility was first identified in $CuGeO_3$[40] and confirmed in the case of NiO[41,42] and La_2CuO_4.[43] Our O *K* XAS and RIXS results for $TbMnO_3$ are presented in Fig. 4 (as before, the O *K* RIXS data recorded at room temperature and at 25 K have similar shape and only the low temperature data are shown in this figure). The XAS spectrum probes unoccupied O 2*p* states and displays four main structures for incident photon energies $h\nu_{in}$ of 529.4, 530.2, 533.6, and 535.8 eV. The RIXS spectra show two separable contributions. For incoming photon energies $528.4 \leq h\nu_{in} \leq 530.2$ eV, a Raman-like spectral feature is found at 2.4 eV constant energy-loss. Based on the Mn L_3 RIXS, it is attributed to a Mn *d*–*d* excitation by analogy with what has been reported in previous O *K* RIXS studies.[40–43] A second contribution arises from the resonant $2p \rightarrow 1s$ fluorescence-like emission (shown as vertical bars in the bottom panel of Fig. 4), at constant $h\nu_{out}$ photon energies, coming from the occupied O 2*p* density of states (DOS). The latter contribution sets in already when the incoming photon energy is tuned 1 eV below the first white line. The spectral weight of the resonant emission increases with the energy of the incoming photons and largely dominates the RIXS spectra, as expected. We note that the Raman-like contribution showing up at 2.4 eV energy loss can be conveniently disentangled, provided that a sufficient number of incident energies are used for recording the RIXS spectra.

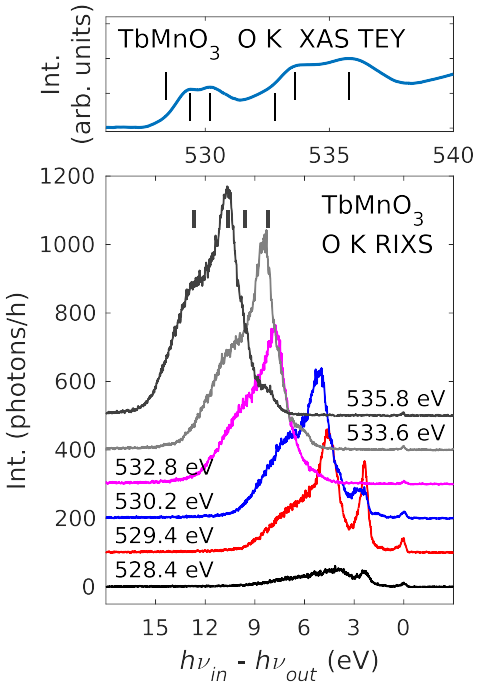

FIG. 4. XAS (top panel) and RIXS spectra (bottom panel) recorded for $TbMnO_3$ at O *K* edge. Vertical lines in the XAS spectrum (taken at room temperature) indicate the incoming photon energies used to record the RIXS spectra recorded at 25 K, the values being listed in the bottom panel. Short vertical bars in the lower panel are a guide to the eye for the main fluorescence-like bands recorded with $h\nu_{in} = 535.8$ eV.

In order to obtain a parametric description of the CF acting on the Mn^{3+} sites, we simulated the Mn $L_{3,2}$ XAS spectrum and the Mn L_3 RIXS spectra using the same set of *Dq*, *Ds*, and *Dt* values. The simulated spectra are shown in Fig. 5 along with the experimental results (for XAS, the case of LH polarized light at normal incidence is shown). We worked with a Racah parameter $B = 800\,\mathrm{cm}^{-1}$, given by *ab initio* Hartree–Fock calculations after reduction of the Slater–Condon parameters (see Sec. III). The best *Dq*, *Ds*, and *Dt* set was obtained after examination of a large number of combinations, as described in Ref. 44. As CT was not included in the calculations, we privileged agreement between predicted and experimental peak positions for RIXS and the main maxima of the L_3 XAS shape. The values obtained were as follows: $10Dq = 1.6$ eV, $Ds = 0.31$ eV, and $Dt = 0.06$ eV. Conserving these values for the core-hole state assumes that the presence of the core-hole potential does

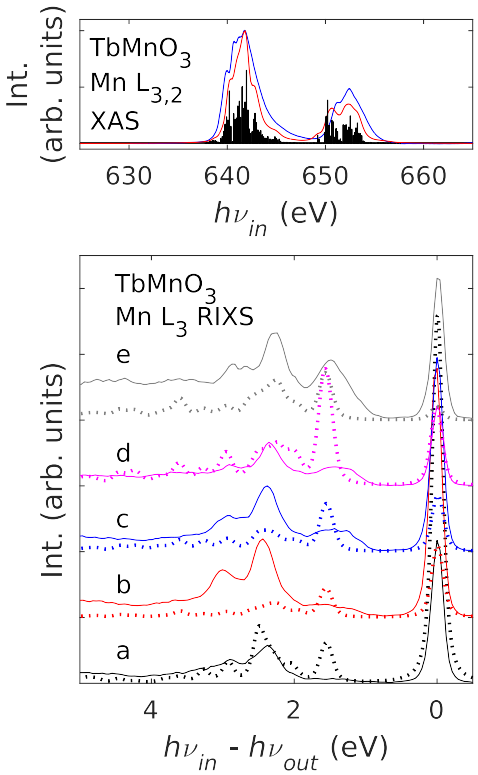

FIG. 5. Simulated and measured XAS and RIXS spectra of $TbMnO_3$ at Mn $L_{3,2}$ edges. Top panel: XAS (the non-resonant contribution has been subtracted to make the comparison with the simulation easier). XAS measured and calculated spectra are shown for LH incoming light at normal incidence. Bottom panel: the energies a–e used to record the RIXS spectra are the same as in Fig. 2; the continuous and dashed lines are the experimental and calculated spectra, respectively.

not alter the CF strength. This assumption, widely used in previous studies,[25] makes it possible to work with a reasonable number of CF parameters. The simulated results are in very good agreement with the measured spectra and allow, according to Ref. 44, the following identifications to be made: the peak located at 1.6 eV energy loss is due to transitions from the $^5B_{1g}$ ground state to a manifold of $^5A_{1g}+^5B_{2g}+^3E_g$ excited states; the peak at 2.4 eV and that at 3.0 eV can be attributed to $^5B_{1g}\rightarrow{}^5E_g+^3A_{1g}+^3A_{2g}+^1A_{1g}$ and $^5B_{1g}\rightarrow{}^3B_{1g}+^1B_{1g}+^3E_g+^3B_{2g}$ orbital excitations, respectively.

V. DISCUSSION

The CF approach has generally demonstrated its ability to provide a good understanding of the energy levels of 3*d* and 4*f* cations in a symmetrical environment of anions. However, the quantitative agreement of the theoretical predictions (point charge model, angular overlap model) with experiments is poor, even when covalent bonding is included within the framework of the ligand field theory. The main difficulties in the calculation of CF parameters arise from the moments $\overline{r^2}$ and $\overline{r^4}$ of the radial distribution. Typically, the experimental $\overline{r^2}/\overline{r^4}$ ratio is several times lower than the values calculated for free 3*d* ions (see Ref. 45 and references therein). A further complication is added by the way the ligands are described; the spatial extension of the O 2*p* states makes it difficult to handle the ligand in terms of point charges with an effective charge *ze* (see, e.g., Ref. 31) and demands for a more sophisticated approach. Efforts to take into account both electrostatic and hybridization effects continue to be made to get better predictions, as they are essential for a quantitative modelization of ferroelectric materials. Such a goal requires an accurate determination of phenomenological CF parameters.[46]

Some insight into the effect of CF on the unoccupied electronic states can be obtained from the O *K* edge spectra (Fig. 4). Electric dipole $1s\leftrightarrow 2p$ transitions bring out the unoccupied O 2*p* partial DOS in the XAS data as well as the occupied DOS in the fluorescence-like contribution to the RIXS data. Following the analysis of various Mn compounds where the transition metal is found in a distorted octahedral environment,[47–51] the O *K* XAS feature at 529.4 eV can be tentatively assigned to O 2*p* states hybridized with Mn $(3z^2-r^2)$ from the e_g branch and the 530.2 eV energy loss can be linked to O 2*p* states hybridized mainly with Mn (x^2-y^2) states. The energy separation $\Delta=0.8$ eV measured in O *K* XAS is expected to be different from $\Delta_{e_g}=\varepsilon_{(x^2-y^2)}-\varepsilon_{(3z^2-r^2)}$. The difference $\delta=\Delta-\Delta_{e_g}$ can be explained by the core-hole binding energy difference for oxygen atoms situated in-plane (planar positions) and out-of-plane (apical positions along the C_4 symmetry axis). According to the present parametrization, $\Delta_{e_g}=4Ds+5Dt=1.54$ eV, therefore leading to an anomalous core-hole binding energy difference $\delta\approx-0.74$ eV. This observation clearly indicates that such simple models to extract the CF splitting from the O *K* XAS can be applied to manganites only in particular cases. The hybridization between occupied O 2*p* and Mn 3*d* states can be observed from the O *K* fluorescence-like resonant emission: the spectra show four main bands, marked with short vertical bars in the RIXS spectra of Fig. 4. The relative intensity of the bands has a strong $h\nu_{in}$ dependence. The O 2*p* partial DOS calculations presented in Ref. 33 display a relatively good agreement with the unoccupied O 2*p* states obtained with the present O *K* XAS. On the other hand, agreement between occupied O 2*p* states revealed by O *K* resonant emission and calculations in Ref. 33 is rather poor.

Our approach involving the Mn L_3 edge relies only on symmetry considerations and provides an explicit way for characterizing the tetragonal distortion of MnO_6 octahedra in $TbMnO_3$. The CF parameters are the best values matching the D_{4h} environment. In other words, the parameters *Dq*, *Ds*, and *Dt* can be used without the need for renormalization accounting for the surrounding of the Mn^{3+} ion and are to be regarded as pure numerical parameters, including both symmetry effects and Mn 3*d*–O 2*p* hybridization. Recently, an attempt to better understand the contributions of electrostatic and hybridization effects has been presented,[52] based on Wannier functions. In particular, the $TbMO_3$ series, where M is a 3*d* transition-metal ion with a formal number n_d of *d* electrons, was studied; an hypothetical tetragonally distorted perovskite structure (space group *P*4/*mmm*; $a=3.86$ Å and $c/a=1.1$) was assumed whatever M. For $n_d=4$ (M = Mn), it is predicted that the hybridization should lead to an inversion of the energy levels corresponding to the (*xy*) and (*xz*, *yz*) states that originate from the octahedral t_{2g} state, i.e., the energy difference $\Delta_{t_{2g}}=\varepsilon_{(xy)}-\varepsilon_{(xz,yz)}$ was found negative in Ref. 52. The energy separation Δ_{e_g} between the (x^2-y^2) and $(3z^2-r^2)$ states remains positive in the model as expected from simple electrostatic considerations based on the shape of the *d* orbitals. This is not supported by our findings. Within the (*Ds*, *Dt*) parametrization, the energy differences are given by (see, e.g., Ref. 31): $\Delta_{t_{2g}}=3Ds-5Dt$ and $\Delta_{e_g}=4Ds+5Dt$. These expressions, derived from symmetry considerations, adopt a pure numerical parametrization, as already mentioned. According to our results, it is found that $\Delta_{t_{2g}}=0.63\,\text{eV}\,(>0)$ and $\Delta_{e_g}=1.54\,\text{eV}\,(>0)$. We note that the parameters obtained here lead to a separation of only 0.06 eV between the (*xy*) state from the t_{2g} branch and the $(3z^2-r^2)$ state from the e_g branch, clearly opening the possibility for state mixture. The magnitude of the Jahn–Teller splitting (>300 meV) of the Mn^{3+} 3*d* levels supports the dominant role attributed to Jahn–Teller effects in the orbital ordering in $TbMnO_3$.[12]

VI. CONCLUSIONS

Combining element specific RIXS and XAS measurements at the Mn $L_{3,2}$ edges with CF multiplet calculations provides accurate parameters for the description of tetragonal distortion of the Mn^{3+} environment in $TbMnO_3$. The present work represents a first step toward reliable calculations of the energies involved in ionic displacements which might enter the emergence of electric polarization in $TbMnO_3$ and are relevant to the description of the magnetic interactions in this compound.

ACKNOWLEDGMENTS

The authors thank R. Gaudemer for technical assistance. S.G.C., R.D., and J.-M.M. acknowledge the support of the

Agence Nationale de la Recherche (ANR), under Grant No. ANR-05-NANO-074 (HR-RXRS). Additional funding was provided by Synchrotron SOLEIL and UPMC. R.S. and H.D.Z. thank the support from NSF-DMR through Award No. DMR-1350002.

[1]D. I. Khomskii, *Transition Metal Compounds* (Cambridge University Press, Cambridge, 2014).
[2]S. Picozzi and C. Ederer, J. Phys.: Condens. Matter **21**, 303201 (2009).
[3]D. Khomskii, Physics **2**, 20 (2009).
[4]T. Kimura, T. Goto, H. Shintani, K. Ishizaka, T. Arima, and Y. Tokura, Nature **426**, 55 (2003).
[5]M. Kenzelmann, A. B. Harris, S. Jonas, C. Broholm, J. Schefer, S. B. Kim, C. L. Zhang, S.-W. Cheong, O. P. Vajk, and J. W. Lynn, Phys. Rev. Lett. **95**, 087206 (2005).
[6]T. Kimura, Annu. Rev. Mater. Res. **37**, 387 (2007).
[7]H. Katsura, N. Nagaosa, and A. V. Balatsky, Phys. Rev. Lett. **95**, 057205 (2005).
[8]M. Mostovoy, Phys. Rev. Lett. **96**, 067601 (2006).
[9]S. B. Wilkins, T. R. Forrest, T. A. W. Beale, S. R. Bland, H. C. Walker, D. Mannix, F. Yakhou, D. Prabhakaran, A. T. Boothroyd, J. P. Hill, P. D. Hatton, and D. F. McMorrow, Phys. Rev. Lett. **103**, 207602 (2009).
[10]H. C. Walker, F. Fabrizi, L. Paolasini, F. de Bergevin, J. Herrero-Martin, A. T. Boothroyd, D. Prabhakaran, and D. F. McMorrow, Science **333**, 1273 (2011).
[11]H. C. Walker, F. Fabrizi, L. Paolasini, F. de Bergevin, D. Prabhakaran, A. T. Boothroyd, and D. F. McMorrow, Phys. Rev. B **88**, 214415 (2013).
[12]A. Flesch, G. Zhang, E. Koch, and E. Pavarini, Phys. Rev. B **85**, 035124 (2012).
[13]X.-Y. Chen, L.-J. Chen, X.-B. Yang, Y.-J. Zhao, H.-C. Ding, and C.-G. Duan, J. Appl. Phys. **111**, 013901 (2012).
[14]A.-M. Haghiri-Gosnet and J.-P. Renard, J. Phys. D: Appl. Phys. **36**, R127 (2003).
[15]N. Hollmann, Z. Hu, T. Willers, L. Bohatý, P. Becker, A. Tanaka, H. H. Hsieh, H.-J. Lin, C. T. Chen, and L. H. Tjeng, Phys. Rev. B **82**, 184429 (2010).
[16]Y. Tokura and Y. Tomioka, J. Magn. Magn. Mater. **200**, 1 (1999).
[17]M. E. Bolívar Guarín, A. d M. Moreira, and N. Speziali, J. Appl. Cryst. **46**, 644 (2013).
[18]R. Kajimoto, H. Yoshizawa, H. Shintani, T. Kimura, and Y. Tokura, Phys. Rev. B **70**, 012401 (2004).
[19]L. J. P. Ament, M. van Veenendaal, T. P. Devereaux, J. P. Hill, and J. van den Brink, Rev. Mod. Phys. **83**, 705 (2011).
[20]T. Zou, Z. Dun, H. Cao, M. Zhu, H. Zhou, and X. Ke, J. Appl. Phys. **116**, 104101 (2014).
[21]M. Sacchi, N. Jaouen, H. Popescu, R. Gaudemer, J.-M. Tonnerre, S. G. Chiuzbăian, C. F. Hague, A. Delmotte, J. M. Dubuisson, G. Cauchon, B. Lagarde, and F. Polack, J. Phys.: Conf. Ser. **425**, 072018 (2013).
[22]S. G. Chiuzbăian, C. F. Hague, A. Avila, R. Delaunay, N. Jaouen, M. Sacchi, F. Polack, M. Thomasset, B. Lagarde, A. Nicolaou, S. Brignolo, C. Baumier, J. Lüning, and J.-M. Mariot, Rev. Sci. Instrum. **85**, 043108 (2014).
[23]R. D. Cowan, *The Theory of Atomic Spectra and Structure*, Los Alamos Series in Basic and Applied Sciences Vol. 3 (University of California Press, Berkeley, 1981).
[24]B. T. Thole, G. van der Laan, and P. H. Butler, Chem. Phys. Lett. **149**, 295 (1988).
[25]F. de Groot and A. Kotani, *Core Level Spectroscopy of Solids*, Advances in Condensed Matter Science (CRC Press, Boca Raton, FL, 2008).
[26]H. Ikeno, F. M. F. de Groot, E. Stavitski, and I. Tanaka, J. Phys.: Condens. Matter **21**, 104208 (2009).
[27]"Core-hole lifetime broadenings," in *Unoccupied Electronic States*, Topics in Applied Physics Vol. 69, edited by J. C. Fuggle and J. E. Inglesfield (Springer Verlag, Berlin, Heidelberg, New York, 1992), p. 347, Appendix B.
[28]P. H. Butler, *Point Group Symmetry, Applications, Methods and Tables* (Plenum Press, New York, 1981).
[29]B. G. Searle and P. H. Butler, J. Phys. A: Math. Gen. **21**, 1977 (1988).
[30]H. J. Ross, L. F. McAven, K. Shinagawa, and P. H. Butler, J. Comput. Phys. **128**, 331 (1996).
[31]B. N. Figgis and M. A. Hitchman, *Ligand Field Theory and Its Applications*, Special Topics in Inorganic Chemistry (Wiley-VCH, New York, 2000).
[32]A. Juhin, C. Brouder, and F. Groot, Cent. Eur. J. Phys. **12**, 323 (2014).
[33]J. M. Chen, J. M. Lee, C. K. Chen, T. L. Chou, K. T. Lu, S. C. Haw, K. S. Liang, C. T. Chen, H. T. Jeng, S. W. Huang, T. J. Yang, C. C. Shen, R. S. Liu, J. Y. Lin, and Z. Hu, Appl. Phys. Lett. **94**, 044105 (2009).
[34]K. H. Wu, I. C. Gou, C. W. Luo, T. M. Uen, J.-Y. Lin, J. Y. Juang, C. K. Chen, J. M. Lee, and J. M. Chen, Thin Solid Films **518**, 2275 (2010).
[35]H. Jang, J.-S. Lee, K.-T. Ko, W.-S. Noh, T. Y. Koo, J.-Y. Kim, K.-B. Lee, J.-H. Park, C. L. Zhang, S. B. Kim, and S.-W. Cheong, Phys. Rev. Lett. **106**, 047203 (2011).
[36]G. Ghiringhelli, M. Matsubara, C. Dallera, F. Fracassi, R. Gusmeroli, A. Piazzalunga, A. Tagliaferri, N. B. Brookes, A. Kotani, and L. Braicovich, J. Phys.: Condens. Matter **17**, 5397 (2005).
[37]A. S. Moskvin, A. A. Makhnev, L. V. Nomerovannaya, N. N. Loshkareva, and A. M. Balbashov, Phys. Rev. B **82**, 035106 (2010).
[38]M. W. Kim, S. J. Moon, J. H. Jung, J. Yu, S. Parashar, P. Murugavel, J. H. Lee, and T. W. Noh, Phys. Rev. Lett. **96**, 247205 (2006).
[39]J. M. Chen, J. M. Lee, S. W. Huang, K. T. Lu, H. T. Jeng, C. K. Chen, S. C. Haw, T. L. Chou, S. A. Chen, N. Hiraoka, H. Ishii, K. D. Tsuei, and T. J. Yang, Phys. Rev. B **82**, 094442 (2010).
[40]L.-C. Duda, J. Downes, C. McGuinness, T. Schmitt, A. Augustsson, K. E. Smith, G. Dhalenne, and A. Revcolevschi, Phys. Rev. B **61**, 4186 (2000).
[41]L.-C. Duda, T. Schmitt, M. Magnuson, J. Forsberg, A. Olsson, J. Nordgren, K. Okada, and A. Kotani, Phys. Rev. Lett. **96**, 067402 (2006).
[42]K. Okada and A. Kotani, J. Phys. Soc. Jpn. **72**, 797 (2003).
[43]V. Bisogni, L. Simonelli, L. J. P. Ament, F. Forte, M. Moretti Sala, M. Minola, S. Huotari, J. van den Brink, G. Ghiringhelli, N. B. Brookes, and L. Braicovich, Phys. Rev. B **85**, 214527 (2012).
[44]E. König and S. Kremer, *Ligand Field Energy Diagrams* (Springer Science+Business Media, New York, 2013), p. 179.
[45]M. Pollet and A. Artemenko, J. Phys. Chem. A **117**, 6536 (2013).
[46]N. M. Avram and M. G. Brik, *Optical Properties of 3d-Ions in Crystals: Spectroscopy and Crystal Field Analysis* (Tsinghua University Press and Springer-Verlag, Beijing, Berlin, 2013).
[47]J.-H. Park, C. T. Chen, S.-W. Cheong, W. Bao, G. Meigs, V. Chakarian, and Y. U. Idzerda, Phys. Rev. Lett. **76**, 4215 (1996).
[48]J.-H. Park, T. Kimura, and Y. Tokura, Phys. Rev. B **58**, R13330 (1998).
[49]M. Merz, P. Reutler, B. Büchner, D. Arena, J. Dvorak, Y. U. Idzerda, S. Tokumitsu, and S. Schuppler, Eur. Phys. J. B **51**, 315 (2006).
[50]V. Capogrosso, M. Malvestuto, I. P. Handayani, P. H. M. van Loosdrecht, A. A. Nugroho, E. Magnano, and F. Parmigiani, Phys. Rev. B **87**, 155118 (2013).
[51]R. U. Chandrasena, W. Yang, Q. Lei, M. U. Delgado-Jaime, K. D. Wijesekara, M. Golalikhani, B. A. Davidson, E. Arenholz, K. Kobayashi, M. Kobata, F. M. F. de Groot, U. Aschauer, N. A. Spaldin, X. Xi, and A. X. Gray, Nano Lett. **17**, 794 (2017).
[52]A. Scaramucci, J. Ammann, N. A. Spaldin, and C. Ederer, J. Phys.: Condens. Matter **27**, 175503 (2015).

Chapter 2

article $DyMnO_3$

Electronic structure of $DyMnO_3$ probed by resonant inelastic x-ray scattering at the Mn L_3 and O K edges

Jiatai Feng[1], Amélie Juhin[2], Romain Jarrier[1,3], Renaud Delaunay[1,3], Haidong Zhou[4], Jean-Michel Mariot[1,3] and Sorin G Chiuzbăian[1,3]‡

[1] Sorbonne Universités, UPMC Univ Paris 06, CNRS, Laboratoire de Chimie Physique–Matière et Rayonnement (UMR 7614), 4 place Jussieu, 75252 Paris Cedex 05, France

[2] Sorbonne Universités, UPMC Univ Paris 06, CNRS, IRD, MNHN, Institut de Minéralogie, de Physique des Matériaux et de Cosmochimie (UMR 7590), 4 place Jussieu, 75252 Paris Cedex 05, France

[3] Synchrotron SOLEIL, L'Orme des Merisiers, Saint-Aubin, BP 48, 91192 Gif-sur-Yvette, France

[4] University of Tennessee, Department of Physics and Astronomy, Experimental Condensed Matter Physics, 407A Nielsen Physics Building, Knoxville, TN 37996-1200, United States

E-mail: gheorghe.chiuzbaian@upmc.fr

Abstract.

X-ray absorption spectra and resonant inelastic x-ray scattering measurements recorded at the Mn $L_{3,2}$ and O K edges (at room temperature and 25 K) on the $DyMnO_3$ multiferroic are presented. The data are interpreted using crystal field multiplet calculations which provide a solid ground for a quantitative description of the Mn^{3+} environment in terms of a D_{4h} symmetry. The crystal field parameters obtained are $10Dq = 1.6$ eV, $Dt = 0.06$ eV and $Ds = 0.36$ eV. The results are compared with those determined for the $TbMnO_3$ isostructural compound.

PACS numbers: 78.70.Ck, 78.70.Dm, 78.70.En, 75.85.+t, 75.10.Dg

Submitted to: *J. Phys.: Condens. Matter*

Keywords: $TbMnO_3$ and $DyMnO_3$, multiferroics, resonant inelastic x-ray scattering, low-energy excitations, crystal field.

‡ Corresponding author.

1. Introduction

Perovskite rare-earth manganites $R\mathrm{MnO_3}$ (R = La, ..., Lu) exhibit complex physical properties arising from the subtle interplay of charge, spin, orbital and lattice degrees of freedom [1]. The crystallographic structure of these manganites deviates from the ideal cubic $R^{+3}\mathrm{Mn}^{+3}\mathrm{O}_3^{2-}$ perovskite structure (space group $Pm\overline{3}m$) that can be described as a cubic close packed lattice of R^{3+} and O^{2-} ions, the Mn^{+3} ions occupying the octahedral holes created by the O^{2-} ions; so the structure has a three dimensional net of corner sharing $\mathrm{MnO_6}$ octahedra with R^{3+} ions located at the twelve-fold voids in the middle of the cube made by eight $\mathrm{MnO_6}$ octahedra. The deviation from the ideal structure has two origins: i) a departure of the cubic lattice constant a from its ideal value $\sqrt{2}(r_R + r_\mathrm{O}) = 2(r_\mathrm{Mn} + r_\mathrm{O})$ determined by the radii of the ions involved; ii) the $3d^4$ ($t_{2g}^3 e_g^1$) electronic configuration of the Mn^{3+} ion which makes it Jahn–Teller active, which means that the $\mathrm{MnO_6}$ octahedra are distorted. In the case where R = Dy or Tb, there is a strong mismatch between the volume of the R^{3+} ion and that of the void between the $\mathrm{MnO_6}$ octahedra, which leads to a rotation of these octahedra around the high-symmetry axes and some of distortion (symmetry lowering) of the octahedra as well [2]. Since every O^{2-} ion is at the apex of two octahedra, the rotations propagate cooperatively in the lattice, which results in the so-called $\mathrm{GdFeO_3}$ distortion and an orthorhombically distorted perovskite structure (space group $Pbnm$) [3].

The magnetic phase diagram of the $R\mathrm{MnO_3}$ compounds (even undoped) has been found very rich and depending on radius of the R^{3+} ions [4, 5]. The cases R = Tb and Dy, i.e. that of medium-sized rare-earth ions, are of particular interest because, upon temperature lowering from room temperature, both corresponding compounds first exhibit a transition from an orbitally-ordered paramagnetic phase [6] to an incommensurate sinusoidal antiferromagnetic order of the Mn moments (at $\approx 41\,\mathrm{K}$ and $\approx 39\,\mathrm{K}$, for R = Tb and Dy, respectively), followed by a transition to a commensurate cycloidal ordering accompanied by the appearance of an electric polarization (at $\approx 28\,\mathrm{K}$ for R = Tb and $\approx 19\,\mathrm{K}$ for R = Dy) [4, 7, 8]. Both transitions are connected to spin ordering of the Mn^{3+} ions; additional transitions related to the $4f$ spins of the R^{3+} ions occur at $\approx 7\,\mathrm{K}$ for both compounds.

The concomitance of antiferromagnetism and ferroelectricity qualifies these compounds as (type II) multiferroic systems (see, e.g. references [9, 10]). Envisioned applications using the fact that an applied electric field can tune magnetic order and *vice versa* and the challenge of understanding the cross-coupling phenomena involved has boosted the field of multiferroic physics within the past decade [11]. Several mechanisms have been proposed to explain the origin of multiferroicity in these compounds. One is the inverse Dzyaloshinskii–Moriya interaction [12] in which the non-alignment of neighboring spins induces a force displacing relatively ions with opposite charge, which creates an electric polarization and evidence for these at the femtometre scale displacements has been given recently [13, 14]. It has also been proposed that, in these cycloidal spin spirals systems, the spin-orbit coupling could distort the electronic cloud

at an ionic core and be at the origin of an electric dipole without the need of any atomic displacement [15].

As a consequence from the above considerations, the interaction between the charge and the spin degrees of freedom of the electrons at the Mn site is central to the magneto-electric coupling. Thus getting information on the Mn local electronic excitations is of primary importance.

Here we present results we have obtained on such excitations from resonant inelastic x-ray scattering (RIXS) experiments performed at the Mn $L_{3,2}$ threshold and O K in $DyMnO_3$. In RIXS the sample is shined by monochromatic light ($h\nu_{\rm in}$) tuned to a given core level binding energy of one of the sample atoms and the spectroscopy of the scattered light ($h\nu_{\rm out}$) is performed. The energy difference ($h\nu_{\rm in}-h\nu_{\rm out}$) allows a mapping of the excitations of this specific atom of the system. It should be underlined that, as on simple grounds, the scattering process can be viewed as a dipolar photoabsorption from the ground state of the system to an intermediate state followed by a dipolar radiative decay from this intermediate state to a low lying excited state of the system, the parity in conserved is the whole scattering process. The spin-orbit coupling in the intermediate core-hole state opens the access to final states with a change in spin multiplicity.

This means that, contrary to what can be probed by UV-vis spectroscopy, intra-band d–d excitations can be revealed without restrictions from selection rules governing optical spectroscopies; charge transfer excitations can be probed as well. In addition, as RIXS is "an x-ray in – x-ray out" experiment the data collected are not affected by surface effects and reveal bulk properties. A consistent simulation of both Mn $L_{3,2}$ XAS and RIXS spectra is made within the crystal field multiplet approach. This approach allows to characterize the crystal field acting on the Mn^{3+} and thus bring information useful to understand better the ferroelectricity in these manganites.

Experimental conditions are given in section 2, the essential ingredients of the CF multiplets calculations for mapping both XAS and RIXS spectra are presented in section 3. This is followed by a comparison between the experimental and theoretical results, and by a more general discussion where a confrontation between the results for $DyMnO_3$ and previous $TbMnO_3$ data is made (section 4). Specific $TbMnO_3$ parameters are listed in the present contribution in order to facilitate the comparison. Conclusions are drawn in section 5.

2. Experiments

Orthorhombic $DyMnO_3$ single crystals were grown under an Ar atmosphere using the floating zone technique [16]. X-ray diffraction and Laue patterns were used to check the crystal structure and orient the normal to the sample surface parallel to (0 0 1). The samples were glued on a copper holder using a conductive epoxy resin compatible with ultra-high vacuum conditions. The samples were scraped with a diamond file under a pressure of 2×10^{-7} mbar in the load-lock chamber attached to the spectrometer and then immediately transferred into the main chamber where the pressure was lower than

5×10^{-10} mbar during all measurements.

The data were acquired at the SEXTANTS beamline [17] of Synchrotron SOLEIL (France). The XAS spectra were recorded in the total electron yield mode. The RIXS measurements were made with the AREHA spectrometer used with its 1800 lines/mm diffraction grating [18]. The RIXS spectra were acquired using linear horizontal (LH) polarization of the incoming light making a 20° angle with the normal to the sample surface, the scattered radiation being at 95° to the incident beam in the horizontal plane. A charge-coupled device cooled at −110 °C serves as detector. The selected incident energies for the RIXS measurements correspond to clear spectral features observed in the XAS spectra. The RIXS measurements were done at room temperature and at ≈ 25 K; the XAS spectra were only measured at room temperature, the semiconducting state of the samples at low temperature preventing the use of the TEY mode. The RIXS total energy resolution was 180 meV at the Mn L_3 resonance; it was 140 meV at the O K resonance, as determined by the full width at half maximum of the elastic peak.

3. Multiplet calculations for XAS and RIXS

The crystal field multiplet theory has proven to be very successful to the describe x-ray radiative processes in solids involving localized electrons as encountered in $3d$ transition metal compounds [19]. Essentially it describes how the degeneracy of the atomic states is left in the solid under the influence of the electric field created by the ligands (L) surrounding this atom. Thus the model relies on the branching from the atomic spherical symmetry to that characteristic of the site involved for the calculation at transition matrix elements involved in either the photoaborption (XAS) or resonant inelastic scattering (RIXS). In this work the calculations of the XAS and RIXS spectra were done using the Cowan–Butler–Thole code [20, 21]. Ligand to metal $3d^4 \rightarrow 3d^5\mathrm{L}^{-1}$ charge transfer effects were not taken into account. Although it somewhat hampers a close comparison of the simulated spectra with experiment to be made, it has the advantages of simplifying drastically the computational task and limiting the number of the parameters involved. It has also to be reminded that the position of the sharp features observed in the $L_{3,2}$ XAS/RIXS spectra of $3d$ transition metal compounds are not expected to be modified upon inclusion of charge transfer in the calculations [19,22].

According to high resolution neutron diffraction data [2], the environment of the Mn^{3+} ions slightly deviates from a D_{4h} symmetry (octahedron elongated along one direction) Mn–O bond lengths in the plane perpendicular to the Mn–O_2 elongation direction (for which the Mn–O_2 bond lengths are 2.222 Å and 2.224 Å for $TbMnO_3$ and $DyMnO_3$, respectively), i.e. ≈ 1.94 Å for Mn–O_1 and ≈ 1.90 Å for Mn–O_2 in both compounds (the O–Mn–O angles remain equal to 180°). Therefore we have adopted the D_{4h} symmetry (instead of D_{2h}) to describe the Mn^{3+} local environment in the optics of computation simplification and of minimization of the number of free parameters used to characterise the crystal field. Only three parameters (Dq, Ds and Dt) are needed in the D_{4h} case: $10Dq$ accounts basically for the energy splitting of the five-fold degenerated

Mn 3*d* orbitals into t_{2g} and e_g states due to the (quasi)octahedral (O_h) environment of the Mn^{3+} ion, Ds and Dt describing the symmetry lowering from O_h to D_{4h} [23].

Our calculations are based on Hartree–Fock values for the Salter–Condon integrals F^k and G^k that have been reduced by 65% to account for electron-electron interaction beyond the Hartree–Fock scheme, a value that has been found to be suitable for rare-earth manganites (see, e.g. reference [24]). In order to generate XAS simulated spectra to be confronted with experiment, the discrete intensity distributions resulting from the calculations were broadened by a Voigt profile that takes into account both the Lorentzian lifetime broadening of the core-hole (0.20 eV and 0.32 eV at the L_3 and L_2 edges, respectively [25]) and the Gaussian broadening of the incoming light (0.14 eV in our experimental conditions). In the case of RIXS the broadening, taken as Gaussian, depends merely on the overall instrumental resolution determined by the beam line and the spectrometer as no core hole is present in the final state (see section 2 for values).

4. Results and discussion

XAS spectra were recorded recorded at two different geometries (normal and 20° grazing incident) and with both linear horizontal and linear vertical polarizations. Measurements with incident photons at low grazing incident angle are expected to deliver more surface sensitive information. In the present case the a similar shape were obtained in both geometries confirming negligible contamination of the sample surface due to oxidation. Moreover no evident polarization dependence was observed compared to previously reported measurements on orthorhombic single crystal $DyMnO_3$, as in reference [26].

Figure 1 also illustrates the experimental RIXS spectra of Mn $L_{3,2}$ edge of $DyMnO_3$ at room temperature and at 25 K using LH polarization. The *d*–*d* excitations are observed on an energy loss scale ($h\nu_{\mathrm{in}} - h\nu_{\mathrm{out}}$) at 1.45 eV, 2.4 eV, 2.8 eV and 3.4 eV. Above $\approx$ 4 eV, a broad structure which disperses on the energy loss sacle corresponds to charge transfer spectral weight. Small temperature dependent variations of the relative intensities for the *d*–*d* excitations can be observed. The peak at 1.45 eV appears to be shifted at higher energy loss when the RIXS spectra are taken with incoming photon energies situated at the maximum of the white line (e) or higher energies. This observation suggests that the corresponding feature is composed by a manifold of *d*–*d* excited states which have different resonant responses.

Crystal field multiplet simulations performed for $DyMnO_3$ are shown in figure 2 along with results obtained for $TbMnO_3$. The complete set of experimental and computational results for $TbMnO_3$ will be presented elsewhere. The XAS measurements are shown after subtraction of the background. The values for the Coulomb and exchange interactions used in the calculations are gievn in table 1. The D_{4h} vrystal field acting on the Mn^{3+} ions can be described by three parameters: $10Dq$, Dt and Ds [19, 23]. $10Dq$ represents the splitting of the five-fold degenerated atomic 3*d* into a t_{2g} triplet and e_g doublet by an octahedral field, while Dt and Ds quantify the further

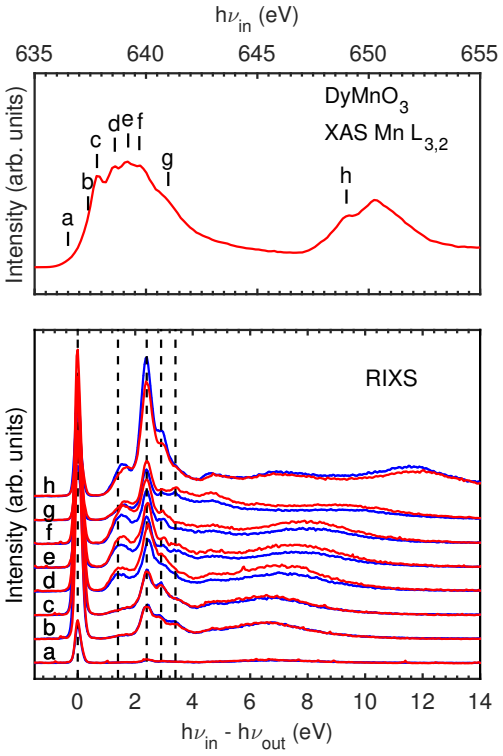

Figure 1. $DyMnO_3$: experimental Mn $L_{3,2}$ XAS spectrum (top panel), recorded at room temperature, and the Mn $L_{3,2}$RIXS measurements (bottom panel) made at room temperature (red line) and 25 K (blue line). The letters indicate the incident energies $h\nu_{\rm in}$ used for the RIXS measurements.

degeneracy lift by the tetragonal symmetry D_{4h}. The crystal field parameters employed in the calculations of the $DyMnO_3$ are: $10Dq = 1.6$ eV, $Dt = 0.06$ eV and $Ds = 0.36$ eV. These values represent the best combination of parameters found when fitting both the RIXS and the XAS data sets. The best set of crystal field parameters obtained for $TbMnO_3$ is almost the same, except for Ds which was found to be 0.31 eV.

According to the present crystal field parametrization, the tetragonal distortion is slightly larger for $DyMnO_3$ when compared to the isostructural $TbMnO_3$. More precisely, the splitting of the t_{2g} branch due to the tetragonal distortion will be $\Delta_{t_{2g}} = 3Ds - 5Dt = 0.78$ eV for $DyMnO_3$ and $\Delta_{t_{2g}} = 0.63$ eV for $DyMnO_3$. Considering the e_g branch, the tetragonal splitting obtained for for $DyMnO_3$ is $\Delta_{e_g} = 4Ds + 5Dt = 1.74$ eV while for $TbMnO_3$ we obtain $\Delta_{e_g} = 1.54$ eV.

Further insight into the effects of the crystal field can be obtained by measurements at the O K resonance (figure 3). The spectra were taken in the same geometries as the Mn $L_{3,2}$ measurements. The $1s \rightarrow 2p$ transitions map the unoccupied O $2p$ partial density of sattes (DOS) in the XAS spectrum while the occupied DOS is detailed in the fluorescence-like contribution to the RIXS data. Previous measurements on various Mn compounds [27–30] indicate that the first two peak structure of the XAS spectrum can be attributed to O $2p$ states hybridized with empty Mn states from the e_g branch: $(3z^2 - r^2)$

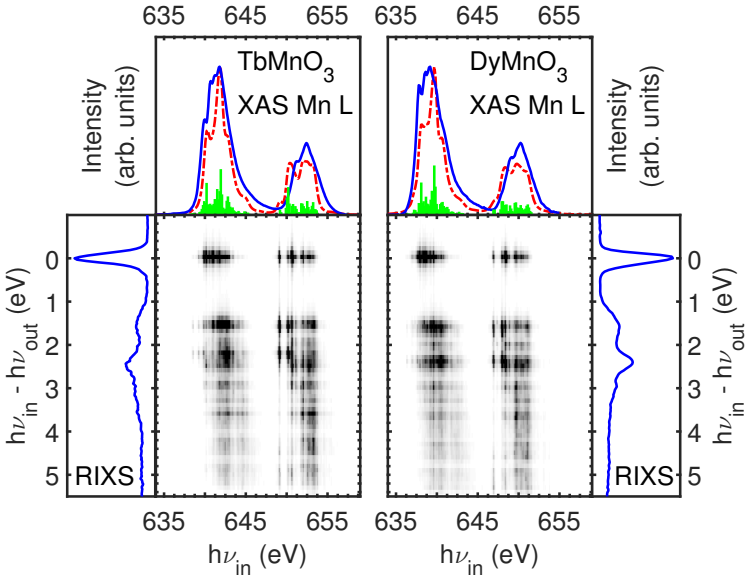

Figure 2. Experimental (blue line) and simulated (red dashed line) XAS data at Mn $L_{3,2}$ edge of $TbMnO_3$ (upper left panel) and $DyMnO_3$ (upper right panel). The green bars indicate the discrete intensities from the ground state to the core-hole final states of the absorption. 2D maps in the central lower panels display the intensities of the calculated RIXS spectra as a function of incident energy, $h\nu_{\rm in}$, and energy loss, $(h\nu_{\rm in} - h\nu_{\rm out})$. Side panels show the RIXS spectra measured at with incoming photons tuned at the maximum of the absorption white line.

Table 1. Parameters used for a consistent simulation of the Mn $L_{2,3}$ XAS and RIXS spectra of $DyMnO_3$ spectra (see figure 2). The values of the Coulomb and exchange integrals in the initial ($|i\rangle$), intermediate ($|n\rangle$) and final ($|f\rangle$) states, as well as the spin-orbit coupling ζ_{3d} of the $3d$ electrons. All energies are in eV.

Parameter	$\|i\rangle$ and $\|f\rangle$	$\|n\rangle$
F^2_{dd}	11.4151	12.2101
F^4_{dd}	7.1481	7.6491
G^2_{pd}	0.0	6.8452
ζ_{3d}	0.0462	0.0592

and $(x^2 - y^2)$ states. The second peak is also expected to contain spectral weight from the lowest spin-down t_{2g} empty states. When RIXS experiments are performed at these resonances, the O K RIXS spectra display Raman-like peaks situated at ≈ 1.5 eV and 2.4 eV which correlate well with the lowest d–d excitations observed in the Mn L_3 spectrum. The possibility to map orbital excitations on the metal site when exciting at the oxygen (ligand) site was previously reported for several oxides [31–34]. The Raman-like contribution in the O K spectra displays a strong resonant behavior. When $h\nu_{\rm in}$ is set at the lowest e_g peak (energy A) the intensity of the 2.4 eV is substantial. Increasing $h\nu_{\rm in}$ to the second XAS peak (energy B) leads to a strong reduction of the intensity in the Raman channel. In the case of $TbMnO_3$ the orbital excitation measured at resonance

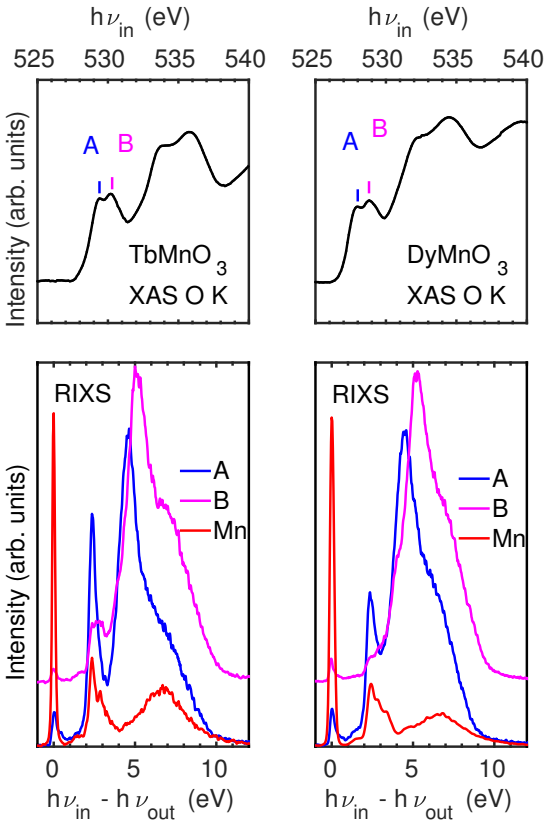

Figure 3. Experimental XAS spectra at O K edge of $TbMnO_3$ and $DyMnO_3$, where vertical lines indicate the incident energies used to measure the RIXS spectra presented in the lower panels. The RIXS spectra are compared with the Mn $L_{3,2}$ RIXS spectrum obtained at the maximum of the white line.

A is significantly sharper. The latter observation hints at a stronger localization of the $3d$ electrons in $TbMnO_3$ when compared to $DyMnO_3$.

5. Conclusions

We have probed experimentally the neutral electronic excitations in $DyMnO_3$ at the Mn $L_{3,2}$ and O K edges using XAS and RIXS. Considering Mn^{3+} ions in a D_{4h} symmetry, the local crystal field can be parametrized and the parameters obtained in a reliable way from the confrontation of experiments with theory. Our results indicate that the tetragonal distortion in $DyMnO_3$ is larger than in $TbMnO_3$, at variance with the variation of the ionic radii of the rare earth ions [35]. The present data are expected to stimulate further efforts for the elucidation of multiferroicity in $DyMnO_3$ especially with respect to quantification of the atomic displacement energies.

References

[1] Coey J M D, Viret M and von Molnár S 2009 *Adv. Phys.* **58** 571

[2] Alonso J A, Martinez-Lope M J, Casais M T and Fernández-Diaz M T 2000 *Inorg. Chem.* **39** 917
[3] Khomskii D I 2014 *Transition Metal Compounds* (Cambridge: Cambridge University Press)
[4] Kimura T, Ishihara S, Shintani H, Arima T, Takahashi K, Ishizaka K and Tokura Y 2003 *Phys. Rev. B* **68** 060403
[5] Goto T, Kimura T, Lawes G, Ramirez A and Tokura Y 2004 *Phys. Rev. Lett.* **92** 257201
[6] Zhou J S and Goodenough J B 2006 *Phys. Rev. Lett.* **96** 247202
[7] Kimura T, Goto T, Shintani H, Ishizaka K, Arima T and Tokura Y 2003 *Nature* **426** 55
[8] Kimura T, Lawes G, Goto T, Tokura Y and Ramirez A 2005 *Phys. Rev. B* **71** 224425
[9] Tokura Y, Seki S and Nagaosa N 2014 *Rep. Prog. Phys.* **77** 076501
[10] Dong S, Liu J M, Cheong S W and Ren Z 2015 *Adv. Phys.* **64** 519
[11] Fiebig M, Lottermoser T, Meier D and Trassin M 2016 *Nat. Rev. Mater.* **1** 16046
[12] Sergienko I A, Şen C and Dagotto E 2006 *Phys. Rev. Lett.* **97** 227204
[13] Walker H C, Fabrizi F, Paolasini L, de Bergevin F, Herrero-Martin J, Boothroyd A T, Prabhakaran D and McMorrow D F 2011 *Science* **333** 1273
[14] Walker H C, Fabrizi F, Paolasini L, de Bergevin F, Prabhakaran D, Boothroyd A T and McMorrow D F 2013 *Phys. Rev. B* **88** 214415
[15] Katsura H, Nagaosa N and Balatsky A V 2005 *Phys. Rev. Lett.* **95** 057205
[16] Zou T, Dun Z, Cao H, Zhu M, Coulter D, Zhou H and Ke X 2014 *Appl. Phys. Lett.* **105** 052906
[17] Sacchi M, Jaouen N, Popescu H, Gaudemer R, Tonnerre J M, Chiuzbăian S G, Hague C F, Delmotte A, Dubuisson J M, Cauchon G, Lagarde B and Polack F 2013 *J. Phys.: Conf. Ser.* **425** 072018
[18] Chiuzbăian S G, Hague C F, Avila A, Delaunay R, Jaouen N, Sacchi M, Polack F, Thomasset M, Lagarde B, Nicolaou A, Brignolo S, Baumier C, Lüning J and Mariot J M 2014 *Rev. Sci. Instrum.* **85** 043108
[19] de Groot F and Kotani A 2008 *Core Level Spectroscopy of Solids* Advances in Condensed Matter Science (Boca Raton, FL: CRC Press)
[20] Cowan R D 1981 *The Theory of Atomic Spectra and Structure* (*Los Alamos Series in Basic and Applied Sciences* vol 3) (Berkeley: University of California Press)
[21] Thole B T, van der Laan G and Butler P H 1988 *Chem. Phys. Lett.* **149** 295
[22] Ikeno H, de Groot F M F, Stavitski E and Tanaka I 2009 *J. Phys.: Condens. Matter* **21** 104208
[23] Figgis B N and Hitchman M A 2000 *Ligand Field Theory and its Applications* Special Topics in Inorganic Chemistry (New York: Wiley-VCH)
[24] Castleton C W M and Altarelli M 2000 *Phys. Rev. B* **62** 1033
[25] Fuggle J C and Inglesfield J E (eds) 1992 *Unoccupied Electronic States* (*Topics in Applied Physics* vol 69) (Berlin, Heidelberg, New York: Springer Verlag) chap "Core-hole lifetime broadenings" (Appendix B), p 347
[26] Chen J M, Hu Z, Jeng H T, Chin Y Y, Lee J M, Huang S W, Lu K T, Chen C K, Haw S C, Chou T L, Lin H J, Shen C C, Liu R S, Tanaka A, Tjeng L H and Chen C T 2010 *Phys. Rev. B* **81** 201102
[27] Park J H, Kimura T and Tokura Y 1998 *Phys. Rev. B* **58** R13330
[28] Merz M, Reutler P, Büchner B, Arena D, Dvorak J, Idzerda Y U, Tokumitsu S and Schuppler S 2006 *Eur. Phys. J. B* **51** 315
[29] Capogrosso V, Malvestuto M, Handayani I P, van Loosdrecht P H M, Nugroho A A, Magnano E and Parmigiani F 2013 *Phys. Rev. B* **87**(15) 155118
[30] Chandrasena R U, Yang W, Lei Q, Delgado-Jaime M U, Wijesekara K D, Golalikhani M, Davidson B A, Arenholz E, Kobayashi K, Kobata M, de Groot F M F, Aschauer U, Spaldin N A, Xi X and Gray A X 2017 *Nano Lett.* **17** 794
[31] Duda L C, Downes J, McGuinness C, Schmitt T, Augustsson A, Smith K E, Dhalenne G and Revcolevschi A 2000 *Phys. Rev. B* **61**(6) 4186
[32] Duda L C, Schmitt T, Magnuson M, Forsberg J, Olsson A, Nordgren J, Okada K and Kotani A 2006 *Phys. Rev. Lett.* **96**(6) 067402

[33] Okada K and Kotani A 2003 *J. Phys. Soc. Jpn.* **72** 797
[34] Bisogni V, Simonelli L, Ament L J P, Forte F, Moretti Sala M, Minola M, Huotari S, van den Brink J, Ghiringhelli G, Brookes N B and Braicovich L 2012 *Phys. Rev. B* **85**(21) 214527
[35] Jia Y 1991 *J. Solid State Chem.* **95** 184